Femtosecond Spectroscopic and Molecular Dynamics Simulation Studies of Chemical Reaction Dynamics in Condensed Phases

by

Weining Wang
B.S., Beijing University, 1984
M.S., Beijing Normal University, 1987

Submitted to the Department of Chemistry
in partial fulfillment of the requirements for the degree of

Doctor of Philosophy

at the

Massachusetts Institute of Technology
February, 1995

Signature of Author____
Department of Chemistry
December 23, 1994

Certified by____
Keith A. Nelson
Professor of Chemistry
Thesis Supervisor

Accepted by____
Dietmar Seyferth
Chairman, Departmental Committee on Graduate Students

This doctoral thesis has been examined by a committee of the Department of Chemistry as follows:

Professor Robert W. Field____
Chairman

Professor Keith A. Nelson____
Thesis Supervisor

Professor Moungi G. Bawendi____

Femtosecond Spectroscopic and Molecular Dynamics Simulation Studies of Chemical Reaction Dynamics in Condensed Phases

by
Weining Wang

Submitted to the Department of Chemistry on December 23, 1994
in partial fulfillment of the requirements for the degree of Doctor of Philosophy in
Chemistry

Abstract

Single-shot femtosecond spectroscopic methods have been developed to study the dynamics of solids or other nonflowable condensed phase samples where the accumulation of reaction products prevents the use of conventional femtosecond spectroscopic methods. The first method (the multiple-probe beam method) involves dividing the probe beam into 16 equal intensity pulses with known and controllable delays among them. Sixteen points along the time axis can be sampled at once. In the second method (the spatial encoding method), the cylindrically focused pump and probe beams cross with each other in a sample at a substantial angle. Different parts of the probe beam interrogate the sample at different delay times. The time-dependent sample response is therefore contained in the probe beam spatial profile and can be recovered by resolving the intensity of this probe spatial profile.

The spatial encoding single-shot method has been applied to study the reaction dynamics of 2,5-distyrylpyrazine (DSP) in its crystal phase. This is the first attempt to study the reaction dynamics of a solid state chemical reaction with femtosecond spectroscopy. It has been known that the crystalline environment enhances the rate of this reaction significantly. However, our preliminary results showed a short time signal similar to that in liquid solutions. This may suggest that the photoexcitation prepares the DSP molecule at a location on its reactive excited state potential energy surface below the transition state energy barrier. Further experiments are necessary to fully understand the roles the crystal lattice and other electronic states play in this reaction.

Molecular dynamics simulations have been performed to study the solvent cage effect on photodissociation in liquid and solid solutions. The purpose of this study is to assess the possibility of observing coherent oscillatory motions of photodissociated fragments on an intramolecular repulsive potential energy surface due to the confining forces of solvent cages. The results demonstrate that under realistically achievable conditions this type of oscillation can be observed in both amorphous solid solutions and liquid solutions. An instantaneous normal mode analysis has also been performed to gain more detailed information about the nature of these oscillations.

Thesis Supervisor: Keith A. Nelson
Title: Professor of Chemistry

ACKNOWLEDGMENTS

I would like to thank my advisor, Professor Keith Nelson, for his help and encouragement over these years. He has always been one of the best sources of ideas. I am especially indebted to him for the more pragmatic view on the objectives of scientific activities, i.e., something not just beautiful but also useful. I would also like to thank him for his patience and tolerance.

I would like to thank Professors Bob Field and Moungi Bawendi for being on my thesis committee and for their help and advice on various occasions. I would also like to thank Professor David Coker of Boston University for collaborations on the MD simulations. His generosity in providing computer resources and many delightful discussions are greatly appreciated. Thanks also to Professors Tom Keyes and John Straub of Boston University for useful discussions and advice.

I have been benefited a lot from working with the Nelson research group. I would like to thank all members of the Nelson group, past and present: Matt Banet, Kerry Brennan, Bernt Burferndt, Dutch Chung, Andy Cook, Lisa Dhar, Tom Dougherty, Anil Duggal, Jim Falters, John Fourkas, Ion Halalai, Alan Joly, Bern Kohler, Hitoshi Kawashima, Chris Mindas, Laura Muller, Dora Paolucci, John Rogers, Scott Silence, Marc Wefers, Gary Wiederrecht, Donghong Wu, and Yongwu Yang.

I wish to thank my parents, Zixiu and Fangding, for providing me with an excellent environment for intellectual and moral development. I thank my grandmother Runzhu for being around and making our lives happier. I also thank my sister Xuening for being my best friend since childhood (Now that friendship has been joined by Changchun and little Taotao). Thanks also to my uncle Yurong for being my "colleague" on science and philosophy during my high school years and, especially, for being a skeptic.

Finally, I would like to thank Li for her continuous support and understanding. Our common interests in scientific and social issues including our recent collaboration on the MD simulations have added enjoyable ingredients to our lives.

If this work has a value it consists in two things. First that in it thoughts are expressed, ... And ... the value of this work secondly consists in the fact that it shows how little has been done when these problems have been solved.

Ludwig Wittgenstein, *TRACTATUS LOGICO-PHILOSOPHICUS*

CONTENTS

1. INTRODUCTION

Since the advent of femtosecond lasers, elementary molecular processes such as coherent vibrational and rotational motions of molecules as well as those involved in chemical reactions such as bond breaking or bond forming can be induced and studied in real time [1.1, 1.2]. On an isolated molecule such studies have provided new information about its intrinsic dynamics. From this information molecular parameters such as potential energy surfaces could be extracted [1.1]. In condensed phases time-resolved spectroscopic methods have been used to study both the dynamics of neat liquids or solids and the influence of the environment on molecular and reaction dynamics [1.2]. With the pulse duration well into the sub-10-femtosecond regime new processes and phenomena can be studied.

The major technological advance in the recent few years is the discovery and development of femtosecond Ti:Sapphire lasers and amplifiers. Now pulses as short as 10 femtoseconds can be routinely generated. Amplification of 20 femtosecond Ti:Sapphire pulses to hundreds of mJ energy has also been demonstrated. These achievements have not only made possible observation of new physical and chemical phenomena that were not possible before but also allowed these to be accomplished in greater efficiency. In Section 2, we will discuss our efforts in the design and construction of a Ti:Sapphire amplifier system. This amplifier system will be used in the study of chemical reaction dynamics in solid phases.

Despite its tremendous success in the study of a variety of systems with chemical and physical importance, femtoseocond spectroscopic study of the dynamics of irreversible processes in solids or other nonflowable samples has not been undertaken. This is because most currently available femtosecond spectroscopic methods are performed in a repetitive manner. Many pairs of excitation and probing pulses are required to characterize a time-dependent signal. In the gas or solution phase, flowing of the sample to remove any products generated by each pair of excitation and probe pulses is necessary to guarantee each pair of pulses interacting with fresh sample. In solid phase samples, however, flowing of the sample is not possible. Reaction products will accumulate in the illuminated volume, preventing reliable experimental results. Without fast electronics to resolve femtosecond time scale signals, we have initiated the development of single shot optical methods. We will report in Section 3 our efforts in developing the single-shot femtosecond spectroscopic methods. First we will describe the multiple beam method and present experimental results. Then we will describe the spatial encoding method. The advantages and limitations of both methods will be discussed.

In Section 4, we will apply the single-shot method (spatial encoding method) to the study of chemical reaction dynamics in solid phase. Solid state reactions are of both scientific and practical importance. A solid state environment provides many unique and interesting features that are not available in other phases. One of them is that the crystal lattice can exert strong control over the course and the products of a chemical reaction by fixing the reactant molecules in a special geometrical arrangement. The collectiveness of the ordered molecular arrangement may also have great influence on reactions. For example the propagation of excitations may be facilitated. Energy may be deposited into a reaction coordinate in a mode specific manner due to phonons. Solid state samples also allow controlled modification of molecular parameters such as the distance and orientation between a pair of reactants by varying the temperature and/or pressure of the sample. Finally, solid state reactions may offer us opportunities of observing bond formation without the complication of diffusion. As the first solid state reaction to be studied by femtosecond spectroscopy, we have chosen the oligomerization reaction of 2,5-distyrylpyrazine in its crystal phase. In this reaction chemical bonds form between two molecules in a crystal upon photoexcitation. This is one of the prototype solid state reactions because it demonstrated many of the unique features of a solid state reaction.

In Section 5, we will change to a different topic, that is the solvent cage effect on photodissociations. We have performed molecular dynamics simulations to investigate the possibility of observing coherent oscillatory motion between a pair of photodissociated fragments on their intramolecular repulsive potential energy surface. It has long been known that in condensed phases molecules (or atoms) are surrounded by other molecules, although their motions are usually diffusive on a long time scale, on a very short time scale, the molecules may execute oscillation-like motions ("rattling") rather than diffusion [1.3, 1.4]. This type of behavior has first been observed experimentally with rotational motion of some linear molecules such as CS_2 where CS_2 molecule may execute librational motion against its liquid surrounding [1.5, 1.6]. The translational analogue of this phenomenon has not been observed because there is not a straightforward way to create and observe coherent translational motion through optical excitation. Photodissociation offers a chance to observe this. However, due to reasons we will discuss later, such behavior has not been observed. In order to have a more accurate evaluation of the possibility of observing this behavior in the real world, we have applied molecular dynamics simulations to the problem. We hope that the simulations will offer us better understanding of the problem and hence assist us in our future experimental explorations. These explorations in turn will add to our understanding of the influence of condensed media on chemical reactions.

Most of the work presented here is part of the continuing effort to reach a better and deeper understanding of condensed phase chemical reaction dynamics. Some of the work is actually just a start of an entirely new area. Whenever possible we will point out any future development directions from our current point of view.

2. LASERS

2.1 FEMTOSECOND TI:SAPPHIRE LASER

The discovery and development of femtosecond Ti:Sapphire lasers have revolutionized the ultrafast laser technology. It is not only technically superior than any femtosecond dye lasers in many respects including higher energy, shorter pulse duration, wider tunability, but also much easier to operate.

Ti:Sapphire as a tunable laser material was first demonstrated and characterized less than a decade ago [2.1]. Ti:Sapphire laser can lase from 660 nm to over 1000 nm. It was soon discovered that due to self-focusing in the Ti:Sapphire crystal, self-modelocking can be achieved to generate short pulses [2.2, 2.3]. Since Ti:Sapphire has a gain bandwidth to support a pulse duration of a few femtoseconds, a lot of efforts have been devoted to compensate the group velocity dispersion inside the cavity [2.4-2.6]. As a result, pulses as short as 11 femtoseconds have been generated.

In our experiment we will use a commercially available Ti:Sapphire laser from Coherent (Mira 900). The laser produces pulses of 50 femtoseconds at 76 MHz. The single pulse energy is on the nanojoule level. In order to achieve higher single pulse energy amplification of the oscillator output is necessary.

2.2 THE TI:SAPPHIRE AMPLIFIER

Ti:Sapphire is also a very good material for laser amplification. In addition to its large gain bandwidth, Ti:Sapphire has very good energy storage capability and high thermal conductivity. However, in order to extract the energy stored in the gain medium efficiently, a high fluence is needed. For short pulses in the sub-100 femtosecond duration regime, it is often impossible to maintain a high enough fluence because a high fluence means high peak power. Nonlinear effects will distort the temporal and spatial profiles of the pulses and even cause damage to the laser crystal. In order to solve this problem, a scheme called chirped pulse amplification (CPA) has been developed [2.7]. In this scheme, the short pulse is stretched to much longer duration before being amplified. After the pulse energy has reached maximum, it is recompressed to its original duration. The amplification is often achieved with a regenerative amplifier because of the smaller cross section of titanium atoms and hence the smaller single pass gain as compared to dye molecules.

We have constructed a Ti:Sapphire amplifier using this chirped pulse amplification scheme based on the design of Mourou and co-workers[2.8, 2.9]. A schematic of our amplifier system is shown in Fig. 2.1. The symbols of the optical elements and their specifications are listed in Table 2.1.

About 10% of the Mira output is sent across the table to seed the amplifier. Since the beam from the Mira is diverging, a telescope (L_1 and L_2) is used to collimate the beam. The polarization of the seed pulses is horizontal. The seed pulses pass through a cube-polarizer (Q_1) and a half-wave plate (HP) which is oriented to give a 45° rotation of the polarization of the seed pulses. The seed pulses then pass through a Faraday rotator (FR) adjusted to rotate the polarization of the seed pulses for 45° in the other direction and emerge polarized horizontally again. Then the seed pulses pass through cube-polarizer Q_2

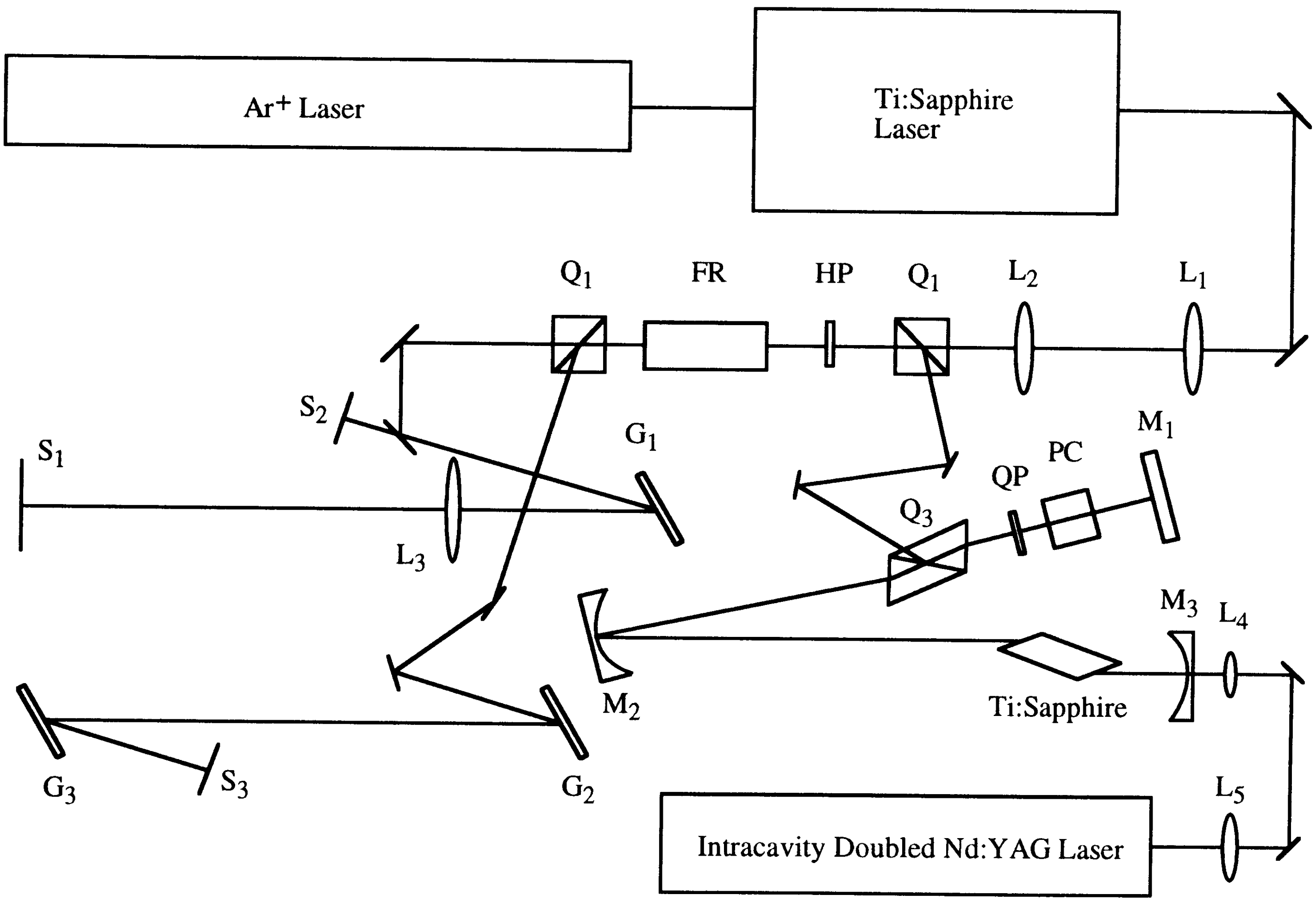

Figure 2.1 Layout of the Ti:Sapphire amplifier system.

Table 2.1 Specifications of the optical elements in the Ti:Sapphire amplifier.

	Symbol and Specification
Collimating Telescope	L_1: 40 cm focal length
	L_2: 25 cm focal length
Faraday Rotator Assembly	Q_1: Cube polarizer (Special Optics)
	Q_2: Cube polarizer (Special Optics)
	HP: Half waveplate (Special Optics)
	FR: Faraday Rotator (ConOptics)
Stretcher/Compressor	G_1, G_3: 11 x 4 cm 1800 l/mm gold coated holographic replica grating (Milton Roy)
	G_2: 4 x 4 cm 1800 l/mm gold coated holographic replica grating (Milton Roy)
	L_3: 4" diameter, 50.0 cm focal length biconvex singlet lens (OFR)
	S_1, S_2, and S_3: 3" diameter ER.2 mirror (Newport)
Regen Amplifier	M_1: Plano HR @ 730-810nm (CVI)
	M_2: Concave 100 cm ROC HR @ 730-810nm (CVI)
	M_3: Concave 50 cm ROC HR @ 730-810nm, AR coating @ 532nm on back surface (CVI)
	PC: Pockel's cell (Medox)
	QP: Quarter waveplate (Special Optics)
	Q_3: Cube polarizer (Karl Lambrecht)
	Ti:Sapphire: Brewster cut, 2.0 cm long, 6mm ϕ, $\alpha = 1.15$ @ 523nm (Crystal Systems)
	L_4: 15 cm focal length lens (CVI)

and are sent into the stretcher.

Fig. 2.2 a) shows a more detailed schematic of the stretcher we use. The upper panel shows the top view and the lower panel shows the side view. This is a folded variation of the standard stretcher [2.10, 2.11] (or it could be called a grating compressor with positive group velocity dispersion) using only a single grating and a single lens. The input beam is dispersed by grating G_1. The diffracted beam passes through lens L_3 at the center horizontally while below center vertically so that it returns to grating G_1 higher than the input beam after being reflected back by mirror S_1. This beam passes just over the mirror which sends in the input beam, and is reflected back by mirror S_2 traveling exactly the same path in the opposite direction back into and then out of the stretcher. The distance from lens L_3 to mirror S_1 equals the focal length f of L_3 (50 cm in our case). The distance d from grating G_1 to lens L_3 is adjustable but shorter than f. This distance is decided by the desired stretching factor. (The effective length of the stretcher is $2f - 2d$.) We used a distance of about 18 cm. The pulses coming out of the stretcher temporally dispersed travel exactly the same path back with the polarization unchanged until after polarizer Q_2. The Faraday rotator rotates the returning pulses 45° in the opposite direction to that from the first pass. After the returning pulses pass through HP again, they polarize vertically instead of horizontally and are reflected by cube-polarizer Q_1, therefore separated from the incoming beam. They are then sent into the regenerative amplifier cavity.

Fig. 2.3 shows a more detailed schematic of the regenerative amplifier. The folded regenerative amplifier cavity consists of two curved end mirrors and one flat end mirror. The 532 nm pump light is sent through mirror M_3 and focused with a 15 cm focal length lens onto the Ti:Sapphire crystal. The Ti:Sapphire crystal is mounted in a home-built cooling block and put about 13 cm away from mirror M_3. The other cavity mirror M_2 is about 43 cm away from the Ti:Sapphire crystal. In the other arm of the cavity, there are a cube-polarizer (Q_3), a quarter-waveplate (QP), and the Medox pockels' cell (PC).

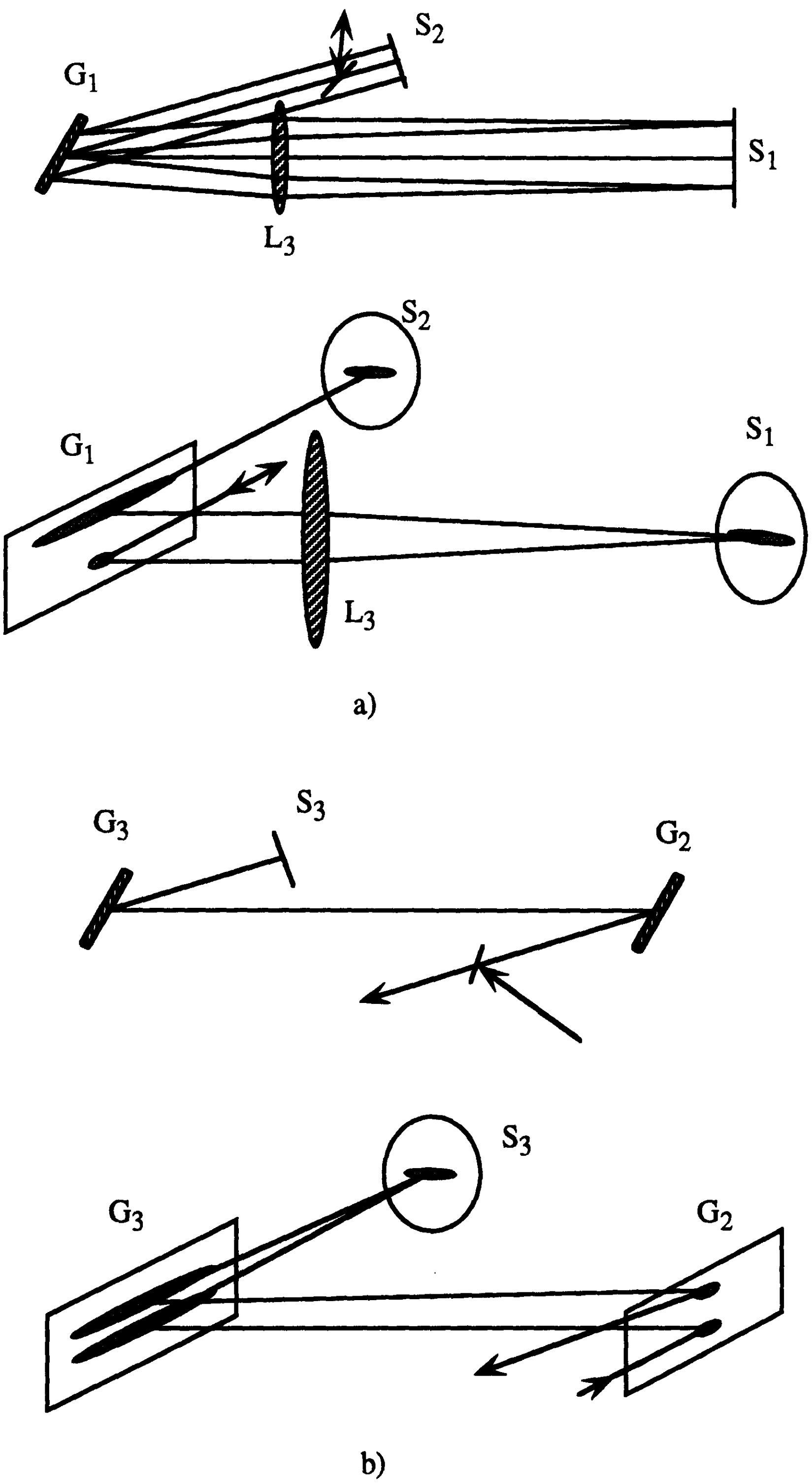

Figure 2.2 Top and side views of a) stretcher and b) compressor.

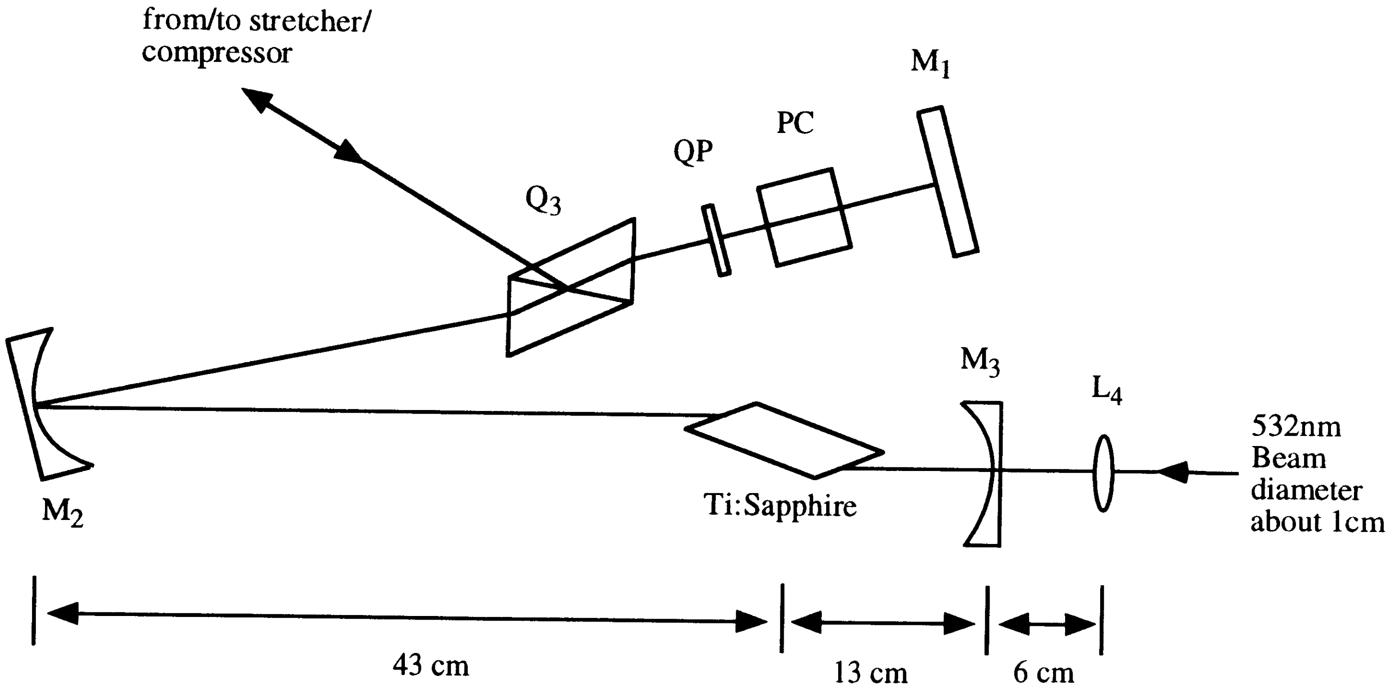

Figure 2.3 Schematic of the regenerative amplifier cavity.

Mirror M_1 is plano. The length of this arm is not as critical as the other arm of the regen. The angle between the two folded cavity arms is kept as small as possible. The stretched pulses are injected into the cavity through cube-polarizer Q_3. The incoming beam is vertically polarized and reflected into the cavity. Without any voltage across the Pockels' cell, the two polarization components have a total retardation of one half wave between them and pulses switch polarization each round trip so that no pulse energy buildup happens. It is also possible to achieve this quarter wave retardation by misaligned the Pockels' cell rather than using a quarter-waveplate. The injection is achieved by applying a quarter wave voltage to the Pockels' cell. The total retardation is one full wave so that only the one pulse already in the cavity is trapped and amplified while other seed pulses are rejected. After the amplified pulse has reached a maximal energy, another quarter wave voltage is applied to the Pockels' cell to switch the pulse out. The time window between the two voltage steps is decided by both the energy of the pump laser and the energy of the seed pulse (to a lesser extent). When pumping with about 6 mJ (about 4 mJ absorbed by the crystal) of green light, a time window of about 270 ns (21 units on the Medox driver dial) is needed and an output energy of about 700 μJ is achieved. The amplified pulse travels back along the same path as the incoming seed pulse until cube-polarizer Q_2 where it is reflected and sent into the compressor.

Fig. 2.2 b) shows a more detailed schematic of the compressor. The compressor is a standard parallel grating compressor which induces negative dispersion to the pulses and therefore reverses the positive chirp induced by the stretcher and in the regen cavity. Mirror S_3 was slightly tilted to allow the output beam being separated from the input beam. The grating separation should match the effective length of the stretcher. With an effective length of 64 cm of our stretcher, the compressor length should be around 64 cm, but due to the dispersion inside the regen, the actual length was longer. The compressor has an efficiency of about 35% which give a pulse energy after compression of about 250 μJ.

The alignment of the amplifier system is important for both shorter pulse duration and higher pulse energy. The following is a procedure that has been found to work. (It may not be the best one.)

1. Faraday rotator assembly. This is usually not routinely needed. After initial alignment, we set two apertures, one in front and one after the Faraday rotator assembly. It was often good enough even though the seed beam had moved. The initial alignment involved setting the beam path parallel to the table first and putting in each optics while keeping the beam path unchanged.

2. The stretcher. It may be more convenient to run the Mira in cw mode rather than in modelocked mode for the first 5 steps below, because it is easier to match two spots of light than one spot and one dispersed strip of light.

(1) Make sure that the grating is vertical by making the input beam, the reflected beam, and the diffracted beam the same height above the table.

(2) Find the Littrow angle by rotating the grating until the diffracted beam and the input beam overlap. Rotate the grating back to about 13° off Littrow angle. This was the smallest practical angle we could use. Finding the Littrow angle first is helpful when trying to match the compressor grating angle with the stretcher grating angle.

(3) Put in mirror S_1 at the desired distance and align it to make sure the beam coming back onto itself.

(4) Insert lens L_3 between G_1 and S_1 at a distance of 50 cm from S_1. Align it through the center first so that the beams stay in their original path. Then translate L_3 upward to allow backgoing beam path higher.

(5) Put in mirror S_2 and align it so that the output beam overlaps the input beam all the way until after the Faraday rotator assembly. The output should be reflected by cube-polarizer Q_1.

(6) Let the Mira run in modelocked mode. Adjust the distance of L_3 to S_1 so that the beam spatial profile is not distorted after leaving the stretcher.

(7) Make sure that no part of the spectrum is blocked before turning on the amplifier.

3. The regenerative amplifier.

(1) The initial alignment of the regen cavity is best done with a 20% output-coupler in the place of M_1. The output energy of this free running laser was typically 35% of the absorbed energy.

(2) Seed pulse is aligned with the regen running in Q-switching mode so that the output from the free running cavity can be used as a guide for the seed pulse.

(3) Once amplification is seen, adjust the timing (both the window location and the window width) to select a clean single pulse.

(4) Optimize the energy by fine tuning both the timing and the alignment of the Pockels' cell.

4. The compressor.

(1) Align the two gratings by making sure that both the reflection and diffraction are in the same plane parallel to the table.

(2) Set the angle of the first grating as close to the angle in the stretcher as possible. This can be done by finding the Littrow angle first and rotating the grating the same amount as in the stretcher.

(3) Set the angle of the second grating as close to the first grating as possible so that no spatial dispersion left after the pulses leave the compressor.

(4) Adjusting the distance between the gratings to minimize the pulse duration. Then iterate: first grating angle--->2nd grating angle--->mirror angle--->grating distance--->first grating angle.... until the minimal pulse width is achieved. With this procedure it was easy to achieve a pulse duration of 150 femtoseconds as compared to the shortest pulse on

this amplifier of about 110-120 femtoseconds which we could get occasionally. This is not a very efficient way of aligning the compressor. With so many degrees of freedom to be optimized, it is best to have more information about the pulses than just a autocorrelation trace. The recently developed frequency-resolved optical gating (FROG) method [2.12] suggested a good way to do this. This method utilizes the optical Kerr effect in a nonlinear optical sample with instantaneous response to obtain a 2D display of pulse intensity vs. frequency and delay time. Group velocity dispersion of the pulses is visually seen through the orientation of the 2D spectogram. Optimization of the alignment of the compressor (maybe the stretcher as well) according to this spectrogram improves the efficiency significantly. (It is to be noted that this is not the intended application of FROG which is more an algorithm to retrieve the phase of the pulses than a experimental technique.)

2.3 INTRACAVITY FREQUENCY DOUBLED Nd:YAG LASER

The pump laser for the Ti:Sapphire amplifier is a Q-switched intracavity doubled Nd:YAG laser with a Z-cavity based on a design by Yongqin Chen at Berkeley. This laser is a variation of the original Z-cavity laser developed by M. V. Oritz and co-workers [2.13] with the laser head being replaced by a Spectron head. Intracavity doubling has long been recognized as the best way of achieving high green power (532 nm) in cw or Q-switched solid state lasers, such as Nd:YAG laser, at a relatively high repetition rate (1 kHz and above) [2.14-2.16]. This is because the pulse duration for a Q-switched laser is on the nanosecond and above level, the efficiency for extracavity doubling is low. It is not easy to scale the power up because the high thermal load generated will degrade the laser performance. Only lasers with very low repetition rate (10 Hz, for example) have been used. In an intracavity doubled laser the output loss mechanism is the converting of the fundamental into its 2nd harmonic. In principle 100% efficiency could be achieved.

Fig. 2.4 shows a schematic of the laser cavity. In order to extract more 2nd harmonic, an intracavity doubled laser often uses a folded cavity to allow combining the 2nd harmonic generated in both of the two opposite passes through the doubling crystal. In our cavity M_4 is a high reflector for both the fundamental (1064 nm) and the 2nd harmonic (532 nm). A telescope (optical relay) formed by a pair of mirrors M_2 and M_3 is put between the laser rod and the KTP crystal. This is to overcome the prominent thermal lensing problem in the YAG rod by keeping the spot size in the KTP crystal relatively insensitive to the thermal focal length of the YAG rod which varies with the pumping power. The thermal focal length of the YAG rod is usually decreasing with increasing pump power. Without the optical relay this will decrease the spot size in the KTP crystal and may cause damage to the KTP crystal. The laser is running in unpolarized mode in order to use the type II doubling crystal without waveplate. This requires the Q-switch to be normally cut rather than Brewster cut. It also requires the Q-switch to be operated in the shear mode driven by 100W RF power. The Q-switch is synchronized to the regen and the Mira through the use of the Mira pulse train as the frequency source. Fig. 2.5 shows an electronic connection diagram. The Medox Pockels' cell driver was synchronized to the Mira. It divided the repetition rate by 1000 first. The final repetition rate was chosen by further division. We have chosen to use a repetition rate of 1 KHz. The 1 KHz trigger was sent to the pump laser's Q-switch driver through a digital delay box. TTL high was sent to jumper j3-2. The overheat sensor must be connected before turning on the RF power. We did not use a Q-switch's overheat sensor with other Q-switches in the past. Compare to the 5W of RF power we used with other Q-switches, 100W of RF power is more likely to cause damage to the Q-switch should inadequate cooling happen. The KTP crystal is oriented to allow vertical polarization of the green. The crystal is put in a CSK oven and heated to 70°C to avoid accumulated damages. The 532 nm output power as high as 8 W at a repetition rate of about 1 KHz has been generated. This translates into a pulse energy of 8

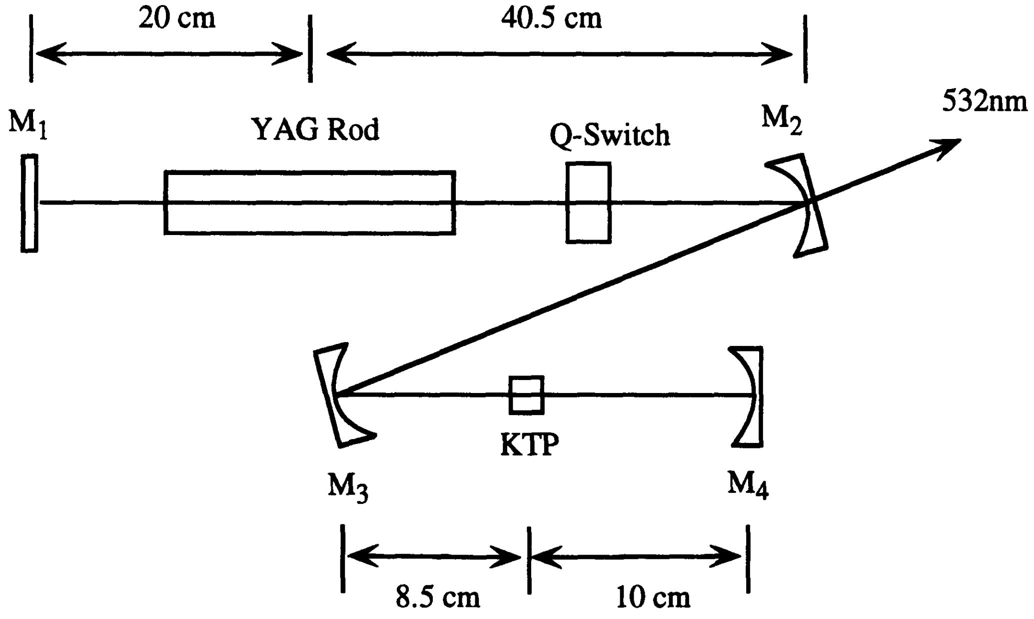

Figure 2.4 The cw-pumped, Q-Switched, and intracavity frequency doubled Nd:YAG laser.

M1: Plano HR @ 1064nm (Alpine Research Optics)
M2: Concave 50 cm ROC HR @1064nm and HT @532 (Alpine Research Optics)
M3: Concave 20 cm ROC HR @1064nm and 532nm (Alpine Research Optics)
M4: Concave 10 cm ROC HR @1064nm and 532nm (Alpine Research Optics)
Q-Switch: normally cut, 100W RF (Crystal Technology)
KTP: 3 x 3 x 5 mm double V coating @ 1064nm and 532nm (Airtron) heated to 70C in CSK oven
HR: high reflection; HT: high transmission; ROC: radius of curvature

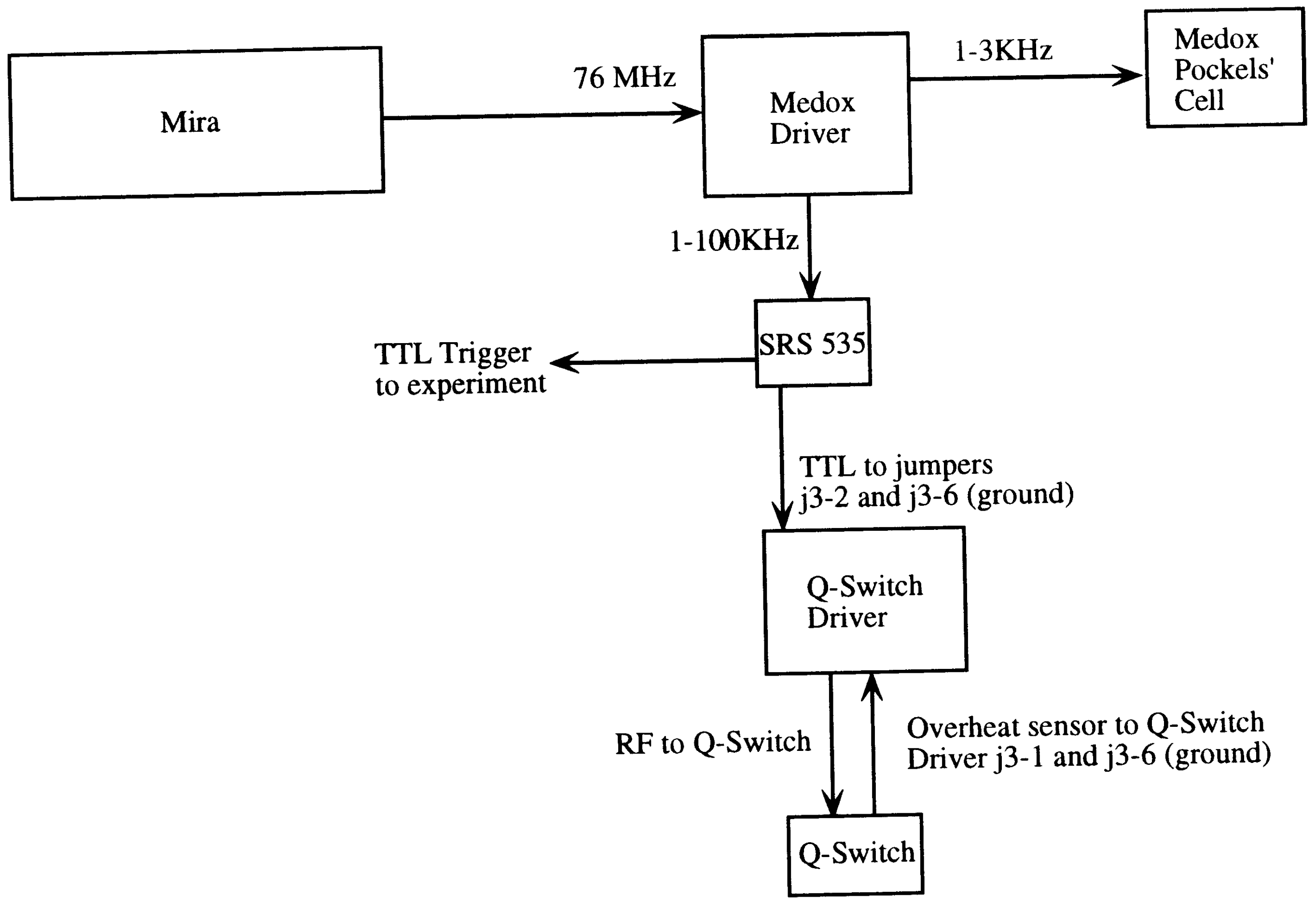

Figure 2.5 Electronic connections of the amplifier system.

mJ. The laser routinely runs at about 6 W without any tweaking. The energy fluctuation (peak to peak) is below 1%. The pulse duration is typically 120 ns indicating that the laser may be undercoupled, i.e., the output coupling through 2nd harmonic generation is below the optimum level.

To align the laser we first used a 10% output coupler in the place of M4. Without the Q-switch and the KTP crystal inside the cavity, we optimized the output power. We could achieve a cw power of about 30W. Then the Q-switch was inserted and aligned to have the best contrast. After that the KTP crystal was inserted and aligned with reduced lamp power and the Q-switch off. Then we turned the lamp to full power and turned on the Q-switch and fine tuned the phase-matching angle to optimize the pulsed green output.

2.4 FEMTOSECOND DYE LASER SYSTEMS

The laser system used to conduct the multiple probe beam single shot experiments was an antiresonant ring dye laser synchronously pumped by the frequency-doubled output of a cw modelocked Nd:YAG laser. The output, centered at 620 nm, is passed through a three-stage amplifier which is pumped by the frequency-doubled output of a Q-switched, modelocked, and cavity-dumped Nd:YLF laser [2.17]. The Nd:YAG and Nd:YLF pump lasers are synchronized through the use of a common RF source which drives both of their modelockers. The synchronously amplified output consists of 80-fs, 10-μJ, 620-nm pulses at a 500-Hz repetition rate.

2.5 FUTURE IMPROVEMENTS

Ti:Sapphire laser technology is evolving fast. Chirped multilayer coatings have been developed to be used in the Ti:Sapphire oscillator for dispersion control [2.18, 2.19].

This should be superior to the currently used prism pairs in that dispersions in all orders may be tailored to achieve the minimum pulse duration supported by the Ti:Sapphire bandwidth. Cavity-dumped Ti:Sapphire oscillators have also been demonstrated [2.20, 2.21]. This type of oscillator can produce 20 femtosecond pulses at the 100 nJ level with a repetition rate as high as 250 KHz. The energy per pulse is high enough to allow many condensed phase experiments while the high repetition rate allows phase sensitive methods to be used.

The amplification of the Ti:Sapphire laser has also seen significant development. The major problem in the amplification, i.e. the difficulty in recompressing the amplified pulses to their original duration, has been largely solved [2.22, 2.23]. The pulse durations for these amplifier systems were 20-30 femtoseconds with energies as high as 100 mJ. These and other amplification systems use reflective optics in their stretcher to avoid chromatic aberration and dispersion introduced by refractive optics. Low resolving power gratings are also advantageous in that alignment tolerances were improved [2.9]. Since a high energy system is needed for most of the single shot experiments due to the extensive spatial filtering and larger beam sizes, improvements in our amplifier system should be important.

In order to achieve higher energy amplified pulses, a higher energy pump laser is needed. The green pulse duration from our YAG laser indicates undercoupling. This means that we may be able to improve it by using a longer KTP crystal or using a telescope with a smaller demagnification ratio to increase the spot size in the KTP. It is also possible to use two laser heads inside the cavity instead of one to increase IR power and use a larger spot size in the KTP to increase the green output.

3. SINGLE SHOT FEMTOSECOND SPECTROSCOPIC METHODS

3.1 INTRODUCTION

The traditional time-resolved experiments are performed employing a repetitive scheme [3.1]. In this scheme (see Fig. 3.1), the delay between the probe pulse and the pump pulse is set to a specific value and a number of pairs of pump and probe pulses pass through the sample. The intensities of these probe pulses are collected and averaged to generate one point on the time-dependent signal curve. Then the delay between the pump and probe pulses is set to another value and the process is repeated. The time dependent signal curve is a result of many different delays each of which corresponds to many excitation and probing processes. This is a way to circumvent the problem that no fast enough photodetectors and electronic signal conditioning devices are available which can follow the signal change in real time on a femtosecond time scale. With most gas phase or liquid phase samples this scheme does not pose any problems, because these samples can be flowed through the illuminated volume so that products formed after one pair of pump and probe pulses can be removed before the next pair of pulses. For those solid state samples which can recover before the next pair of pump and probe pulses come, such as after ISRS excitation of phonons, this scheme also works well. On the other hand, with solid samples which undergo irreversible photochemical reaction as well as solid samples to which laser radiation causes permanent changes such as optical damages, the same scheme is no longer applicable. There will be products building up inside the sample. Each pair of pulses will see a different sample composition. The signal generated this way will be different from the signal that the true dynamics would generate. In the most severe case, the sample could change so much that the deteriorated optical quality may no longer permit any further experiment. The simplest way of dealing with solid samples of this kind may be to move the sample after each exposure. This would require large size, physically and chemically uniform samples which are often difficult to obtain. If the sample uniformity is not great, calibration from spot to spot is extremely difficult. This situation has motivated the development of single shot methods which should allow us to recover as much information after each excitation as possible.

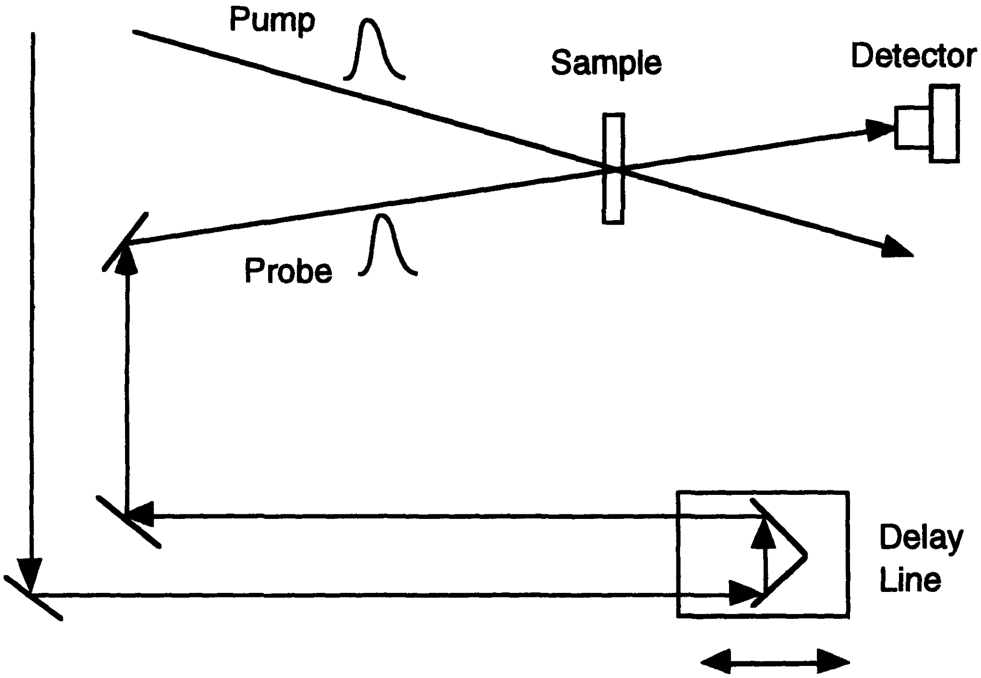

Figure 3.1. Conventional Pump Probe Experiment Setup

3.2 MULTIPLE PROBE METHOD

The first single shot method we have developed is the multiple probe beam method [3.2-3.4]. This is a brute force method which achieves its goal of single shot detection by dividing the probe beam into 16 equal intensity, spatially and temporally separated parts and monitoring the intensity of each of them after they pass through the sample following the pump pulse. Since the delays among them are variably controlled, we can sample 16 points on the time axis after a single excitation. The method also allows real time probing of the same sample volume. Although 16 points are often not enough to characterize a signal completely, the method provides internal calibration which would be important when combining with probing several sample spots. A schematic of the device is presented in Fig. 3.2. Fig. 3.3 shows the experimental setup. The 16 beam device was designed and built in a way that the two major requirements, compactness and robustness, were achieved. The whole device occupied a 3' by 3' breadboard (Newport Corp.) with the 16 arms grouped into 4 tiers and mounted on each side of two vertical breadboards. The retroreflector for each arm was mounted on a translation stage (Klinger) which provided a 2.5 cm travel. The relative timing among the 16 beams were set with the stages at the middle of their traveling range so that after aligning the timing of each beam could be varied without realigning. The single probe beam was sent into the device and passed through the series of beamsplitters and retroreflectors (see figure 3.2). After the device, it became 16 spatially separated and temporally delayed pulses. These 16 beams were arranged in a 4 by 4 grid of approximately 1.5" by 1.5". The beams were focused to the sample with a 3 inch diameter lens with a focal length of 10 cm. The sample was put at the focal point. Another lens with identical specifications was put after the sample to collimate the 16 spot grid back to its original size. A CCD detector (Princeton Instrument) was used to collect the

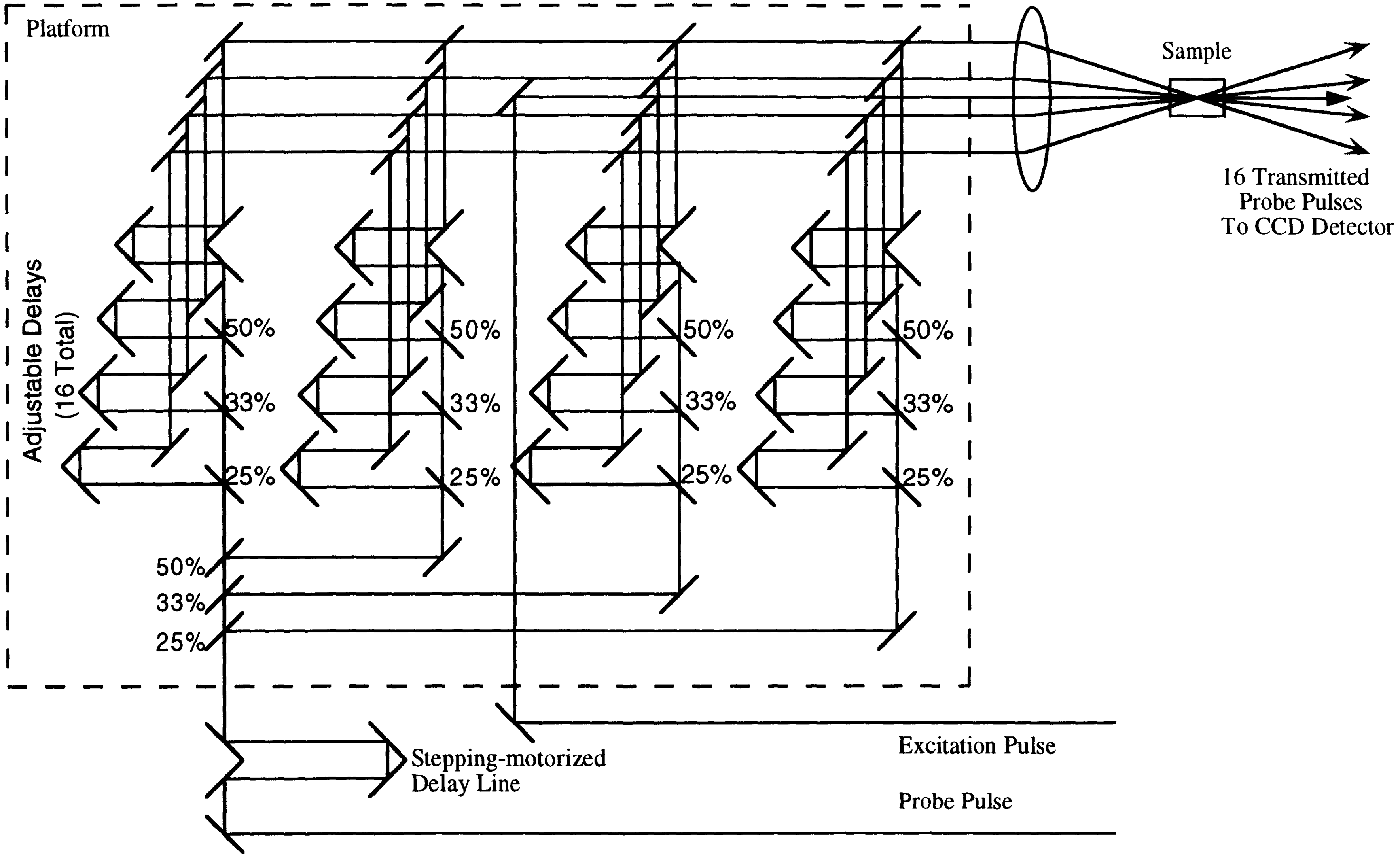

Figure 3.2. Schematic illustration of pump-probe experiment with 16 probe pulses.

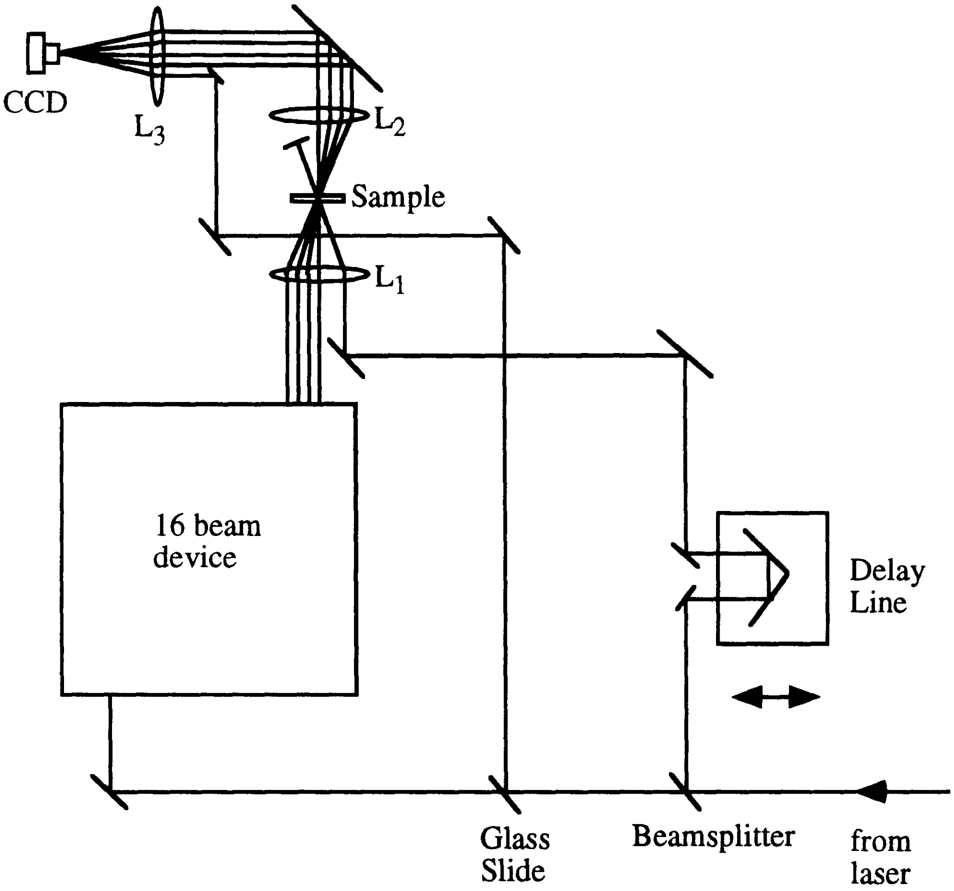

Figure 3.3 Experimental setup for the multiple probe pulse experiment. L_1, L_2, and L_3 are 3 inch diameter lenses with a focal length of 10cm.

intensities of all 16 probe pulses simultaneously. A seventeenth beam which was derived from the probe before it entered the device was sent to the CCD as a reference to normalize the shot-to-shot intensity fluctuation of the laser. Data recording was as follows. First the pump beam was blocked and an image of the 16 beam grid was taken by the CCD detector. This image was saved and used as the background. Then the pump beam was unblocked and signal images were recorded. The intensity of each probe pulse in each image was then calculated and divided by the intensity of the reference pulse. The signal curve consisting of 16 points was generated by subtracting the background and combining with a file which contained timing information of the 16 probe pulses. This timing file was manually edited from delay information determined independently in advance and saved in a sequence that matched the CCD readout sequence. Then the assignment of the delay time to each beam was automatically performed by specifying the name of the time file during data processing.

The time resolution of a femtosecond experiment depends on experimental geometry. In the collinear, copropagating pump-probe geometry the time resolution is pulse duration limited. In the 16 probe pulse experiment, since the 16 beams are spatially separated, they can not collinearly propagate with the pump. When the pump and probe beams are not collinear the resolution will degrade from pulse duration limited. It is important to know the time resolution of this setup. We have calculated the dependence of time resolution on crossing angle and beam sizes. Fig. 3.4 shows the geometry of a noncollinear pump-probe experiment.

Assume that $I_1(t)$ and $I_2(t)$ are the pump and probe pulse intensities and $\gamma(t)$ is the sample response function. The pump induced change in the sample is given by

$$\Delta\Gamma(t) = \int dxdydz \int_{-\infty}^{\infty} \gamma(t-t')I_1(t')dt' \qquad (3.1)$$

The change in probe intensity is thus given by

$$\Delta I_2(\Delta t) = \int dxdydz \int_{-\infty}^{\infty} \Delta\Gamma(t) \cdot I_2(t)dt \tag{3.2}$$

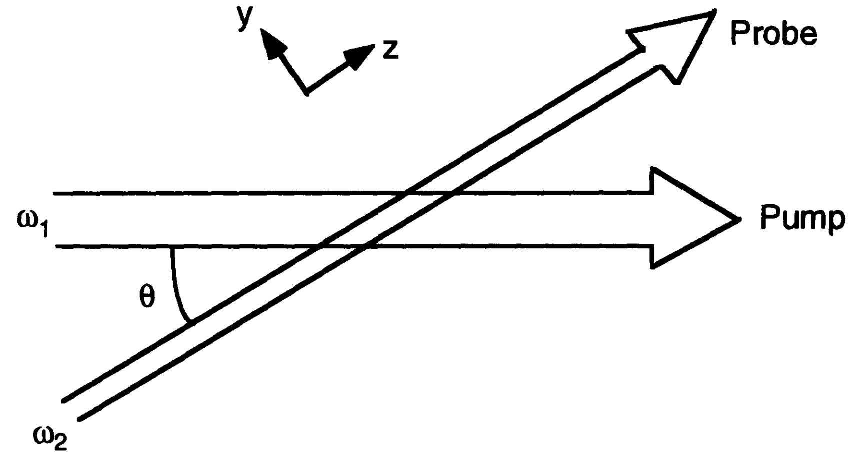

Figure 3.4 Schematic of noncollinear pump-probe experiment geometry

The signal for an instantaneous response $\gamma(t)=\delta(t)$ is then given by

$$S(\Delta t) \propto \int dxdydz \int_{-\infty}^{\infty} I_2(t+\Delta t) I_1(t)dt \tag{3.3}$$

The time resolution was defined as the full width at half maximum of $S(\Delta t)$ and calculated to be

$$\Delta = \left\{ -\frac{\left(1+\frac{1}{\omega_3^2}\frac{R}{Q}\right)^2}{H} + 1 - \frac{1}{\omega_3^2}\frac{1}{Q} \right\}^{-\frac{1}{2}} \frac{\tau}{\sqrt{2}} \tag{3.4}$$

where

$$R = -\frac{\gamma}{\alpha}\cos\theta\sin^2\theta - \cos\theta - 1$$

$$Q = -\frac{\gamma^2}{\alpha}\cos^2\theta\sin^2\theta + \frac{\sin^2\theta}{\omega_1^2} + \frac{\cos^2\theta}{\omega_3^2} + \frac{1}{\omega_3^2}$$

$$H = -\frac{1}{\omega_3^2}\frac{R^2}{Q} - \frac{1}{\alpha}\frac{\sin^2\theta}{\omega_3^2} + 2$$

$$\alpha = \frac{\cos^2\theta}{\omega_1^2} + \frac{1}{\omega_2^2} + \frac{\sin^2\theta}{\omega_3^2}$$

$$\gamma = \frac{1}{\omega_1^2} - \frac{1}{\omega_3^2}$$

$$\omega_3 = nc\tau$$

and ω_1 and ω_2 are the pump and probe beam waists, n is the sample refractive index, τ is the pump and probe pulse duration.

Figure 3.5 shows a plot of time resolution for different experimental parameters with n=1.5. The time resolution for the usual collinear pump-probe arrangement corresponds to zero crossing angle and is decided by the pulse duration only. When the crossing angle is nonzero, time resolution degraded as the plots show. In our experiment, the beam diameters are about 50 μm and the largest crossing angle is about 10-15°. It can be seen from the plot that the time resolution is not significantly degraded: with a pulse duration of 50 fs a time resolution of about 60 fs can be achieved.

The initial alignment of the 16 beam device was time consuming. However, since the device is very robust, the alignment was preserved very well even after the whole device was moved around the lab. Timing among the 16 pulses was measured through performing an optical Kerr effect experiment for each individual probe with the pump in a sample which gave large electronic response. The experiments were carried out in a conventional way by using a photodiode to monitor one probe at a time. For convenience, we run the delay line on the pump beam instead of the probe beam to avoid aligning the 16

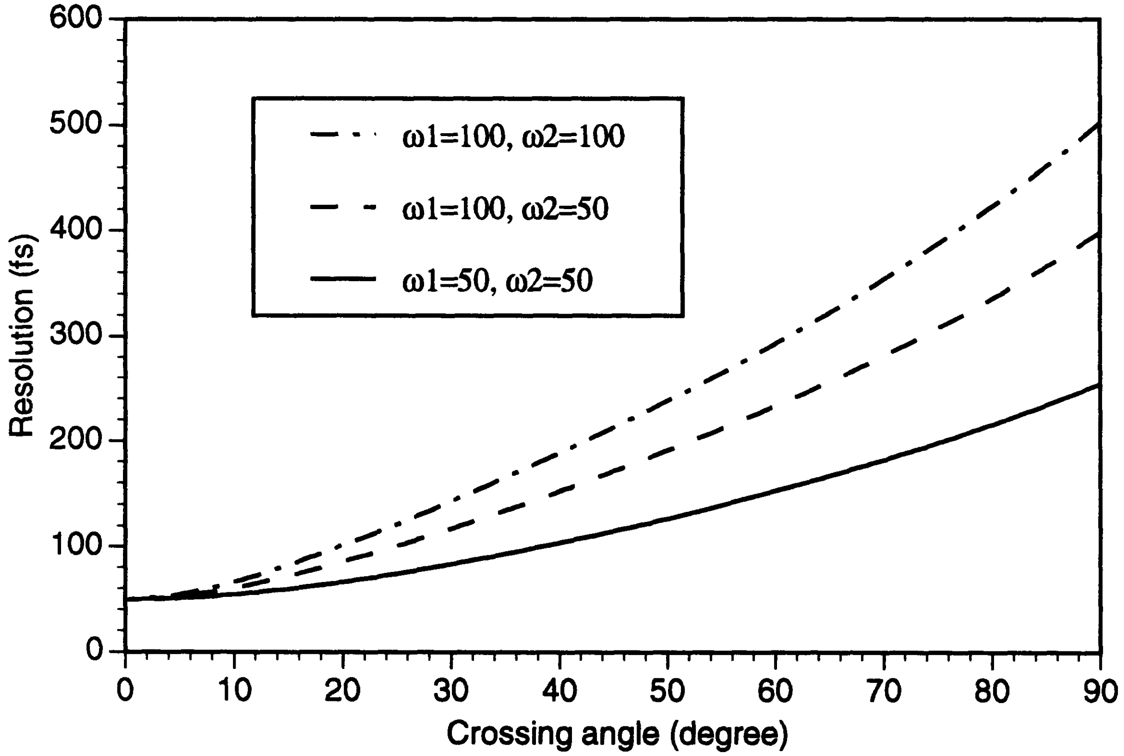

Figure 3.5. Resolution vs. crossing angle for several pump and probe beam size combinations. Pulse durations: 50 fs.

beam device too frequently. After the timing was defined, a sample was put into the position where the nonlinear optical glass was and a single shot data set was collected on the CCD detector.

The single shot detection scheme using the 16-beam method has been tested with two experiments. Fig. 3.6 shows the single shot data of optical bleaching of malachite green in methanol. The solid line is the signal obtained in the same sample through the conventional way using only one of the 16 beams as probe. The data were consistent with the results from the conventional method. Several different delay line settings have been used to demonstrate the robustness of the method. Fig. 3.7 presents another data set. Data points are connected with lines to show that they are distributed around the true dynamics curve.

In the second set of experiments, we apply the method to measure optical Kerr effect in liquid to demonstrate the method's capability for single shot polarization sensitive spectroscopy. A 2 inch diameter sheet polarizer was introduced just before the last lens which focuses the 17 beams (16 probe beams and 1 pump beam) into the sample. A half waveplate and a polarizer were introduced into the pump beam path. At the sample the pump had a polarization 45° to that of the probe beams. Another sheet polarizer 90° to the first one was introduced just after the collimating lens. Fig. 3.8 shows the single shot data of optical Kerr effect in CS_2. These single shot results were also consistent with the results from conventional method. To demonstrate the robustness of the setup, single shot data from other different settings are presented in Fig. 3.9.

There are several factors in this method which need special consideration. All of them are related to the geometrical arrangement of the pump and probe beams, since the 16 probe beams are separated spatially and they overlap with the pump with different angles. First, the difference in crossing angles will cause the signal level to be different for each individual probe beam. It is important to use a standard sample to calibrate this effect.

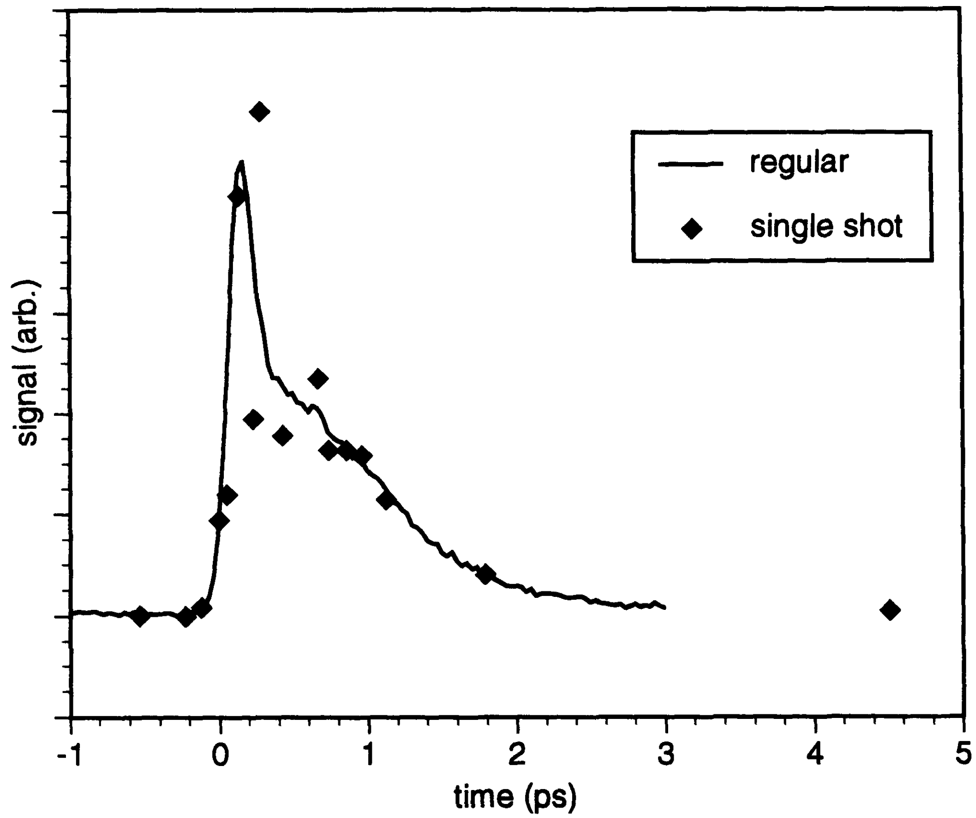

Figure 3.6. Femtosecond single shot optical bleaching data in malachite green in methanol. Solid line: data from regular experiment; Diamond: single shot data.

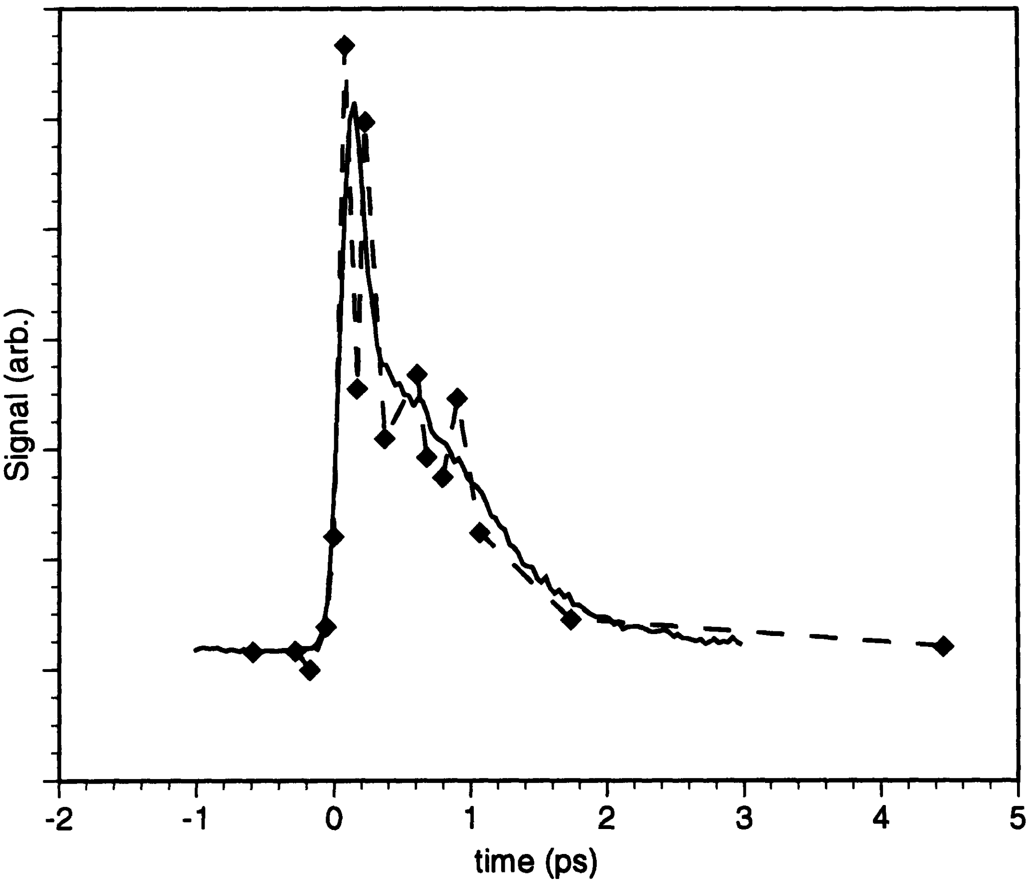

Figure 3.7. Single shot data of optical bleaching experiment in malachite green in methanol. Solid line: regular experiment data; Diamond: single shot data; Dashed line: connecting single shot data points.

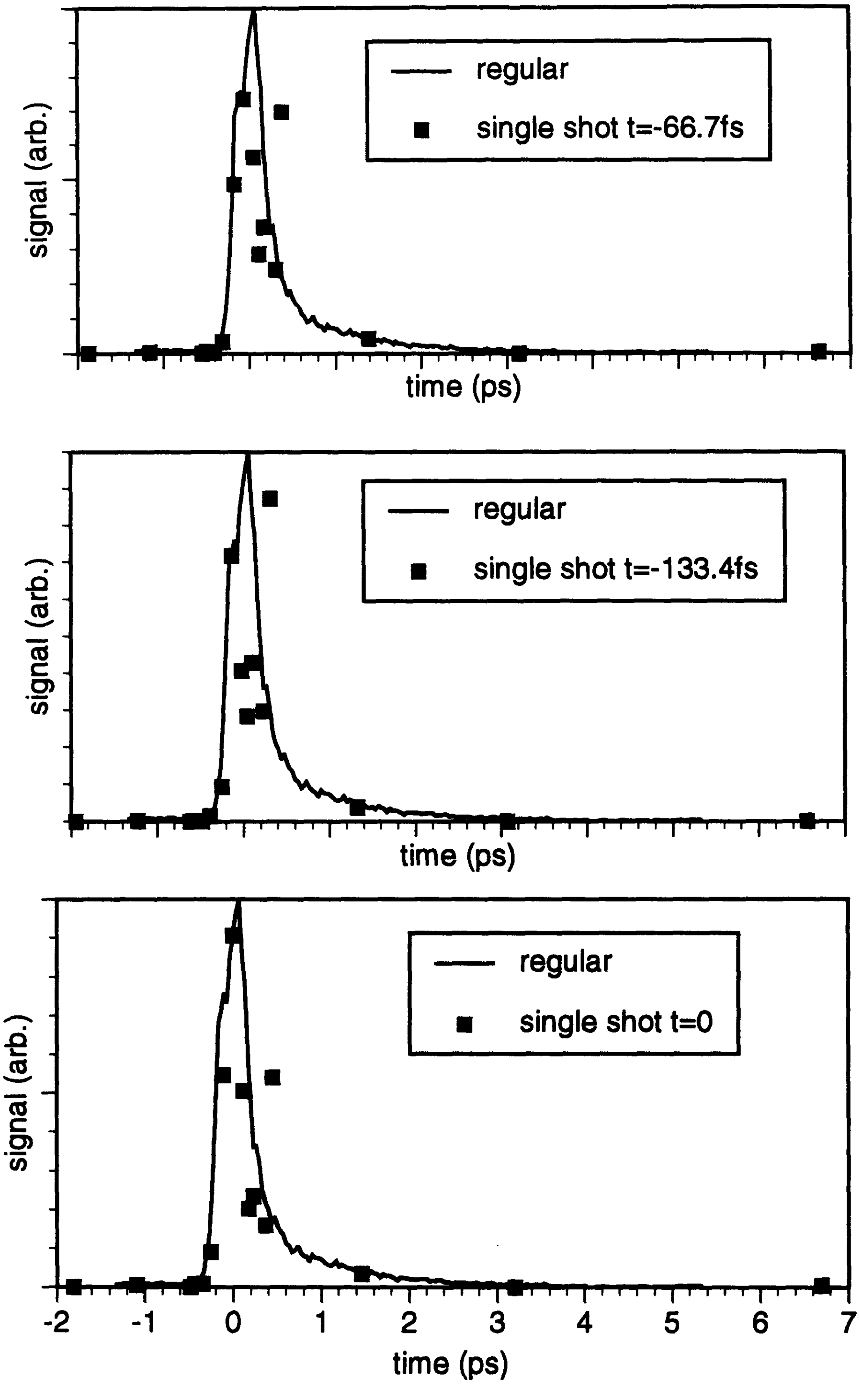

Figure 3.8. Femtosecond single shot experiment of optical Kerr effect in CS_2.

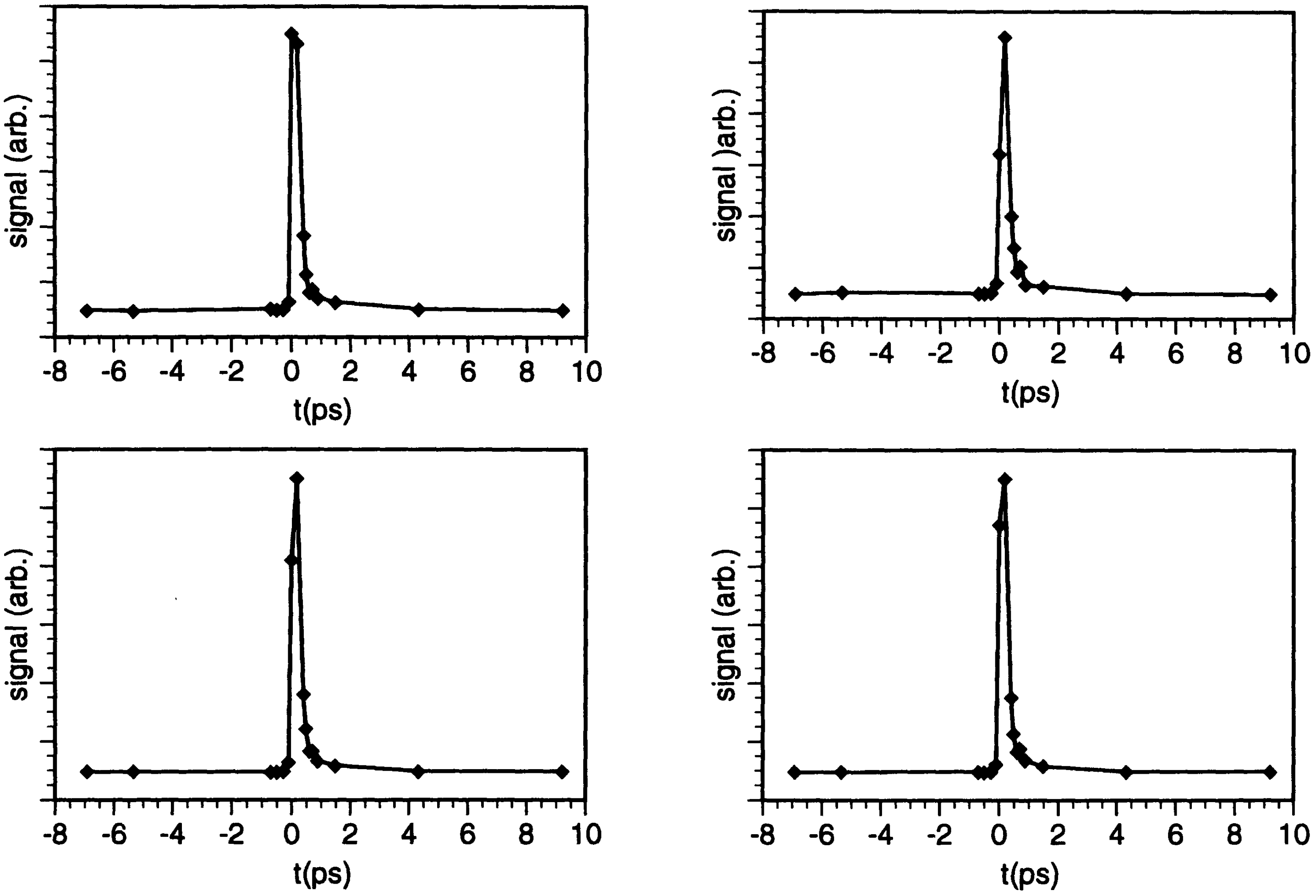

Figure 3.9. Some representative single-shot data of optical Kerr effect in CS_2. Solid lines connect the data points to guide eyes.

The second problem is the possibility that part of the pump pulse may be scattered into those probe pulses which temporally overlap with the pump pulse and generate the so called "coherence spikes" [3.5]. It is also possible for those probe pulses temporally overlapped with the pump pulse to form gratings with the pump and diffract other probe pulses. This problem is generally difficult to correct because the precise crossing angles are usually not known. The easiest way may be to avoid it by carrying out the experiment with different pump and probe wavelengths. The 16-beam device is currently optimized for 620 nm, so we need to choose the pump to be a different wavelength.

Although the method has been shown to work, there are several limitations. The first is that only 16 points along the time axis could be sampled after each excitation pulse. This makes the method more of a way of achieving internal calibration to facilitate experiment on a lot of fresh sample spot than as a way of getting the complete time dependent dynamical information in a single shot. The second limitation is that a set of 15 beamsplitters are needed for each probing wavelength. This is both costly and inconvenient since many probing wavelengths are generally needed to characterize the dynamics of a photochemical reaction.

3.3 SPATIAL ENCODING METHOD

Another method which has been demonstrated in this lab recently is to make use of the spatial dimension of the pump and probe beam [3.6]. Fig. 3.10 illustrates the basic concept of this method. The pump and probe beams were cylindrically focused into two stripes. They cross each other in the sample at an angle. Different parts of the pump and probe beam will overlap at different times. By resolving the spatial profile of the probe pulse, temporal information encoded onto it could be recovered. Figure 3.11 shows the

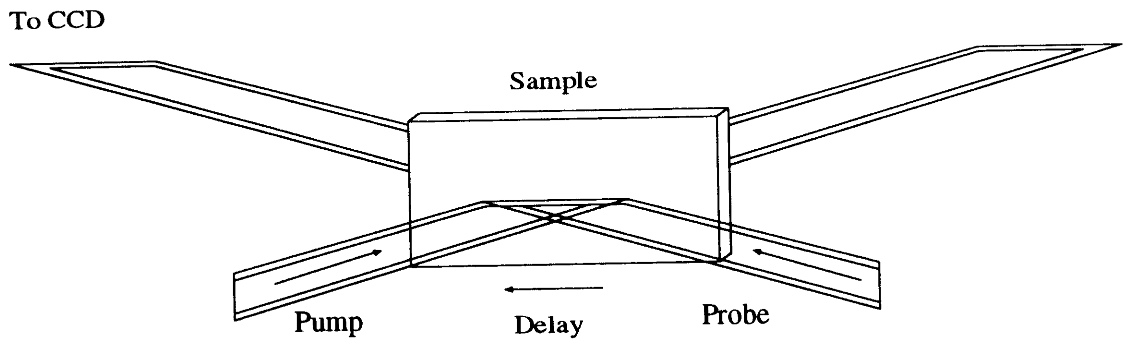

Figure 3.10. Illustration of the concept of the spatial encoding single shot method

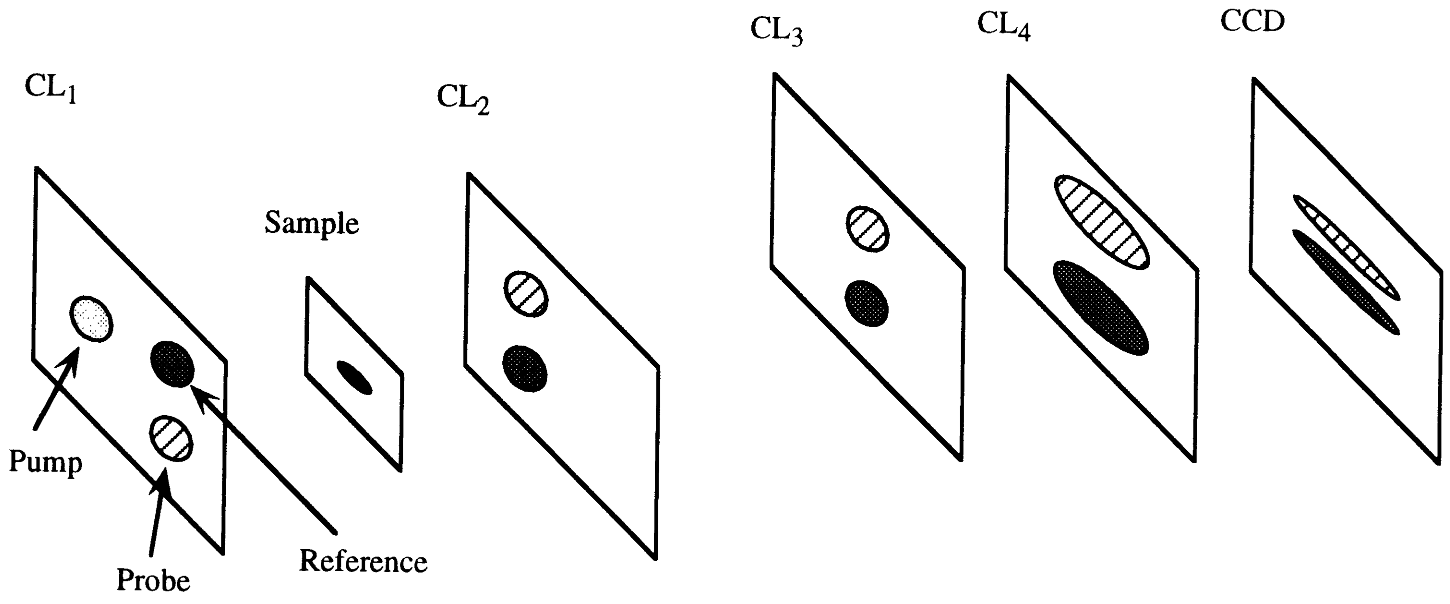

Figure 3.11. Beam arrangement for the spatial encoding single shot method.

optical arrangement of the method and Fig. 3.12 shows the experimental setup using this method. The specifications of optical elements are listed in table 3.1. The beam spatial

Table 3.1. Optical elements and specifications for spatial encoding single shot method.

Symbol	Specifications
L_1	spherical lens, f.l. = 40cm
BBO	0.5mm thick (BSA Technology)
KDP	0.8mm thick (Cleveland Crystals)
DB	dichroic beamsplitter, reflect 350-435nm (90%) and transmit 700-900nm (80%) (CVI)
L_2	spherical lens, f.l. = 40cm
L_3	spherical lens, f.l. = 40cm
L_4	spherical lens, f.l. = 40cm
L_5	spherical lens, f.l. = 40cm
L_6	spherical lens, f.l. = 40cm
L_7	spherical lens, f.l. = 30cm
A_1	diamond pinhole, 100μm (Fort Wayne Wire Die)
A_2	diamond pinhole, 100μm (Fort Wayne Wire Die)
BS	50% beamsplitter
CL_1	cylindrical lens, f.l. = 5 or 10cm
CL_2	cylindrical lens, f.l. = 5 or 10cm
CL_3	cylindrical lens, f.l. = 30cm
CL_4	cylindrical lens, f.l. = 15cm
S	sample

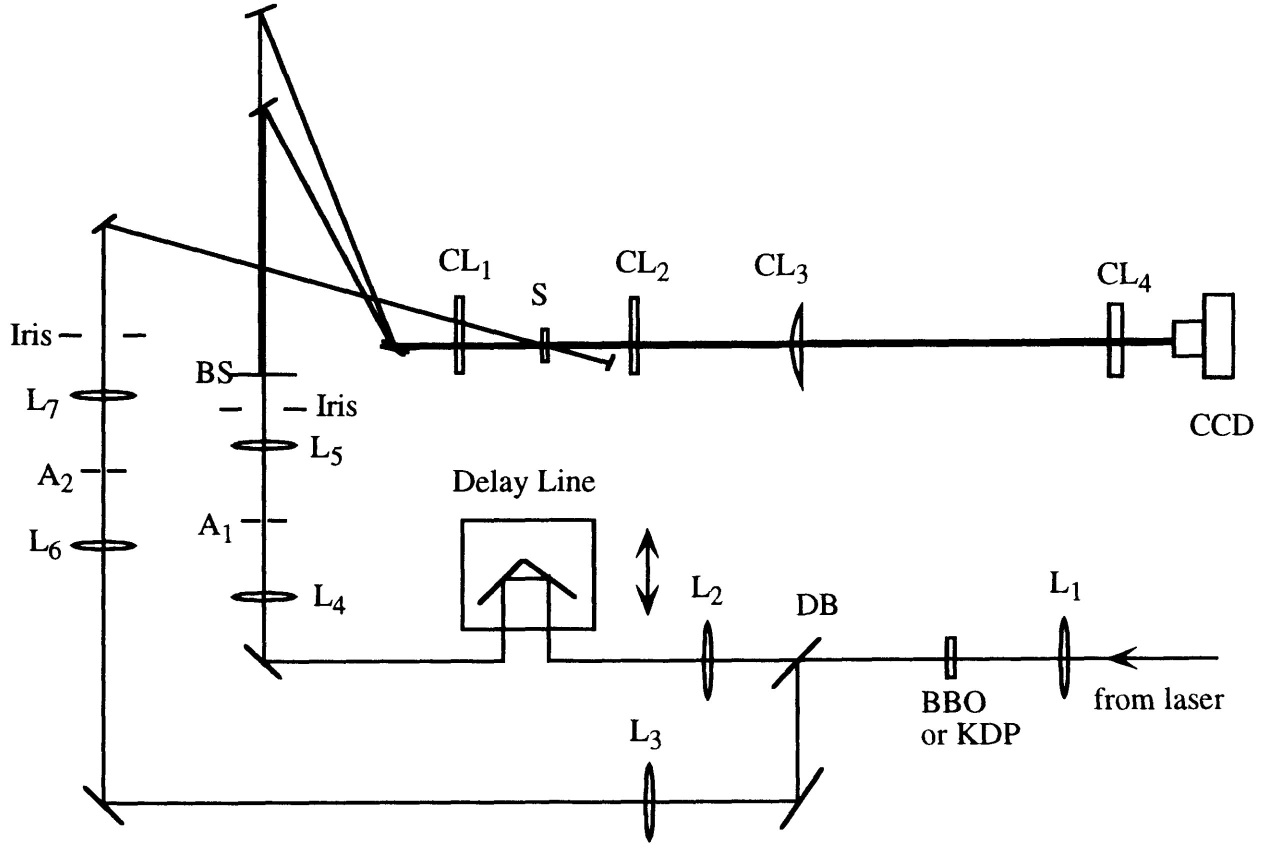

Figure 3.12. Experimental setup using spatial encoding single shot method.

quality and the alignment of the probe and reference beams are crucial in getting correct results. The two apertures A_1 and A_2 were used to spatially filter the pump and probe beams to guarantee good spatial quality. The two irises were used to block the diffraction rings. Beamsplitter BS divided the probe beam into two equal intensity parts, one used as probe and the other used as reference. These two beams were aligned to propagate in exactly the same direction with the reference beam on top of the probe beam. The reference beam traveled a shorter distance than both the pump and the probe beam to make sure that it reached the sample earlier all the time. The pump, probe, and the reference beam were focused to the sample by a 5 or 10 cm cylindrical lens CL_1. After the sample an identical cylindrical lens CL_2 recollimated the probe and the reference beam back to their original sizes and imaged to the CCD camera by cylindrical lenses CL_3 and CL_4. A Ronchi ruling was put at the sample position while the images were examined on the CCD to ensure that the wavefronts were not tilted. Currently, the images are examined by eye. It will be more precise and convenient if the computer does this examination automatically. (This would be a task well suited for computer since the CCD detector forms a 2D grid which allows very precise and convenient determination of the orientation and fringe spacing of the Ronchi ruling image.) After the alignment, the sample was inserted and single shot images of probe and reference spatial profiles were collected. A series of probe spatial images at different delay times were recorded. The signal was obtained through subtracting the reference to get a probe signal spatial profile and then normalizing this probe signal spatial profile to that from a sample with constant signal (This is actually the pump spatial profile.). The signals from different delay were used to calibrate the time axis. Fig. 3.13 presents representative data using this technique. This method provides complete information within the temporal range defined by the spatial size of the pump and probe beams as well as the angle between them. However, due to its nature of utilizing the spatial profile to carry the temporal

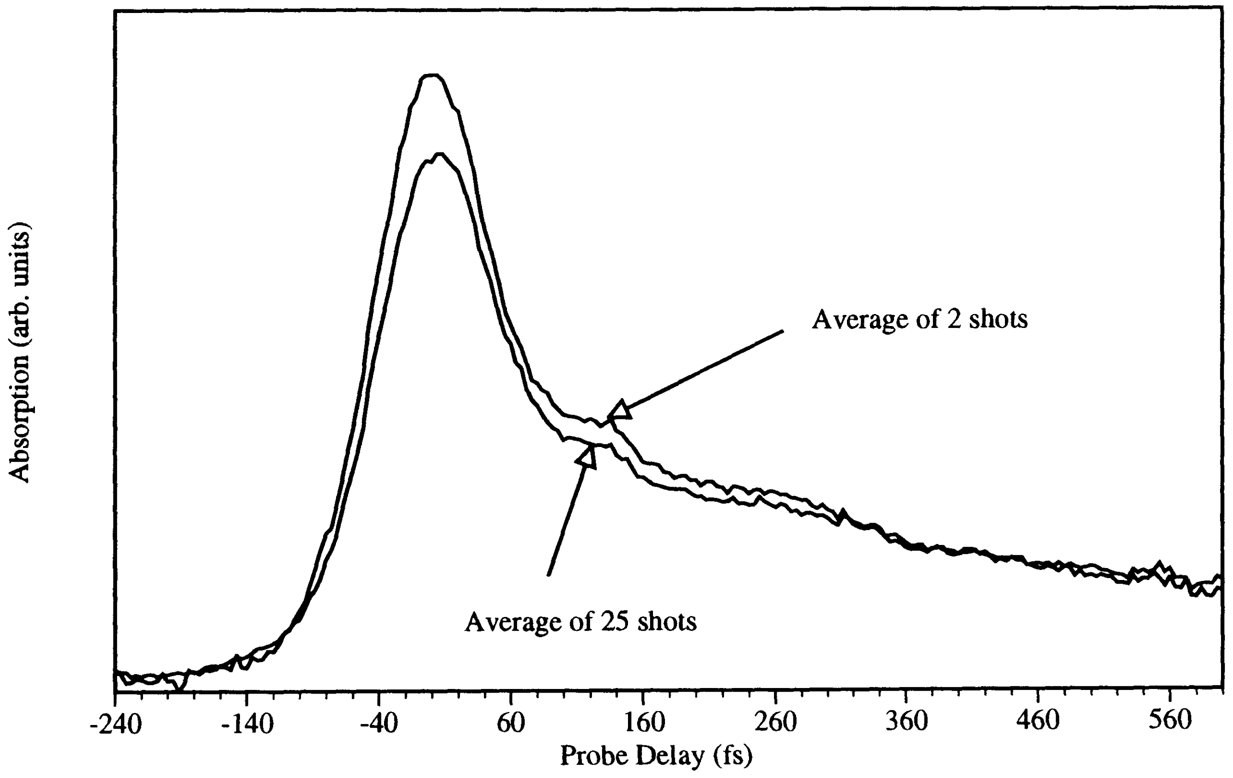

Figure 3.13. Representative single shot data in malachite green in methonal using the spatial encoding method.

information, high quality solid samples which have uniform volume at least of several millimeters in one dimension are required.

3.4 FUTURE DEVELOPMENT

Although we have seen great progress in the development of single shot femtosecond spectroscopy, the area is still in its very early stage. A lot of effort is needed to make single shot methodology a quantitative and convenient tool in studying a variety of important chemical and physical processes in solids or any other nonflowable samples. One possible important improvement may be to use a long pulse (20 picoseconds long, for example) as probe to interrogate the sample after the excitation. This long pulse can be derived from the femtosecond pulse by narrowing its spectral width with a slit for example. It can also be obtained with more sophisticated methods [3.7]. The temporal information will be encoded into the temporal profile of this long pulse. Then use some other optical methods to recover this information.

One possible method is to use the 16 pulses to recover the dynamical information imprinted in the long probe pulse. It will also allow us to use the device optimized for one wavelength, such as 620 nm, to do experiments which require other probing wavelengths. Since the intensity of the long probe pulse is usually very low, it may not be possible to use it as a gating pulse. We may be able to use 16 relatively strong pulses to upconvert the long probe pulse under tangential phase matching condition (Appendix). It is also possible to recover the information by cross-correlating the modulated long pulse with its unmodulated replica in a doubling crystal and spatially resolving the generated second harmonic in much the same way as in a single shot autocorrelator [3.8-3.10]. The method would combine the advantage of having continuous delay as offered by the spatial encoding method and the advantage of probing a single spot on the sample as offered by the multiple probe method.

This separation of probing process into a long pulse probing step which collects the dynamical information in a single shot and a characterization step which recovers the information carried by the long probe pulse would make single shot femtosecond spectroscopy routine. The characterization of the long pulse which carries the sample dynamics information can be carried out with nonlinear crystals which generally have the best optical quality. Samples with only small high quality areas can also be examined because the pump and probe process at the sample requires only a single spot.

4. CHEMICAL REACTION DYNAMICS OF 2,5-DISTYRLPYRAZINE (DSP) IN THE CRYSTAL PHASE

4.1. INTRODUCTION

Chemical reaction dynamics in solids has many unique features that are associated with this particular phase only. For example, solid phase is the most densely packed phase for most substances. This would provide the opportunity of exploring parameter space beyond liquid phase for solvent effects which depend strongly on the solvent structure. We will discuss this in the next section in association with the studies of solvent cage effect. Solids also form ordered forms, such as crystalline forms, in which reactant molecules are aligned to each other in a specific way. This special arrangement of reactant molecules may play a decisive role in dictating the reaction dynamics [4.1-4.3]. Examples include oriented bimolecular reactions, such as photodimerizations, among others. In these reactions, new bonds form between a pair of molecules upon photoexcitation. The reaction happens only when the two reactants are close to each other and aligned properly. In gases and liquid solutions this is usually not the case even when reactant molecules form van der Waals associations, because the special alignment and distance required for the reaction to happen may not be the most favorable configuration for the molecular pair itself. But in a crystal this special arrangement may be maintained as a result of stabilizing the crystal as a whole.

There are many examples of this kind of topochemical lattice control on chemical reactions in solids. Some of them have been used in synthesis [4.1, 4.3]. One example is the synthesizing of an organic nonlinear optical material polydiacetylene in solid state [4.1].

The other unique feature of solid state reactions is the collectiveness of molecular motions in a lattice. These collective motions, such as phonons or excitons, could have certain long range effects on a chemical reaction. Unlike in a liquid solution where only the immediate solvent neighbors have significant influences on the reactants and products while far away solvent molecules' interactions with the reacting molecules tend to cancel each other (at least in systems with only short range interactions to be considered here), in a solid the reactants could feel the influence of far away molecules through these collective motions (even in systems with only short range interactions such as molecular crystals). For example, thermal excitation in a crystal lattice results in lattice phonons which are highly directional, i.e., energy being confined to modes along well defined directions. This would facilitate the deposition of thermal energy into a reaction coordinate and enhance reaction rates. Concepts such as phonon assisted chemical reactions have been developed [4.1]. It is also possible to achieve collective chemical reaction in crystal since molecules in all unit cells tend to move in coordination. Molecular excitations could also propagate along the lattice to enhance reactivity. In photoreactions, photoinduced electronic excitations are precursors of a chemical reaction. These excitations could move more easily from one site to another in a crystal lattice than in solutions to increase the reaction rate.

The crystal phase also allows modification of interactions between molecular pairs in a controlled way. For example, by varying the pressure on the solid sample it is possible to modify the distance and sometimes alignment of the molecular pairs. This will allow us to study the role these factors play in, for example a bimolecular reaction, in a more systematic manner.

Due to their fundamental and practical importance, chemical reactions in solid state have been studied extensively. These studies, including spectroscopic, X-ray, etc., have revealed invaluable information about the reaction dynamics in solid states. However, there are still many unanswered questions which require time-resolved studies. Since many solid state reactions involve several factors, time-resolved spectroscopic methods would allow us to separate them temporally. For example, in order to study the role play by lattice vibrations (phonons) in a solid state reaction, Raman or other spectroscopic methods were used to monitor the phonon frequency change during the course of the reaction. Phonon assistance was deduced if there was a significant frequency change such as mode softening of a particular lattice mode during a reaction. This sometimes is not a valid approach because the frequency change of a lattice mode could quite possibly be a result of the reaction rather than to assist the reaction. It is important to know if the mode softening comes before or after the reaction. A time domain method is required to achieve this. Other examples include the reaction of DSP which we will discuss in this section. Two electronic transitions may be involved in this reaction, in a time-resolved experiment the temporal relation of the two electronic transitions may be examined.

From a more general point of view, bond formation has been more difficult to deal with in gas phase and liquid solutions than bond fission due to the diffusion process prior to the encounter of the two reactants and the bond forming process. In case of bond fission, such as photodissociation, the reaction starting time is precisely defined by the excitation pulse. In case of bond formation, however, the time it takes for a pair of reactants to find each other would be on the picosecond to nanosecond time scale. This makes it more complicated if our primary interests are to study the dynamics of bond forming processes when the two reactants are already in position. One way to solve this problem is to use a precursor [4.4-4.7]. Solid state samples offer another opportunity by fixing the reactants in the vicinity.

Due to the difficulties mentioned in the last section, femtosecond spectroscopic studies of reactive solids have not been undertaken. With our recent success in developing the single shot femtosecond spectroscopic methods, experiments with these materials have been started. In this section, we will present preliminary results of a particularly interesting system, 2,5-distyrylpyrazine. Due to the fact that this technique has just been developed and still in its initial stage, a full understanding of the dynamics of DSP (or any other systems) is yet to come. The significance here is that this is the first ever femtosecond spectroscopic experiment on a reactive solid. By this we have demonstrated that time-resolved spectroscopy of irreversible solid state reaction is possible. This has opened up the door to a whole new field that was not possible before.

4.2. 2,5-DISTYRYLPYRAZINE (DSP): PROPERTIES AND REACTIONS

2,5-distyrylpyrazine (DSP) has been a prototype solid state reaction. The molecule was first synthesized by Franke in 1905 [4.8]. In 1958, it was found that DSP could be converted into a polymer in solid phase [4.9]. The molecular structure and the reaction are illustrated in Fig. 4.1. Since the late 1960s, this compound and related diolefin compounds such as 1,4-bis[b-pyridyl-(2)-vinyl]bensene (P2VB) have been subjected to extensive study [4.10, 4.11]. Further investigation showed that there was a wavelength dependence of this reaction [4.12]. When irradiated with light of wavelength longer than about 400 nm, two or more molecules underwent a four-center addition type of reaction where one or both double bonds in a molecule opened to form an oligomer composed of an average of 3

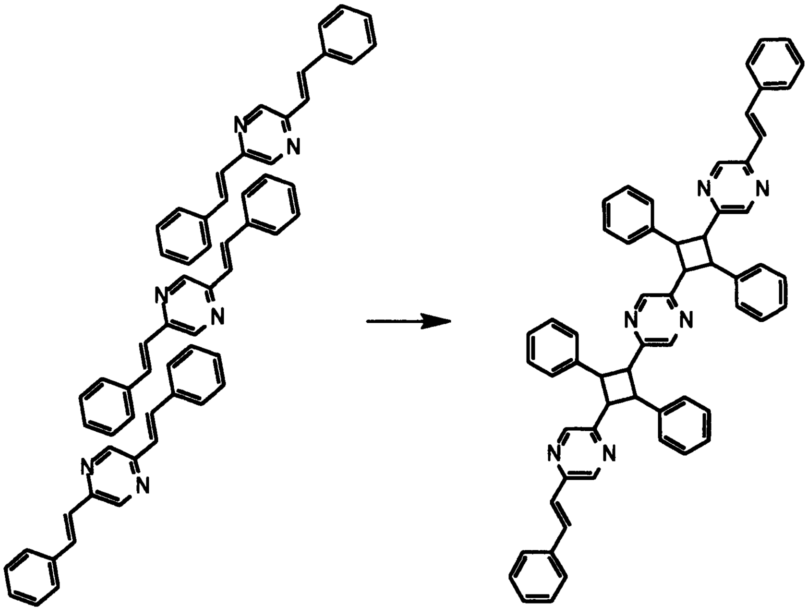

Figure 4.1. The four-center addition reaction of DSP.

monomer units (molecular weight about 900). The oligomer crystal lattice was very close to the original monomer crystal lattice that during the reaction the single crystal configuration was preserved. When the oligomer crystal was further irradiated with light of wavelength shorter than 400 nm, it reacted to form a high polymer. Again the single crystal structure of oligomers transformed into a single crystal of polymers. The monomer crystal could also be converted directly into a polymer crystal by irradiation with light of wavelength shorter than 400 nm without the intermediate oligomer stage. In solution, photo irradiation produced only DSP oligomers. Further irradiation with shorter wavelength light caused dissociation of the oligomers rather than formation of polymers. Oligomers produced in solution crystallized into a different form of crystal and would not further polymerize by light of short wavelengths. A schematic illustration of the reaction pathways is presented in Fig. 4.2 [4.12]. Recently, very detailed spectroscopic studies have been performed on DSP [4.13-4.20]. Since this system demonstrates many of the special features associated with a

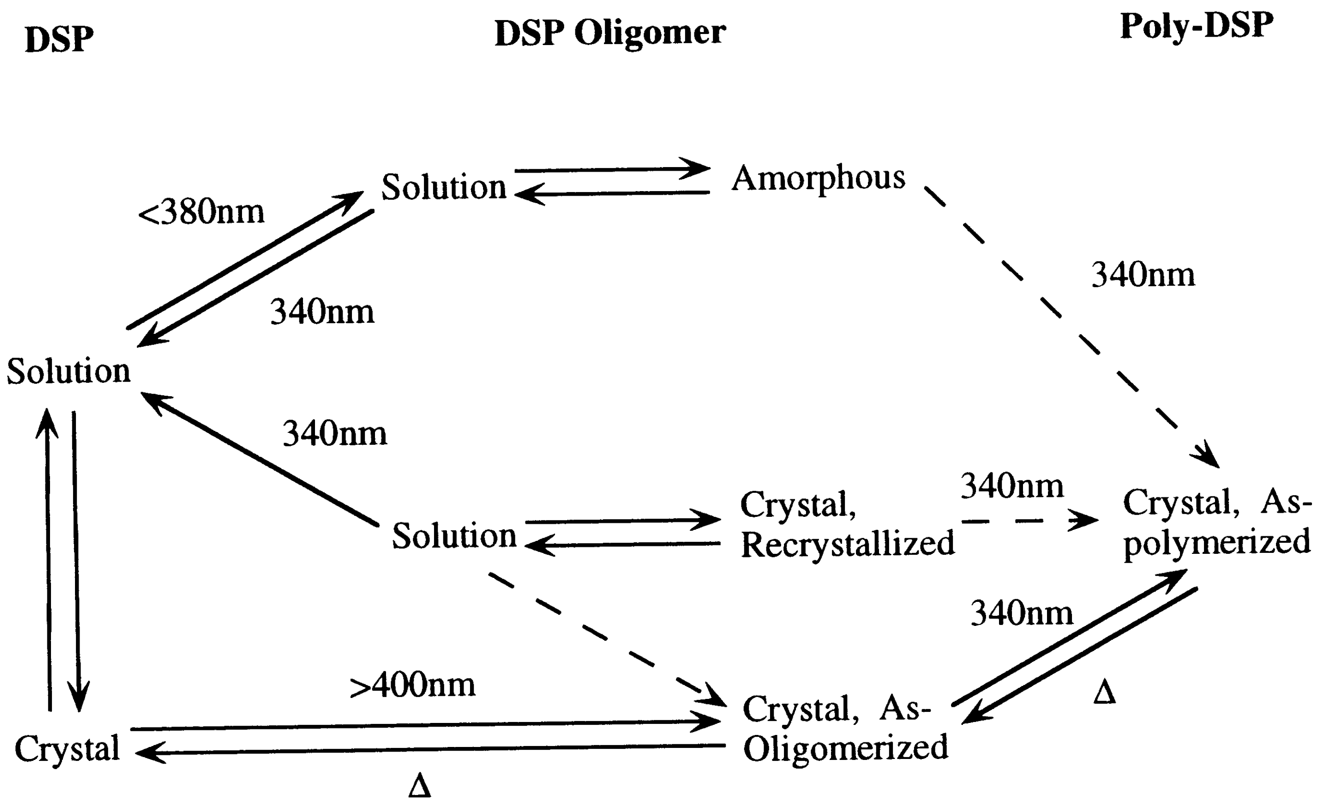

Figure 4.2 Reaction Pathways of DSP in solution and in crystal.

——→ Reaction — —→ No Reaction

solid state reaction, such as topochemical control and collective motion enhancement of reactivity, it is one of the best candidates to be studied. Fig. 4.3 and Fig. 4.4 reproduce the absorption spectra of DSP in solutions and in the crystalline solid [4.17].

4.2.1 Topochemical Principle and the Crystal Structures of DSP

The concept of topochemical principle was introduced by Cohen and Schmidt [4.21] in the studies of the effect of the reactant lattice geometry on solid-state chemical reactions. They postulated that "the reaction in the solid state occurs with the minimum amount of atomic or molecular movement. This postulate implies that solid-state reactions are controlled by the relatively fixed distances and orientations, determined by the crystal structure, between potentially reactive centers." [4.21]. In a series of papers following the above mentioned one, this postulate was applied to a variety of solid state reactions including the type of reaction that DSP belongs to [4.22, 4.23]. This postulate has been very useful in rationalizing the reactivity difference in a solid state reaction as compared to the reaction in solution phase as well as differences in reactivity among different crystal structures. It could be regarded as a statement of the lattice control on reactions in solids. DSP has been one of the examples of this kind of topochemical lattice control.

DSP forms two different forms of crystals. Table 4.1 lists the crystallographic parameters of these two forms of crystals [4.24, 4.25]. One form is photoreactive while the other form is photostable. The photoreactive form, which is called the α-polymorphic form from the classification by Schmidt [4.21], has a structure illustrated in Fig. 4.5 [4.24]. In this crystallographic form, the monomer molecule is very close to a planar configuration with a dihedral angle of 12.09° between the center pyrazine ring and each of the two benzene rings. Molecules are arranged along the c-axis in such a way that their reactive double bonds are stacked antiparallelly on top of each other with a distance of 3.939 $\mathring{A}$.

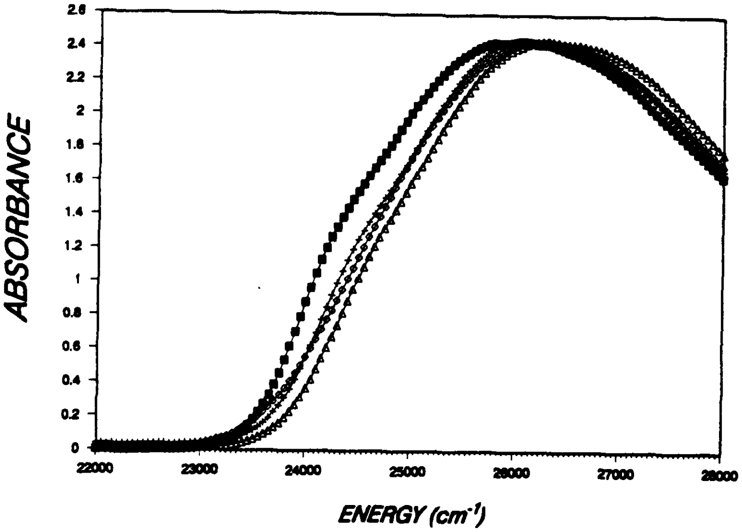

Figure 4.3 Solution spectra of DSP in bezene (filled square), in methanol (diamond), in tetrahydrofuran (cross), and in acetonitrile (triangle). [From Reference 4.17]

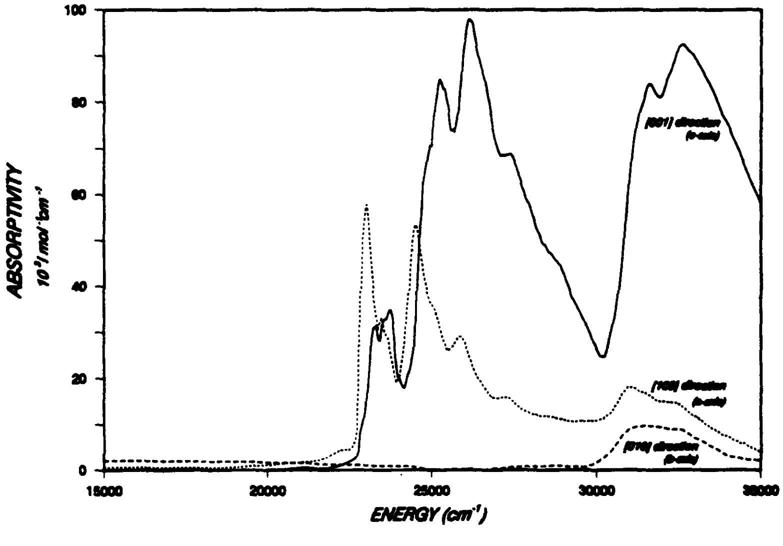

Figure 4.4 The polarized, low-temperature absorption spectra of the DSP monomer crystal. [From Reference 4.17]

The angle between the molecular long axis and the crystal c-axis is 30°. The oligomerization or polymerization happens along the c-axis direction with the final products of either oligomers or polymers aligning along the c-axis. Since the displacements of atomic groups in a molecule during the reaction are quite small, the stack structure of the monomer lattice transforms into a stack of oligomers or a polymer chain with single crystallinity well preserved from the monomer to the high polymer.

The other crystallographic form is called the γ-form which is a needle-shaped crystal grown from sublimation [4.25]. In the γ-form the monomer molecule assumes a much different structure than in the α-form. Although the bond lengths and angles are similar to those in the α-form, the relative rotations of the benzene rings and the ethylene groups to the center pyrazine ring are significantly larger than in the α-form. The dihedral angles between the pyrazine ring and the two benzene rings are 23.5° and 28.9° respectively in opposite direction. This makes the dihedral angle between the two benzene rings 52.3° so that the molecule is not in a planar configuration at all. The crystal structure is also different from the crystal structure of the α-form. (Fig. 4.6) The molecules are

Table 4.1. Crystallographic parameters of the α- and γ-forms of DSP

	α-form	γ-form
Crystal System	Orthorhombic	Monoclinic
Space Group	Pbca	$P2_1/a$
a	20.638 Å	13.833 Å
b	9.599 Å	18.615 Å
c	7.655 Å	5.823 Å
Z	4	4
Density	1.257 g/cm^3	1.269 g/cm^3

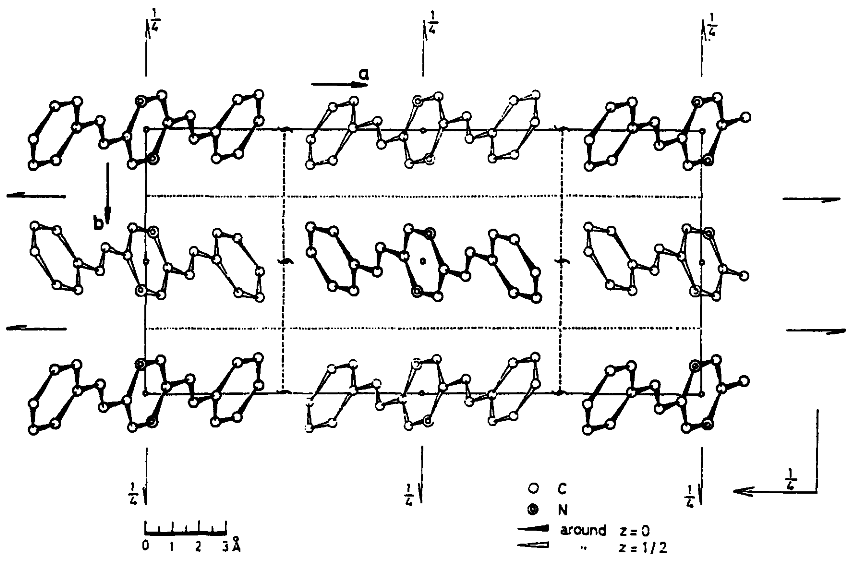

The crystal structure viewed along the *c*-axis.

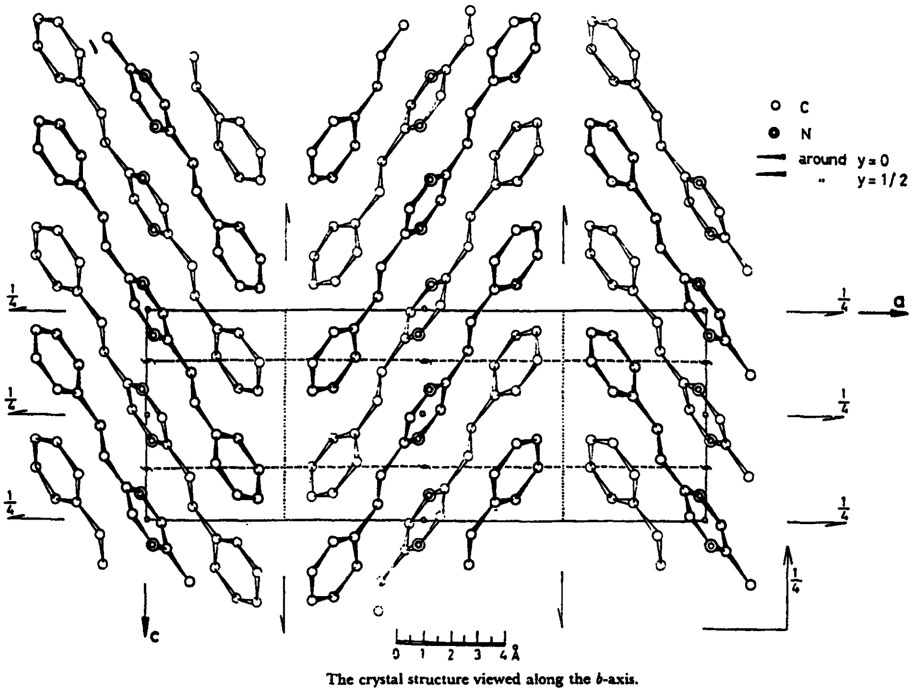

The crystal structure viewed along the *b*-axis.

Figure 4.5 The molecular arrangement in the α-form DSP crystal. [From Reference 4.24].

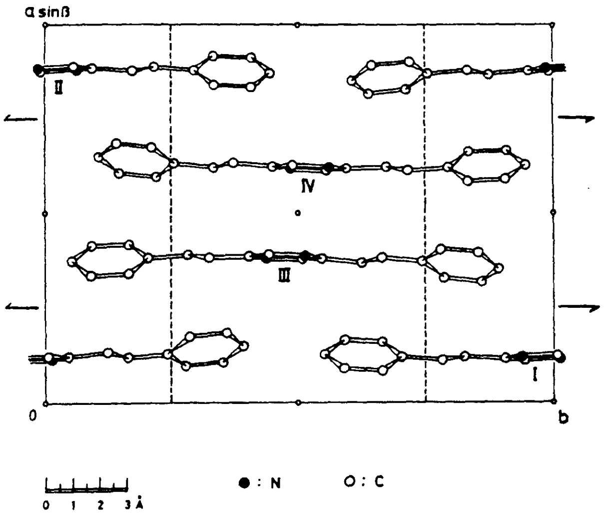

The crystal structure viewed along c.

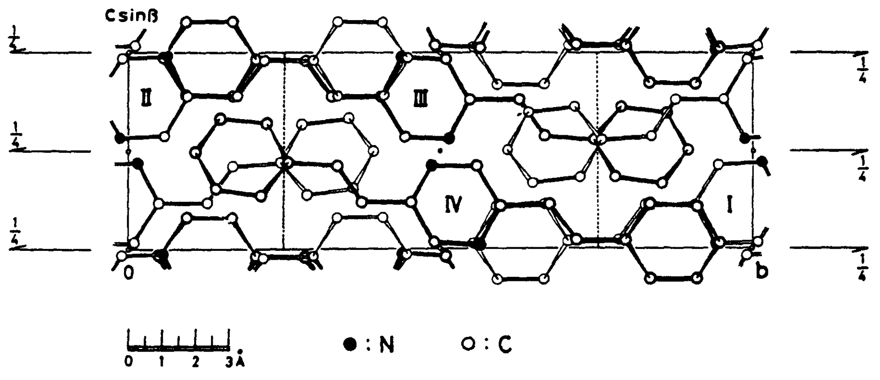

The crystal structure viewed along a.

Figure 4.6 The molecular arrangement in the γ-form DSP crystal. [From Reference 4.25].

arranged into layers perpendicular to the crystal a-axis. The closest double bonds are in molecules in adjacent layers. However, these molecules are not in a face-to-face configuration as in the α-form and the reactive double bonds are not parallel to each other [4.25]. Although the shortest distance between these closest double bonds in the γ-form (4.187 Å) is only slightly longer than that in the α-form, reaction would require large deformation of molecular layers and hence is prohibited. One the other hand, it was demonstrated that the γ-form DSP crystal underwent a phase transition when heated to about 130°C to α-form which would react to form single-crystal polymer when irradiated with light of suitable wavelengths [4.26].

This has been one of the classic demonstrations of lattice control of chemical reactions in solid state. The reactivity difference between the two crystallographic forms of the same molecule demonstrates the importance of factors other than chemical properties of the species in determining the course of chemical reactions.

4.2.2 Electronic and Dynamical Properties of DSP Crystal and the Mechanism of its Reaction

Although the lattice structure plays an important role in determining the reactivity, it is not the only factor. A comparison between the reactivity of DSP and P2VB has revealed other factors in the reaction of DSP. The molecular structures of the two molecules are shown below to be very similar to each other. In solution they have comparable reaction rates (Table 4.2). They also have similar crystal structures. In fact, P2VB has not only an isomorphic crystal structure to DSP but also a reactive double bond separation of 3.910 Å which is shorter than that of DSP. However, the reactivity of DSP is about 30 times larger than the reactivity of P2VB, contrary to the prediction of the static lattice control principle.

This has made more detailed information about the electronic and dynamical properties of the DSP crystal important in understanding its reaction dynamics.

Table 4.2. A comparison of the reactivity of DSP and P2VB [4.27]

	Quantum Yield of Crystal	Yield in THF solution (after 48h irradiation)
DSP	1.2	60%
P2VB	0.04	29%

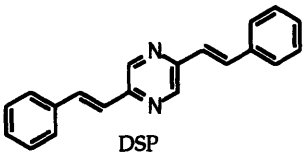

DSP

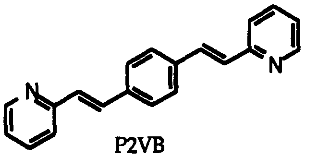

P2VB

The early spectroscopic study of DSP in a Shpol'skii matrix at 4K assigned the molecular transition in the photoreaction wavelength region to be a π–π^* transition to the molecular lowest singlet state of B_u symmetry [4.20]. It was also suggested that the geometry of the first excited state is unchanged as compared to the ground state. More recent studies showed that there are two transitions in this spectral region [4.16]. In addition to the π–π^* transition, there is an n–π^* transition of A_u symmetry which is actually the lowest molecular transition. An n–π^* transition has been shown to be a unique feature of the pyrazine molecule. In pyrazine molecular crystal this transition couples to the lattice phonon mode strongly because the nitrogen lone electron pairs contribute a great deal in determining the crystal packing and therefore the excitation of one of the non-bonding electrons causes the local lattice force field to change significantly [4.28]. On the other hand, in aromatic hydrocarbon crystals it is the intermolecular H-H interactions that contribute the most in determining the crystal packing [4.28, 4.29]. Since the excitation of a π electron does not change this interaction very much, a π-π* transition should couple to the lattice modes only weakly. This has indeed been observed in the DSP crystal. Table 4.3 lists the experimental values of the transition energies, Davydov splittings, and the D-shifts (level shift due to changes in van der Waals interactions upon electronic excitation) of the two transitions of the DSP crystal [4.17]. Hochstrasser and Prasad have shown [4.30] that a comparison of the D-shift term with the exciton splitting can provide information about the nature of the exciton-phonon coupling. A larger D-shift to splitting ratio indicates a more localized exciton with stronger lattice deformation around it, while a smaller D-shift to splitting ratio indicates a more delocalized exciton. From the data in Table 4.3 it can be seen that the n–π* exciton is more localized while the π-π* exciton is delocalized. On the contrary, in P2VB crystal, the only transition in the reaction wavelength region is a π–π* transition. It is the lack of a lattice deformation, i.e. a dynamical lattice control factor, that makes the P2VB's reactivity significantly lower.

Table 4.3 Experimental values of the energies of the n–π* and π–π* transitions of DSP

	n–π*	π–π*
Transition energy (cm^{-1})	24200	24900
D-shift (cm^{-1})	850	900
Davydov splitting (cm^{-1})	250	2200

The reaction mechanism of this system was thus suggested to be a cooperative effect of the two electronic transitions. This hypothesis has been further supported by a two-photon absorption experiment in DSP [4.1]. It was found that prolonged irradiation of DSP at IR wavelengths did not lead to reaction although a considerable amount of DSP fluorescence at the blue wavelength was observed indicating significant two-photon absorption. The n-π* transition induces a deformation along the molecular stack. This deformation traps the delocalized π-π* excitation which can move easily along the molecular stack to the trapping site to form a four member ring. From the lattice control point of view, this is a static lattice effect plus a dynamical lattice effect. Fig. 4.7 illustrates this mechanism in terms of potential energy surface changes along the reaction coordinate. The potential along the reaction coordinate has a barrier of height E which is the energy difference between the reactant pair and the transition state. This barrier height is determined by the relative orientation and distance between the reactants. In a crystal, the static lattice structure will either increase (γ-form) or decrease (α-form) this barrier depending on the molecular arrangement in the crystal lattice. This increase or decrease of barrier height could be a result of either a decrease in the transition state potential energy due to a molecular arrangement that is closer to the transition state energy minimum or an increase of the reactant potential energy due to the lattice effect which forces the reactants to assume a higher energy configuration or both. In the γ-form of the DSP crystal, the molecular arrangement disfavors the product and the transition state configurations and therefore results in an increase in the barrier height. On the other hand, in the α-form of the DSP crystal the molecular arrangement favors the product and the transition state configurations while it disfavors the reactant configuration as compared to the free DSP molecular van der Waals associations, causing an effective decrease of the reaction barrier. The deformation of the lattice structure caused by the n-π* transition may further lower the reaction barrier in favor of reaction. It is to be mentioned that the change in energy curve may be exaggerated. In a photoinduced excited state reaction, since the reactants could be prepared with an energy higher than the excited state barrier height, it is not necessary for the barrier to approach zero to allow fast reaction.

Time-resolved study of this system will allow a direct examination of the role played by the n-π* transition, if any. Since it couples to the lattice strongly, the excitation of this transition alone would have resulted in an excimer with oscillatory motion between its two partners. If the distortion of the lattice assists the reaction, then it should be possible to observe the reaction yield to be modulated by this excimer oscillation.

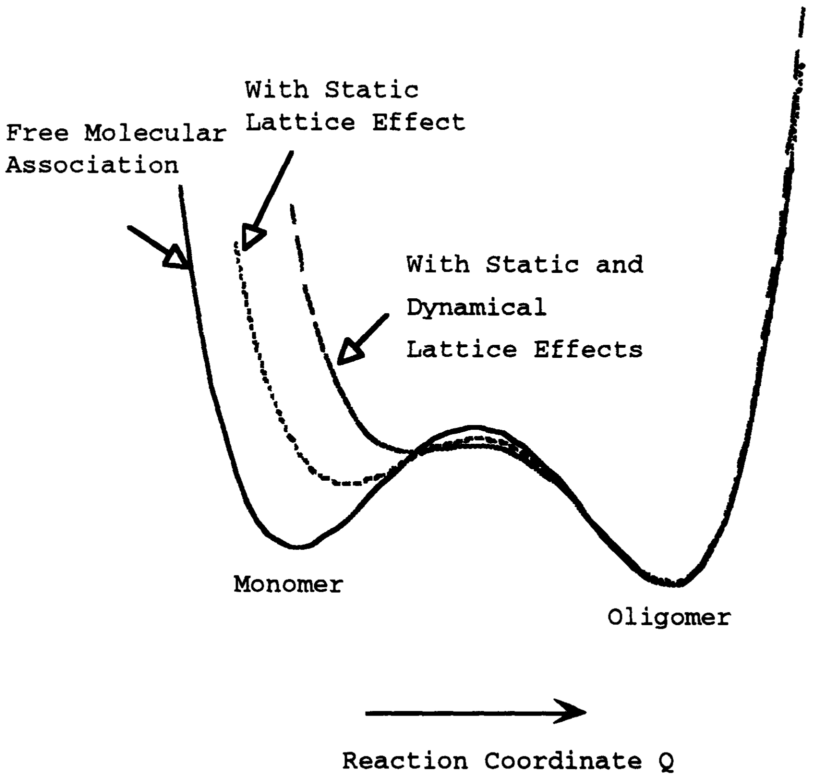

Figure 4.7 Illustration of the DSP potential energy surface in different environment along the reaction coordinate. The changes are due to the modification of the molecular arrangement. They are actually cuts in a multidimensional potential energy surface along different directions

4.3 FEMTOSECOND SPECTROSCOPY OF DSP IN SOLUTION

Pump-probe experiments have been performed on DSP in chloroform solutions first to characterize the spectroscopic property of its excited state. The experiments were carried out with our Ti:Sapphire laser/amplifier. The laser system was run at 810 nm. 70% of the amplified 810 nm light was sent through a KDP crystal to generate the pump wavelength at 405 nm (about 15% efficiency). The rest of the Ti:Sapphire output was focused to a 1 cm thick quartz substrate to generate a white light continuum. 10 nm bandwidth filters were used to obtain the probe wavelengths. A schematic of the setup is shown in Fig. 4.8.

DSP was synthesized by the method of Hasegawa [4.10]. The DSP powder so obtained was purified by sublimation a few times. Solution samples were made by dissolving the purified DSP in chloroform. Sample was flowed through a 1 mm thick quartz cell (NSG).

Fig. 4.9 shows the pump probe results at different probing wavelengths. At shorter wavelengths stimulated emission was observed. This is consistent with the fluorescence transition from the first excited state to ground state in DSP solution which peaks at about 450 nm and extends to about 550 nm [4.13]. At longer probing wavelengths we observed transient absorption by the first excited state to higher lying states. Fig. 4.10 shows a diagrammatic illustration. Note that this is a simplified schematic. There may be several higher lying potential energy surfaces reached by the transient absorption probing process. Changing the concentration from a saturated solution (≈ 10^{-2}M) to a very dilute solution (≈ 10^{-5}M) of DSP showed no changes in the signal temporal features, suggesting that we were seeing the decay dynamics of the excited electronic state itself. Reaction occurs outside our experimental time window of about 7 picoseconds. These experiments also suggested that we can use the Ti:Sapphire fundamental as the probe wavelength in single

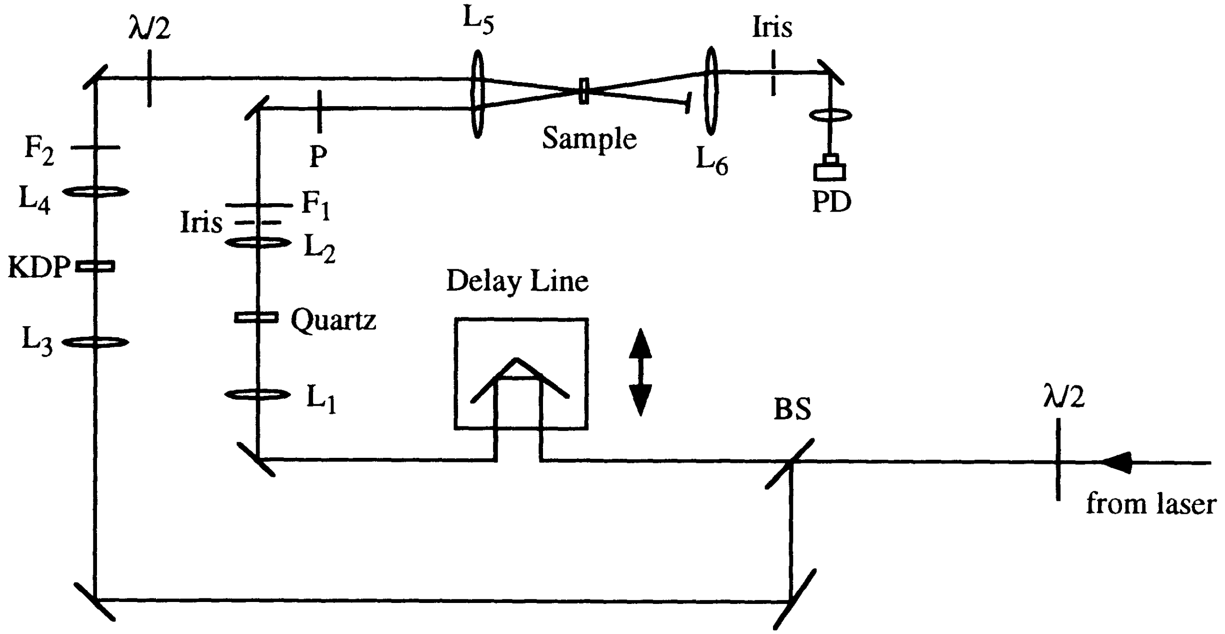

Figure 4.8. Experimental setup for pump-probe experiment in DSP solution. BS: 30% Beamsplitter; L_1: f.l=20cm; L_2: f.l=30cm; L_3: f.l=40cm; L_4: f.l=250cm; L_5: f.l=30cm; L_6: f.l=30cm; F_1: 10nm bandpass filter; F_2: Short pass filter; P: Polarizer

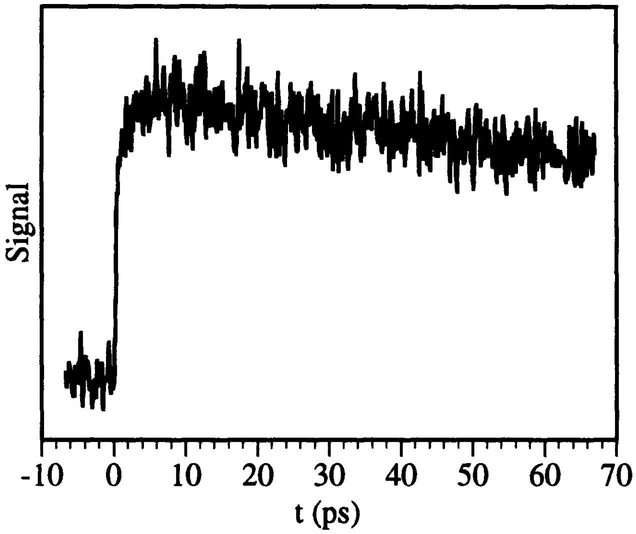

Figure 4.9 a). Transient stimulated emission of DSP in chloroform. Pump 405 nm, Probe 500 nm.

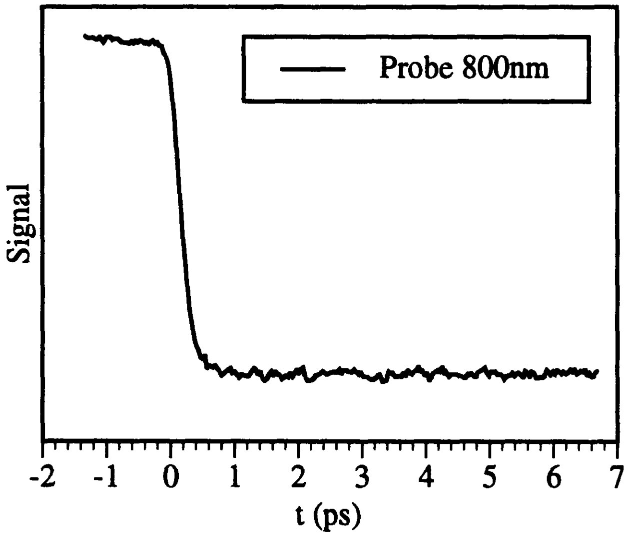

Figure 4.9 b) Transient absorption of DSP in chloroform. Pump 405 nm.

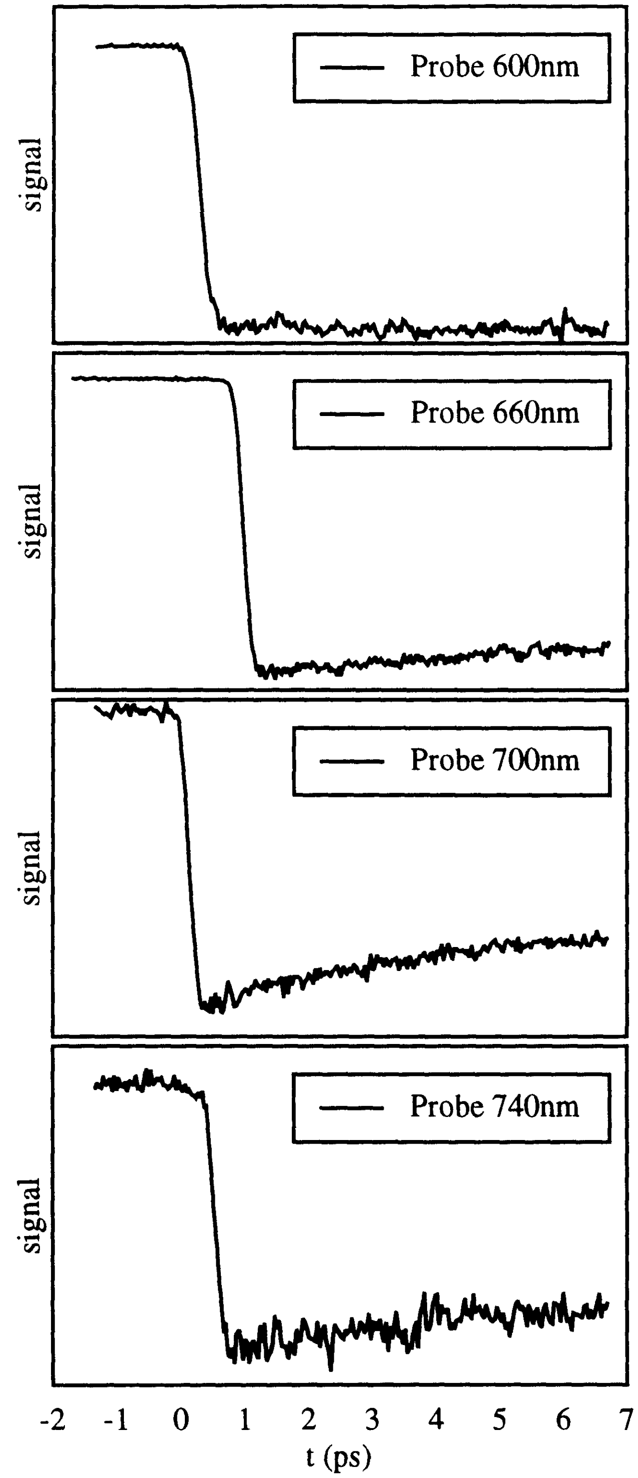

Figure 4.9 b) Transient absorption of DSP in chloroform.
Pump 405 nm.

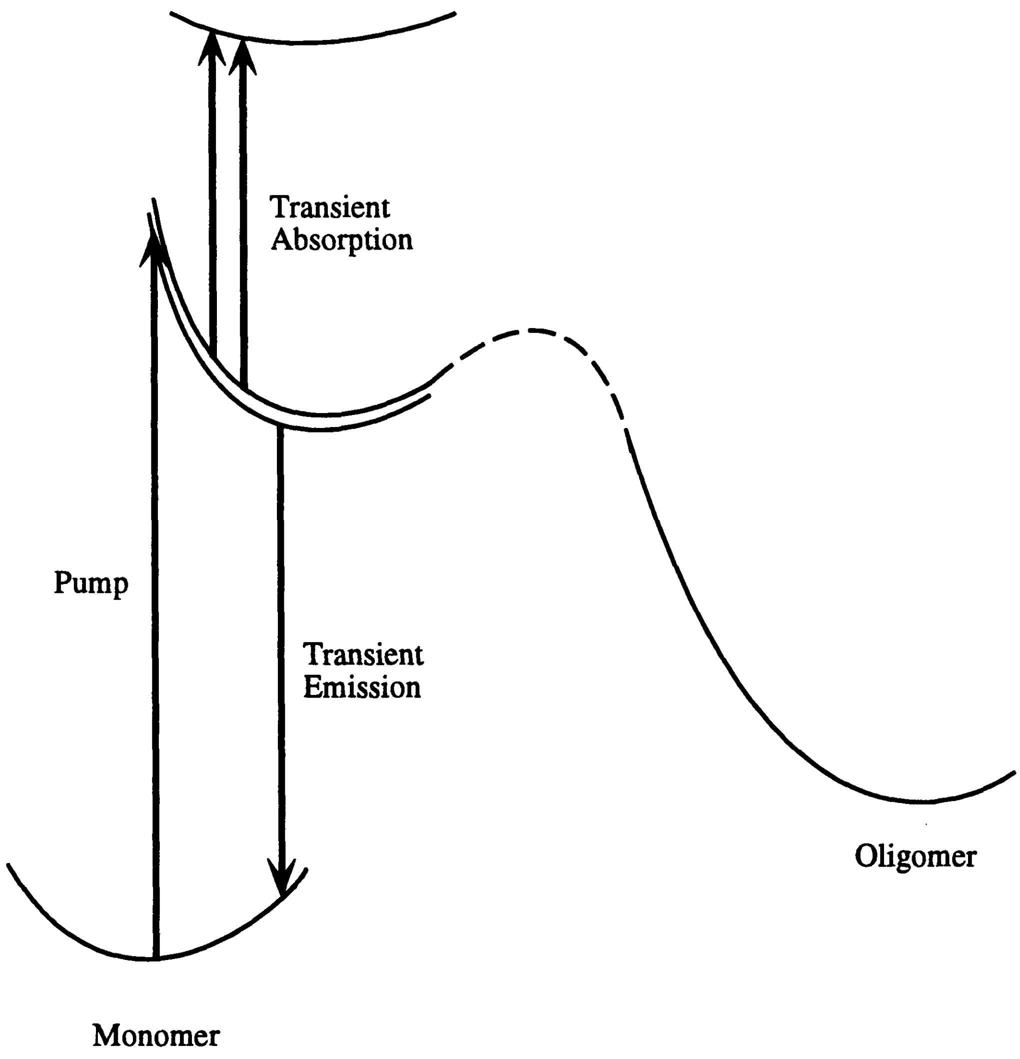

Figure 4.10 Illustration of the potential surfaces along the reaction coordinate involved in the DSP reaction.

shot experiments. Both the beam spatial profile stability and the intensity stability were much better for this wavelength than other wavelengths which were selected from the white light continuum.

Experiments with the DSP crystal were also tried with this setup. The transparent yellowish sample turned opaque within a few hundred laser shots preventing any further experiment.

4.4 PRELIMINARY FEMTOSECOND SPECTROSCOPY OF DSP REACTION DYNAMICS IN SOLID STATE

The single shot spatial encoding method was used on DSP crystal samples. The crystals were yellowish α-form flakes either home grown from solution using tetrahydrofuran as solvent or sent by the Eckhardt group of University of Nebraska at Lincoln. The quality of the crystals was critical in getting single shot signals. Only a few crystals from the Eckhardt group were good enough to be used in the experiments

Experiments were performed with 405 nm pump and 810 nm probe. A schematic of the experimental setup was presented in Fig. 3.12. The amplifier was run at 1 KHz repetition rate. A 24-slot chopper (Laser Precision) with 22 of the slots taped reduced the repetition rate of the laser pulses to about 40 Hz. Two slots at the opposite side of the chopper blade were left open to maintain balance. A mechanical shutter (Uniblitz) was put into the pump beam path. This shutter was synchronized to the CCD camera shutter in such a way that it opened when the CCD shutter opened. This prevented the pump light from reaching the sample when data collection was not in progress. The CCD shutter was in turn synchronized to the laser pulses by a pohtodiode which picked up a small portion of the pump light. The Uniblitz shutter was put at a pump beam waist to avoid clipping of the beam during opening and closing.

Single shot experiments with DSP solution were carried out first to obtain the pump spatial profile. They were used to normalize the probe signal spatial profile. Data here were averages of 25 shots. Fig. 4.11 presents the probe signal spatial profiles at several delay line settings. From Fig. 4.11 it can be seen that the probe signal spatial profile was the same at this delay line setting as at the t=-1.333ps delay line setting. This meant that the signal had reached a constant at this delay and we could use this as the pump spatial profile. Calibration of the time axis was done by measuring the relative displacement of the signals across the CCD from two delay settings (at t=-0.333ps and t=-0.667ps). At these two delay line settings, the signal started in the center portion of the pump spatial profile (see Fig. 4.11) to provide the best signal to noise ratio. The rise part of the probe signal spatial profile could be fitted very well by two approximately parallel lines (Fig. 4.12). The distance in the x-direction gave a calibration relation of 4.4fs/pixel. Fig. 4.13 presents the recovered signal after normalizing with the longer delay (delay line at -2.000ps) probe signal spatial profile. The signal was constructed from data at t=-0.333ps and t=-1.333ps. No scaling of the signal level was involved in the construction procedure. We simply translated the signal along the time axis according to its delay setting and merged them together. This also demonstrates that the method was reproducible and self consistent.

After solution phase data were taken, the crystal sample mounted between two glass slides was inserted and aligned with the pump beam blocked to avoid damage to the sample. Single or multiple shot data were collected. It has been found that a few tens of shots could be taken at the same region before the sample deterioration caused signal to noise ratio to drop. However, since every shot caused changes in the sample, retaking the background was necessary after each shot was collected. Fig. 4.14 shows the probe signal spatial profiles at several delay line settings averaged 15 shots. The signals were noisier than those from the solution. In fact, even the best crystal which looked optically very good by eye was not entirely uniform across. This reduced the signal-to-noise ratio significantly.

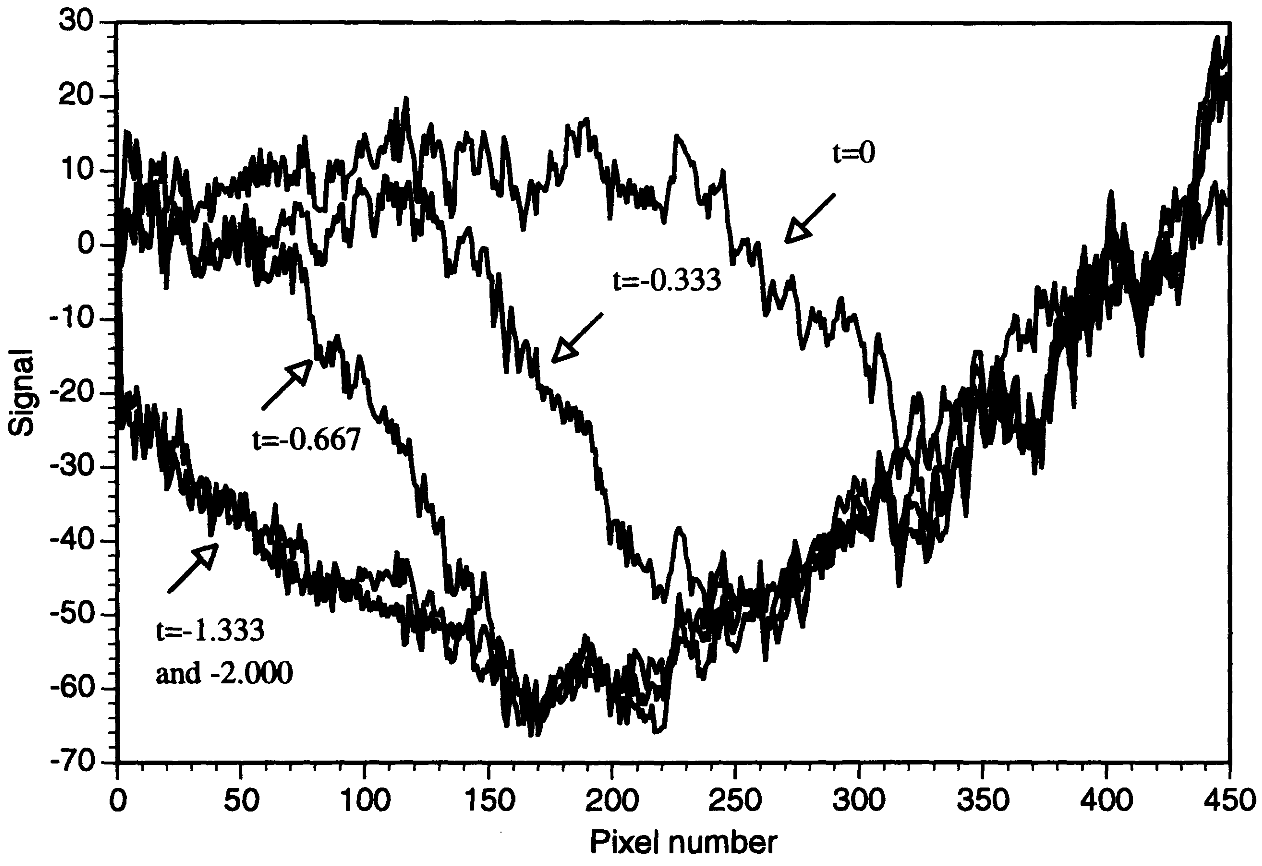

Figure 4.11 Probe signal spatial profiles at different delay settings. Delay setting unit is picosecond.

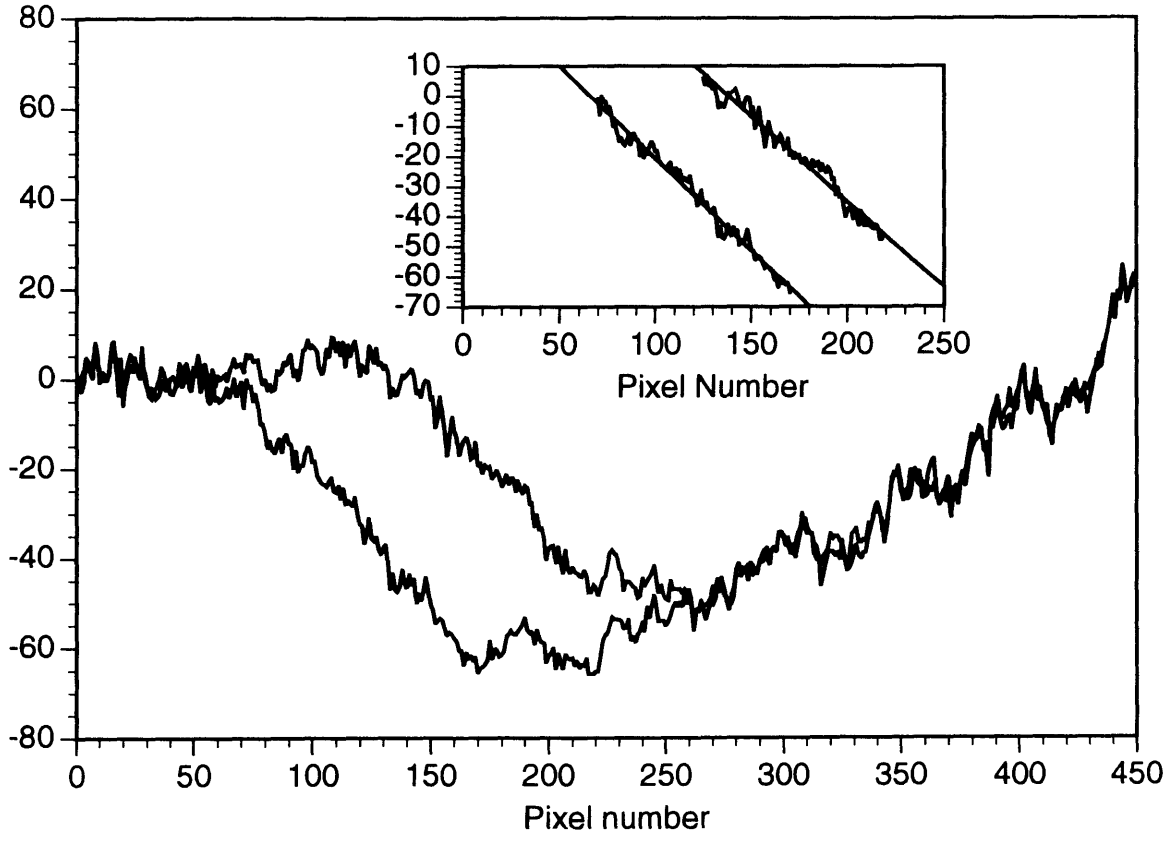

Figure 4.12 Calibration graph

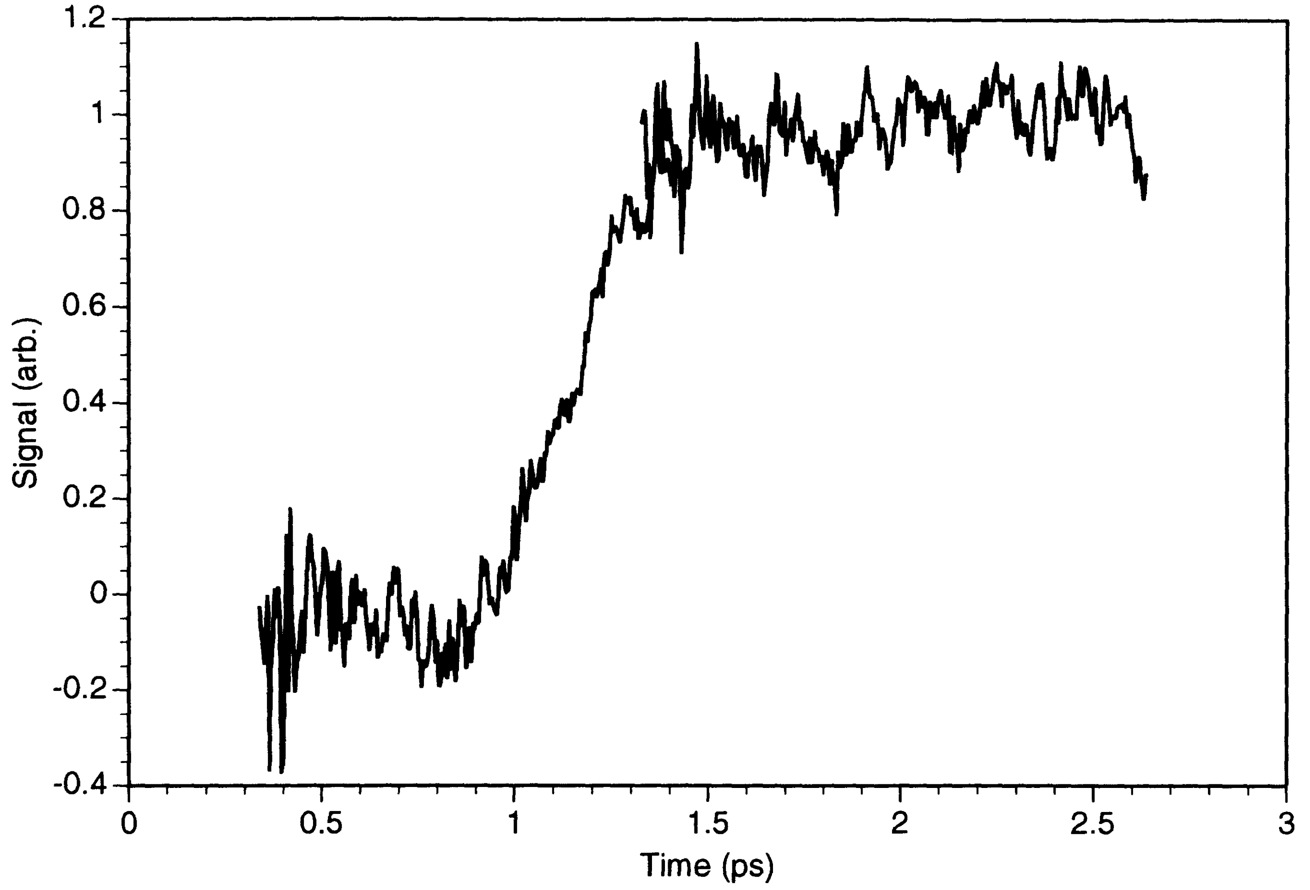

Figure 4.13 Recovered single shot signal in solution.

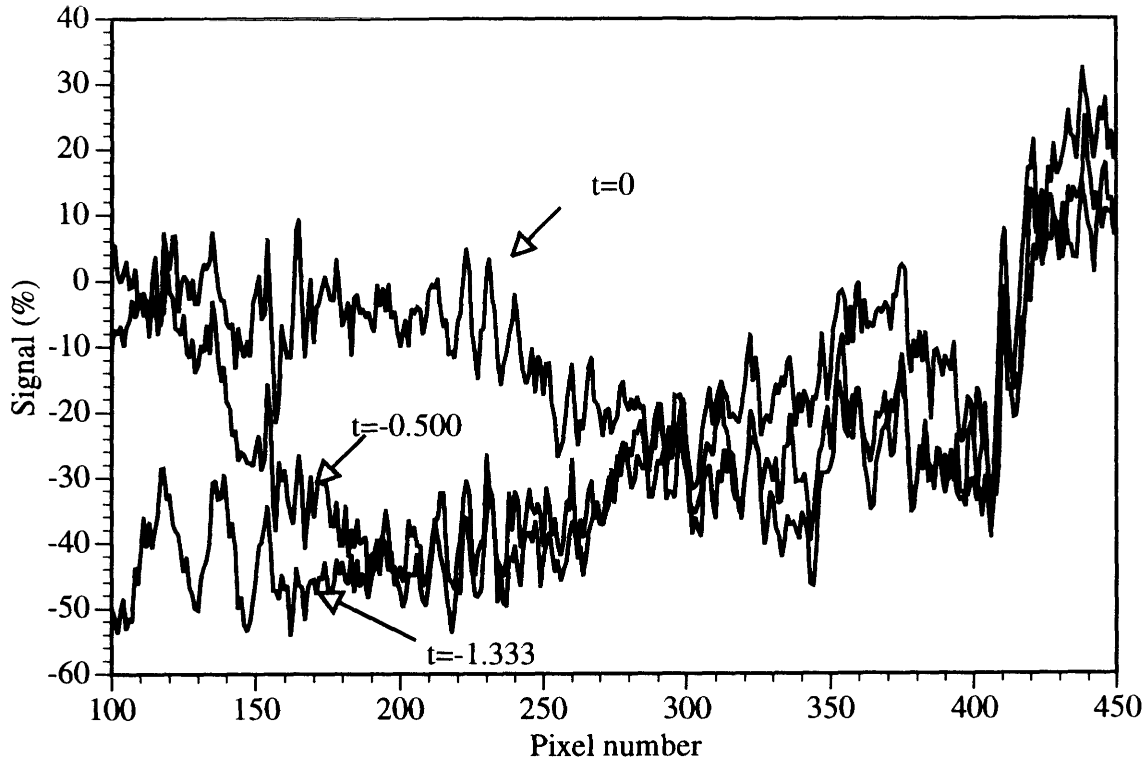

Figure 4.14 Probe signal spatial profiles of DSP crystal. Delay setting unit is picosecond.

Fig. 4.15 presents the recovered signal after normalizing with the t=-2.000ps delay probe signal spatial profile in solution. This signal was constructed from the three data sets showed in Fig. 4.13 in the same way as we generated the solution phase single shot signal.

Fig. 4.16 presents the single shot signal in a crystal along with the signal from solution. It can be seen that within a 1 picosecond window the two curves overlap very well. This may indicate that a barrier exists in the crystal phase reaction. Photoxecitation may not excite the reactants to a portion of the potential surface higher than the barrier height. Both the favorable crystal packing and the electronic transition induced local lattice deformation may not be enough to move the reactant configuration to a potential region which is higher than the barrier. It is to be noted that it is not necessary to have a diminished barrier height to allow subpicosecond reaction as in the ground state (or thermal) reactions. In a photochemical reaction, even there is a barrier on the reactive excited state potential energy surface, since photoexcitation may prepare reactants on a higher portion of the potential surface rather than the potential minimum, reaction could proceed almost as if it is barrierless. The result here is not a trivial one by revealing that the reaction may not be barrierless under our experimental conditions. However, these conclusions should be viewed as tentative.

4.5 FURTHER EXPERIMENTS

The first and foremost improvement in the single shot studies of DSP solid state reaction is to make the method quantitatively more precise. This could include improving the signal-to-noise ratio and better aligning procedure (for example automated alignment by computer as discussed in section 3). The crystal optical quality must be improved, too, in order to use the spatial encoding method. The signal should be at the same level of precision as the solution data collected with the regular pump-probe method to allow a more

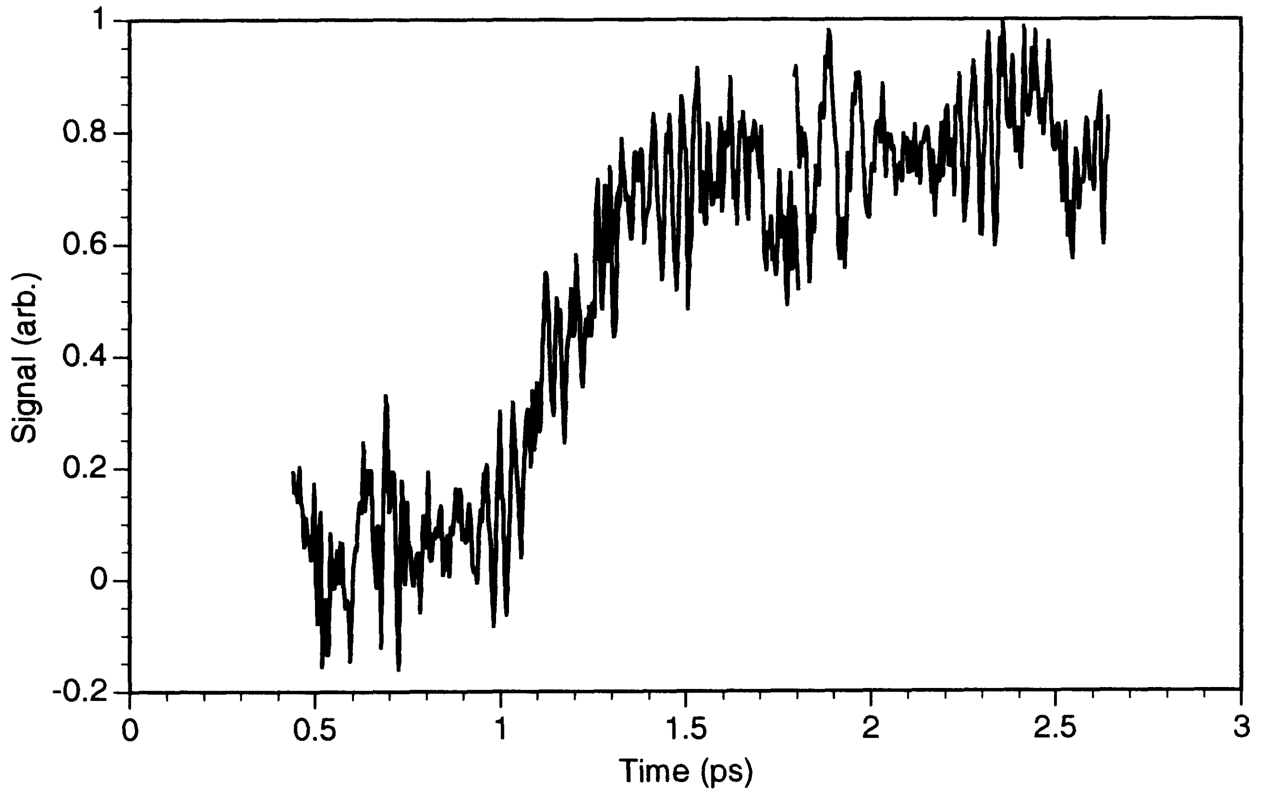

Figure 4.15 Recovered signal in DSP crystal.

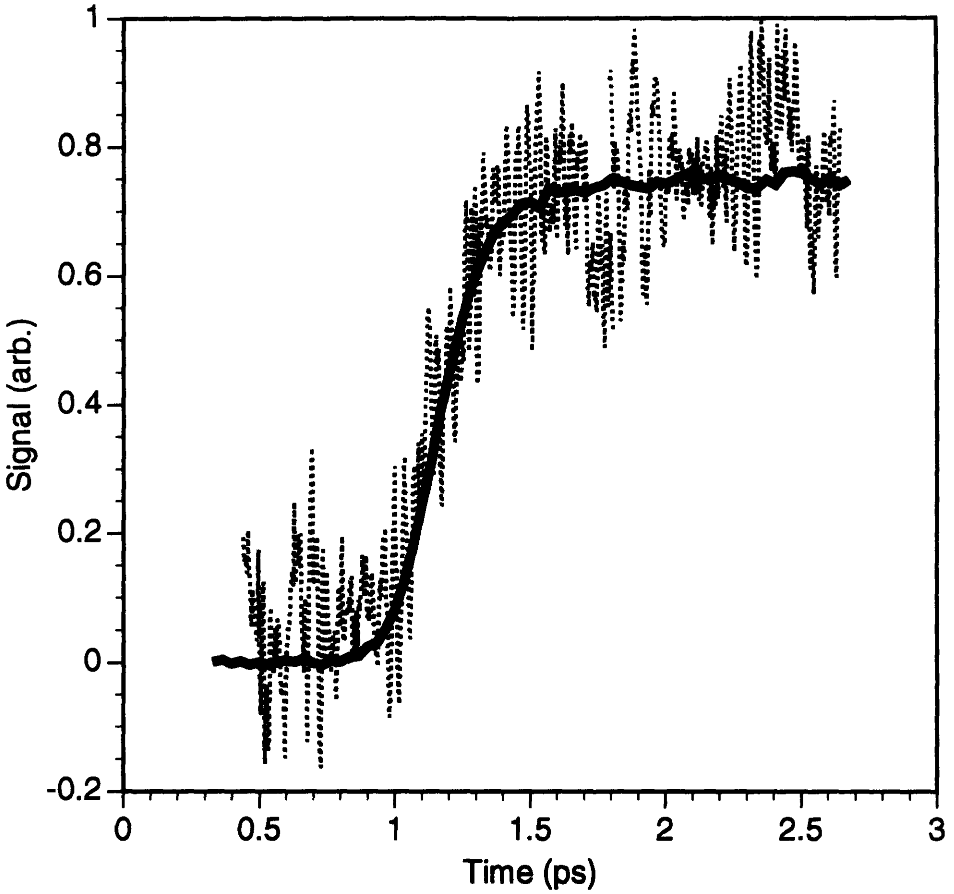

Figure 4.16 Transient absorption in DSP crystal and solution. The solid curve is the signal in solution. The solution curve is the same as in Fig. 4.9b while the crystal curve is the same as in Fig. 4.15.

precise comparison and extraction of molecular parameters. As mentioned above, if the barrier height is comparable with the energy of the photoexcitation prepared reactants, the deviation between the crystal and the liquid solution signal may be small and good quality data is necessary to allow an unambiguous determination. Since the reaction could be biexcitonic, a pump intensity dependence study would be of importance. This would require higher pulse energy from the amplifier. Currently, we have used all pump light that we could generate. The method involves spatial filtering of the pump light which cut the intensity down to about 25% and focusing the pump cylindrically to a roughly 3 mm by 50 μm strip, both of which reduced the intensity at the sample. It is also important to study the temperature dependence of the reaction because the trapping rate tends to decrease at higher temperatures while barrier crossing tends to increase at higher temperatures. A temperature dependence study will further provide us with information that could be used to examine the reaction mechanism.

5. MOLECULAR DYNAMICS SIMULATION STUDIES OF THE SOLVENT CAGE EFFECT ON PHOTODISSOCIATION IN CONDENSED PHASES

5.1 INTRODUCTION

The solvent cage effect on photodissociation has been one of the classical and, quite possibly, the simplest examples of the modification of intrinsic chemical reaction dynamics by the condensed phase environment. It was first discussed by Frank and Rabinowitch many decades ago [5.1]. Rabinowitch and Wood then suggested that in solutions reacting molecules tended to collide with each other a few times before they break out of the solvent "cage" around them [5.2]. This may be the origin of the now popular term the "cage effect". Since then this effect has been subjected to extensive theoretical and experimental studies.

There have been many spectroscopic studies of this solvent "cage effect" with modern spectroscopic methods since the 1970s [5.3-5.5]. Time-resolved studies with picosecond time resolution (more correctly 100 picoseconds) started in the mid-1970s by Eisenthal and co-workers [5.6]. These studies and the more extensive picosecond experimental work by Harris and co-workers [5.7-5.9] have laid the experimental foundation for an understanding of the dynamics of the cage effect. Theoretical studies and molecular dynamics simulations have also played crucial roles in reaching an understanding of the cage effect [5.10, 5.11]. As a matter of fact, it was the discrepancy between the earlier explanations of the experimental results and the theoretical and MD simulation results [5.6, 5.10, 5.11] on the time scale of I_2 geminate recombination that motivated a lot of efforts on both sides. This close interaction between theory and experiment has helped to reveal a general physical picture of the "cage effect".

To this day the solvent cage effect on photodissociation has also been studied with a variety of other molecules such as large organic molecules [5.12] or metal complexes [5.13] in addition to simple diatomic molecules such as pure and mixed halogens [5.3-5.5] in a variety of solvents, including solid matrices [5.3-5.5, 5.14-5.17] and clusters [5.19, 5.20] in addition to liquids. The basic features of this effect, however, can be best described with a simple diatomic molecule in a simple atomic solvent. Fig. 5.1 presents a

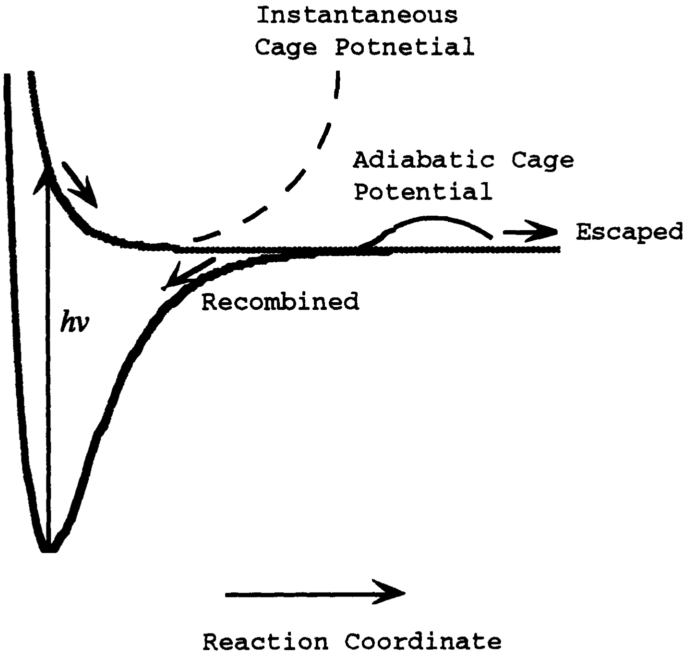

Figure 5.1 Illustration of the solvent cage effect of photodissociation.

pictorial illustration of the solvent cage effect using this simple diatomic molecule. In the gas phase, photoexcitation to a repulsive potential energy surface will lead to the separation of the two atoms. Depending on the excess energy and the details of the potential energy surface, etc., it takes an isolated molecule several tens to several hundreds of femtoseconds to dissociate [5.21-5.24]. In solutions, due to the large density of solvent atoms around the photoexcited chromophores, the separating atoms will collide with solvent atoms before they can reach large separations. We say that the solvent atoms form a cage around the chromophore. The two dissociating atoms could either break out of the cage and dissociate if they have enough kinetic energy to make their way through the cage potential barrier or be trapped in the cage after they have lost most of the energy to the solvent atoms (or its cage) through collisions. In the case of being trapped in the cage, if the repulsive potential energy surface is correlated in the asymptotic region to the ground electronic state, the two atoms will eventually cross down to the ground state and recombine. The time required for this process (geminate recombination) was determined to be on the order of picoseconds for iodine by both experiments [5.8] and MD simulations [5.10. 5.11, 5.25]. Of course, it should depend on factors such as the details of the potential energy surfaces and solvent density, etc. Recent experimental studies showed that this process could be as fast as a few hundreds of femtoseconds [5.26]. After geminate recombination, the newly formed molecule will relax from the top of its ground state potential well to the bottom via interaction with the surrounding solvent atoms (vibrational relaxation). This process could take several tens to several hundreds of picoseconds to nanoseconds, depending on the vibrational energy spacing of the solute and the guest-host coupling, etc. Based on this picture, we can divide the whole process into two major events: a) early time dynamics: the dynamics on the repulsive potential energy surface and surface hopping (curve crossing); and b) vibrational relaxation.

The earlier experimental and theoretical work focused mostly on the vibrational relaxation dynamics. With the time resolution improved into the sub-100fs regime, the early time dynamics has been the focus of more recent theoretical and experimental investigations. As mentioned above, Harris and co-workers have demonstrated recently that geminate recombination in certain systems could happen in a few hundreds of femtosecond [5.26]. Scherer and Fleming and co-workers have studied the predissocaiton of I_2 bound B-state and concluded that the predissociation of I_2 B-state induced by solvent collisions occurred within one picosecond and some coherence was preserved during this predissociation process [5.27, 5.28]. Apakarian and co-workers have studied the cage effect on I_2 when it was excited to the A-state above the dissociation limit in crystalline argon or krypton solution. They have observed coherent rebound from the solvent cage and coherent motion in the A-state potential well [5.15, 5.16]. Zewail and co-workers studied the solvent cage effect on I_2 in a variety of densities of argon fluids as well as CCl_4 liquid [5.29, 5.30]. They also studied the solvent cage effect in argon clusters and observed similar behavior to the results of Apkarian and co-workers [5.20].

The behavior of a dissociating molecule while still on its repulsive intramolecular potential energy surface, but also under the influence of the solvent cage, can also be examined. This behavior should reflect not only the interaction between the dissociating molecule and its initial solvent cage, but also solvent structural relaxation from the initial configuration around the reactant to a new configuration which will accommodate the dissociating molecule and finally the separated photofragments. There are two limiting cases of this cage dynamics. In the first limit, the solvent can follow the solute motion adiabatically. This corresponds to fast solvent motion and slow solute motion along the reaction coordinate. The dynamics is of the diffusive type and can be described by a Langevin equation. The other limit corresponds to the rigid cage limit, in which motion along the reaction (dissociation) coordinate is much faster than solvent relaxation. In this case we might expect to observe the dissociating fragments oscillating against each other [5.31-5.33]. The general situation lies somewhere between these two limits. It has been known that the adiabatic mean field potential energy barrier [5.34, 5.35] the solvent cage provides is usually not high enough to prevent the chromophore from dissociating. However, in many cases, such as Cl_2 in solid xenon matrix, the cage effect was almost complete, even with an excess energy over 1eV [5.4]. This makes it more interesting to study the possibility of solvent cage-induced oscillation on repulsive potential surfaces, since it demonstrates that the dissociating chromophores actually interact with stronger cage potentials than the adiabatic cage potentials. They may collide with their cages a few times before the cage potentials approached their adiabatic values. Then, even though the cage potentials are no longer as strong, the chromophores have lost most of their energy and can no longer break out of their cages. In the earlier experimental work, frequency-domain methods were used to determine whether cage forces can give rise to quantized vibrational levels on a repulsive potential surface [5.3]. No such quantization has been observed. Due to the transient nature of this kind of vibrations even if they exist, it is not generally possible to observe them with frequency domain techniques. Femtosecond time-resolved spectroscopy of liquids has also failed to reveal oscillations of molecules excited into repulsive potential energy surfaces [5.12, 5.13]. Results from more highly ordered media such as crystalline solids [5.14, 5.15, 5.36], ordered van der Waals clusters [5.19, 5.20], and even some proteins [5.37] are more encouraging. Experiments on I_2^- in CO_2 clusters [5.19] showed oscillatory responses in dissociative potential energy surfaces. Photoexcitation of I_2 in argon clusters [5.20] and in solid argon or krypton matrices [5.14, 5.15] gave rise to coherent oscillations in the weakly bound A state, even though the initial energy was well above the dissociation limit. On the other hand, since this dynamics would provide unique information about the solvent structure (cage potential, for example) and its relaxation in response to impulsive driving forces (memory kernel and random forces, for example), further studies are warranted.

In general, the prospects for observation of coherent oscillatory motion in an unbound molecular potential energy surface due to solvent effects in ordinary liquids are reduced by several factors. First, there is often an imbalance of forces in which the molecular exit force driving photofragment separation overwhelms the weaker intermolecular forces (cage forces) resisting it. Second, even where the cage potential is sufficiently strong there is a great deal of inhomogeneity in the local liquid-state environments around the reacting species, and so the forces resisting dissociation vary widely. Some molecules may dissociate with little resistance, while others may undergo excited-state oscillations of varying number and frequency before dissociation or relaxation to the molecular ground (or other unreactive) state. In addition to this inhomogeneous dephasing of vibrational motion, fluctuations and relaxation of the local environments will yield an additional (homogeneous) contribution. This can be considered equivalently from a frequency-domain point of view. Motion along the reaction coordinate may be described in terms of a spectrum of frequencies whose average reflects the strength of solvent resistance to such motion (as well as the repulsive molecular potential energy surface) and whose width reflects the solvent relaxation dynamics as well as the degree of inhomogeneity in the local solvent environments. For many photodissociation reactions in liquids, the width of such a spectrum may be far greater than the average frequency, i.e. many photodissociation events proceed with little or no resistance and those that do undergo oscillations have a wide range of frequencies. The experimental result is a washing out of any oscillatory structure. To the extent that oscillations between incipient photofragments on a repulsive potential energy surface can be observed, they could provide a wealth of information about the forces between reacting molecules and their environments, the degree of inhomogeneity in those forces, and the dynamics of solvent responses to solute reactivity.

5.2. THEORETICAL BACKGROUND

In order to have a more precise formulation about our problem in hand, we need to take a small exercise to describe it in a more appropriate way. We choose to use a theory developed by Adelman and co-workers [5.31-5.33], because we want to study a system where the motion of the dissociating molecules is much faster than the structural rearrangements of their solvent surroundings. This is exactly the opposite of the Langevin approach to Brownian motion. A better zeroth order approximation is thus a molecule in a completely rigid cage instead of an adiabatic cage. We will also briefly discuss the instantaneous normal mode analysis in the context of solvent cage effect in liquids. We will apply this technique to calculate the instantaneous spectrum along the reaction coordinate.

5.2.1 The Molecular-Time-Scale Generalized-Langevin-Equation (MTGLE) Theory

Employing the statistical mechanical theory of irreversible processes, the theory reduced the many-body dynamical problem of chemical reaction dynamics in condensed media into an effective few-body problem. It showed that the cage restoring force exerted on a reaction coordinate is a result of the solvent system's delay in trying to maintain equilibrium with the instantaneous solute configuration. This theory provides a good conceptual framework for us to grasp the general physical picture of the solvent cage effect..

Here we present an approximate derivation of the equations of motion of the MTGLE theory [5.33]. A formal derivation using Mori's projection operator method is given in by Adelman [5.33].

The Hamiltonian of a solution including a solute molecule with reaction coordinate $r=(\vec{r}_1,\cdots,\vec{r}_n)$ is

$$H=\sum_{\lambda=1}^{N}\frac{p_\lambda^2}{2M}+\frac{1}{2}\sum_{i=1}^{n}m_i\dot{r}_i^2+U_{VV}(q)+U_{VU}(q,r_0)+U_{UU}(r_0) \tag{5.1}$$

where M is the mass of the solvent molecules, q is the coordinate of solvent molecules $q=(\vec{q}_1,\cdots,\vec{q}_N)$, $\{m_i\}$ is the mass associated with the reaction coordinate r. $U_{VV}(q)$ is the solvent-solvent interaction potential energy, $U_{VU}(q,r_0)$ is the solvent-solute interaction potential energy, $U_{UU}(r_0)$ is the solute intramolecular potential energy.

The Hamiltonian H_0 of the solvent on condition that the solute configuration is clamped at r_0 is

$$H_0=\sum_{\lambda=1}^{N}\frac{p_\lambda^2}{2M}+U_{VV}(q)+U_{VU}(q,r_0) \tag{5.2}$$

The Liouville operator corresponding to H_0 is

$$iL_0=\sum_{\lambda=1}^{N}\left\{\frac{\vec{p}_\lambda}{M}\cdot\frac{\partial}{\partial\vec{q}_\lambda}-\frac{\partial}{\partial\vec{q}_\lambda}[U_{VV}(q)+U_{VU}(q,r_0)]\cdot\frac{\partial}{\partial\vec{p}_\lambda}\right\} \tag{5.3}$$

Assuming r moves from r_0 at t=0 to $r_0+\Delta r_0(t)$ at t=t, the Liouville operator at t becomes

$$iL(t)=\sum_{\lambda=1}^{N}\left\{\frac{\vec{p}_\lambda}{M}\cdot\frac{\partial}{\partial\vec{q}_\lambda}-\frac{\partial}{\partial\vec{q}_\lambda}[U_{VV}(q)+U_{VU}(q,r_0+\Delta r_0(t))]\cdot\frac{\partial}{\partial\vec{p}_\lambda}\right\} \tag{5.4}$$

To linear order in $\Delta r_0(t)$

$$\begin{aligned} U_{VU}[q, r_0 + \Delta r_0(t)] &= U_{VU}(q, r_0) + \sum_{i=1}^{n}\sum_{\alpha=1}^{3} \frac{\partial}{\partial r_{0i}^{\alpha}} U_{VU}(q, r_0) \cdot \Delta r_{0i}^{\alpha}(t) \\ &\equiv U_{VU}(q, r_0) - \sum_{\alpha=1}^{3} F_i^{\alpha} \Delta r_0^{\alpha}(t) \\ &= U_{VU}(q, r_0) - F^T \cdot \Delta r_0(t) \end{aligned} \tag{5.5}$$

where we have defined $F_i^{\alpha} = -\frac{\partial}{\partial r_{0i}^{\alpha}} U_{VU}(q, r_0)$. Write

$$iL(t) = iL_0 + iL^{(1)}(t) \tag{5.6}$$

where $iL^{(1)}(t) = \sum_{\lambda=1}^{N} \frac{\partial}{\partial \vec{q}_{\lambda}} [F^T \cdot \Delta r_0(t)] \cdot \frac{\partial}{\partial \vec{p}_{\lambda}}$. Linear response theory gives the solvent probability distribution function as

$$f(p,q;t) = f^{(0)}(p,q) + \int_0^t d\tau \exp[-iL_0 \cdot (t-\tau)][-iL^{(1)}(\tau) f^{(0)}(p,q)] \tag{5.7}$$

where $f^{(0)} = Z_0^{-1}(\beta) e^{-\beta H_0}$ is the solvent PDF at t=0, and $Z_0(\beta) = \int e^{-\beta H_0(p,q)} dpdq$ is the partition function. Since

$$-iL^{(1)}(t) f^{(0)}(p,q) = \beta f^{(0)}(p,q) \sum_{\lambda=1}^{N} \frac{\vec{p}_{\lambda}}{M} \cdot \frac{\partial}{\partial \vec{q}_{\lambda}} [F^T \cdot \Delta r_0(t)] \tag{5.8}$$

and the equation of motion for F^T is

$$\dot{F}_0^T = iL_0 F^T = \sum_{\lambda=1}^{N} \frac{\vec{p}_{\lambda}}{M} \cdot \frac{\partial F^T}{\partial \vec{q}_{\lambda}} \tag{5.9}$$

$$-iL^{(1)}(t) f^{(0)}(p,q) = \beta f^{(0)}(p,q) \dot{F}_0^T \cdot \Delta r_0(t) \tag{5.10}$$

we have

$$f(p,q;t) = f^{(0)}(p,q)\cdot\{1+\beta\int_0^t \dot{F}_0^T(\tau-t)\cdot\Delta r_0(\tau)d\tau\} \tag{5.11}$$

The force acting on solute is

$$\begin{aligned}\langle F\rangle_t &= \int dpdqf(p,q;t)F[q,r_0+\Delta r_0(t)] \\ &= \langle F\rangle_{r_0} + \left\langle \frac{\partial F^T}{\partial r_0} \right\rangle_{r_0} \cdot \Delta r_0(t) + \beta\int_0^t \left\langle \tilde{F}_0 \dot{\tilde{F}}_0^T(\tau-t) \right\rangle_{r_0} \cdot \Delta r_0(\tau)d\tau \end{aligned} \tag{5.12}$$

where $\tilde{F}_0(t) = F_0(t) - \langle F\rangle_{r_0}$. The total force on the solute to resist the change $\Delta r_0(t)$ is

$$\begin{aligned} F[\Delta r_0(t)] &= F_g[r_0 + \Delta r_0(t)] + \left\langle \frac{\partial F^T}{\partial r_0} \right\rangle_{r_0} \cdot \Delta r_0(t) \\ &-\beta\int_0^t \left\langle \dot{\tilde{F}}_0(t-\tau)\tilde{F}_0^T \right\rangle_{r_0} \cdot \Delta r_0(\tau)d\tau + \tilde{F}_0(t) \end{aligned} \tag{5.13}$$

where Fg(r) is the intramolecular force of the solute $F_g(r) = \frac{\partial U_{UU}(r)}{\partial r}$, and $\tilde{F}_0(t)$ is the solvent random force associated with change $\Delta r_0(t)$. The equation of motion for the reaction coordinate r is thus

$$m\ddot{r}(t) = F_g[r(t)] + \left\langle \frac{\partial F^T}{\partial r} \right\rangle_{r_0} \cdot r(t) - \beta\int_0^t d\tau \left\langle \dot{\tilde{F}}_0(t-\tau)\tilde{F}_0^T \right\rangle_{r_0} \cdot r(\tau) + \tilde{F}_0(t) \tag{5.14}$$

This is a very suggestive equation of motion. The center two terms have physical interpretations as follows: $\left\langle \frac{\partial F^T}{\partial r} \right\rangle_{r_0} \cdot r(t)$ is the cage restoring force which gives rise to the dynamic cage effect. This is the most important outcome of the MTGLE theory. The integral term accounts for the solvent nonrigidty and energy dissipation.

We can define (assume a single coordinate for simplicity)

$$\omega_{e0}^2 = -\frac{1}{m}\left\langle \frac{\partial F^T}{\partial r} \right\rangle_{r_0} \tag{5.15}$$

which is called the Einstein frequency. At short times or in a completely rigid cage, both the integral term and $\tilde{F}(t)$ in Eq.(5.14) are negligible. The motion will be an oscillator type governed by potential $U_{UU}(r)$ and $-\frac{1}{2}\omega_{e0}^2 r^2(t)$. Fig. 5.2 plots such a "rigid" cage potential for the model I_2 solution. The repulsive part was taken as $U_{UU}(r) = ar^{-9}$, $a = 7.54 \times 10^7 (\text{KÅ}^9)$ and $\omega_{e0}^2 = 28 ps^{-2}$ [5.38]. Fig.5.3 shows the quasibound motion on this potential.

If we define $\theta_1(t) = -\frac{\beta}{m\omega_{c1}^4}\left\langle \dot{\tilde{F}}_0(t)\tilde{F}_0^T \right\rangle$ which can be regarded as the solvent or heatbath response, we have

$$\ddot{r}(t) = m^{-1}F_g[r(t)] - \omega_{e0}^2 r(t) + \omega_{c1}^4 \int_0^t d\tau \theta_1(t-\tau) r(\tau) + m^{-1}\tilde{F}_0(t) \tag{5.16}$$

To see the physical picture involved in MTGLE, it is best to recast the equation of motion into a hierarchy of equations describing the dynamics of an equivalent nearest-neighbor chain.

Define the spectral density of $\dot{\theta}_1(t)$

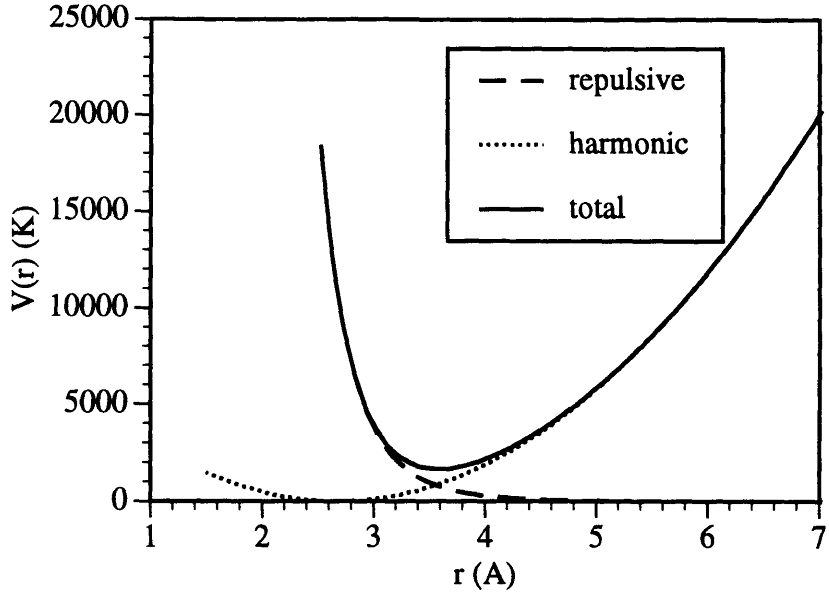

Figure 5.2 Model potential for I_2 in a rigid cage.

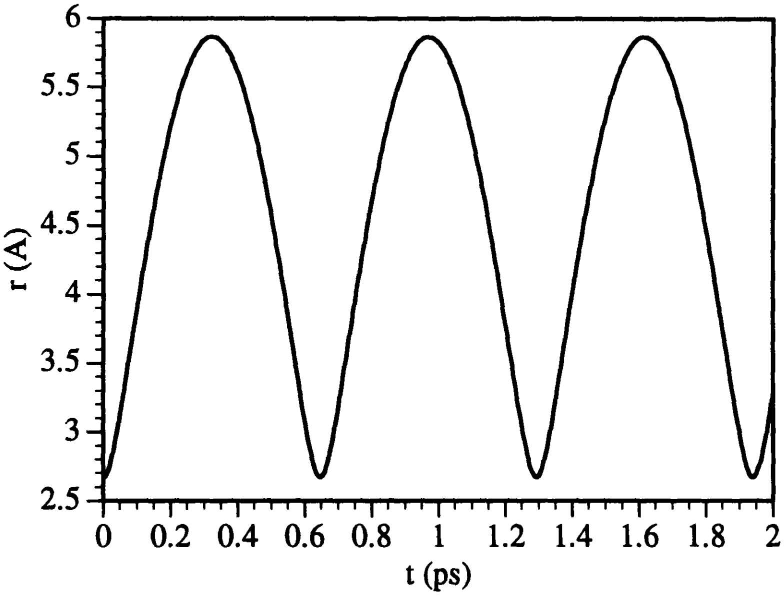

Figure 5.3 The motion of I_2 on the total potential surface shown in Fig. 5.2.

$$\sigma_1(\omega) = \frac{2}{\pi}\int_0^\infty \cos \omega t \dot{\theta}_1(t) dt \tag{5.17}$$

The Einstein frequency of the 1st heatbath and the coupling constant between the 1st and 2nd heatbath are defined as

$$\omega_{e1}^2 = \int_0^\infty \omega^2 \sigma_1(\omega) d\omega \tag{5.18}$$

$$\omega_{c2}^2 = \int_0^\infty \left(\omega^2 - \omega_{e1}^2\right)^2 \sigma_1(\omega) d\omega \tag{5.19}$$

Then we can define the response of the 2nd heatbath to the first heatbath as $\hat{\theta}_2(z) \equiv \mathcal{L}[\theta_2(t)]$ in Laplace domain

$$\hat{\theta}_1(z) = \left[z^2 + \omega_{e1}^2 - \omega_{c2}^4 \hat{\theta}_2(z)\right]^{-1} \tag{5.20}$$

In time domain, this is

$$\ddot{\theta}_1(t) = -\omega_{e1}^2 \theta_1(t) + \omega_{c2}^4 \int_0^t \theta_1(t-\tau)\theta_2(\tau) d\tau \tag{5.21}$$

Next we can define $\tilde{R}_1(t)$ as the dynamical variable associated with $\tilde{F}_0(t)$

$$\tilde{F}_0(t) = m\omega_{c1}^2 \tilde{R}_1(t) \tag{5.22}$$

and a fictitious heatbath coordinate

$$R_1(t) = \tilde{R}_1(t) + \omega_{c1}^2 \int_0^t d\tau \theta_1(t-\tau) r(\tau) \tag{5.23}$$

With the definition of $\theta_1(t)$, $\tilde{R}_1(t)$,and $R_1(t)$, and the equation of motion for $\theta_1(t)$ we have the equation of motion for $\tilde{R}_1(t)$

$$\ddot{\tilde{R}}_1(t) = -\omega_{e1}^2 \tilde{R}_1(t) + \omega_{c2}^4 \int_0^t d\tau \theta_2(t-\tau) \tilde{R}_1(\tau) + \omega_{c2}^2 \tilde{R}_2(t) \tag{5.24}$$

and hence,

$$\ddot{R}_1(t) = -\omega_{e1}^2 R_1(t) + \omega_{c1}^2 r(t) + \omega_{c2}^4 \int_0^t d\tau \theta_2(t-\tau) R_1(\tau) + \omega_{c2}^2 \tilde{R}_2(t) \tag{5.25}$$

where $\tilde{R}_2(t)$ and $R_2(t)$ are the counterparts for the 2nd heatbath as $\tilde{R}_1(t)$, and $R_1(t)$ for the 1st heatbath.

Continuously carrying out this procedure, we can construct the complete hierarchy:

$$\ddot{r}(t) = m^{-1} F_g[r(t)] - \omega_{e0}^2 r(t) + \omega_{c1}^2 R_1(t)$$

$$\ddot{R}_1(t) = -\omega_{e1}^2 R_1(t) + \omega_{c1}^2 r(t) + \omega_{c2}^2 R_2(t) \tag{5.26}$$

......

This gives us the solvent shell interpretation of the MTGLE theory (see Fig. 5.4).

It is of interest to compare the MTGLE and the conventional generalized Langevin equation. The conventional generalized Langevin equation has been used extensively in modeling chemical reaction dynamics in condensed phases. To see the connection between the MTGLE and GLE, we can integrate the integral term in Eq. (5.16) by parts and yield

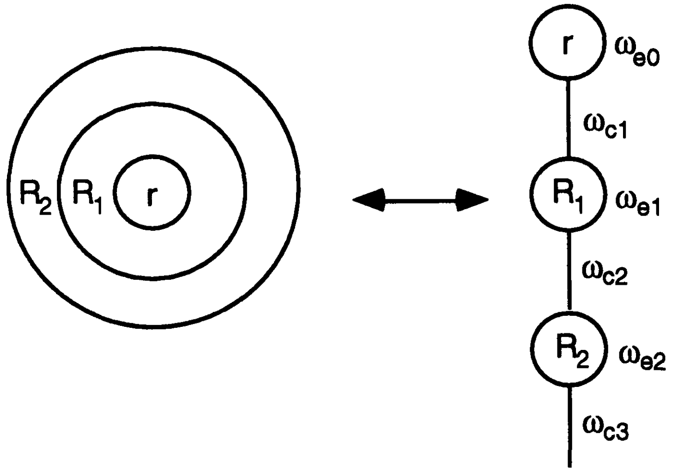

Figure 5.4 Illustration of the solvent shell interpretation of the cage effect.

$$\ddot{r}(t) = m^{-1}F_g[r(t)] - \Omega_0^2 r(t) - \int_0^t d\tau \beta_1(t-\tau)\cdot \dot{r}(\tau) + m^{-1}\tilde{\tilde{F}}_0(t) \qquad (5.27)$$

where

$$\beta_1(t) = \omega_{c1}^4 \int_t^\infty \theta_1(\tau) d\tau \qquad (5.28)$$

is the friction kernel,

$$\Omega_0^2 = \omega_{e0}^2 - \beta_1(0) \qquad (5.29)$$

is the adiabatic frequency, and

$$\tilde{\tilde{F}}_0(t) = \tilde{F}_0(t) - \beta_1(t)\cdot r(0) \qquad (5.30)$$

is the Mori form of random force.

It can be seen that the Mori's random force actually contains a systematic transient term $\beta_1(t)\cdot r(0)$. It is truly random only when $t\to\infty$, since $\lim_{t\to\infty}\beta(t)=0$. Also note that Ω_0^2 should be regarded as the adiabatic frequency, because $\beta_1(0)$ is the heatbath response to an infinitely slow process.

The two forms of the generalized Langevin equation, though mathematically equivalent, are different ways to decompose the solvent forces on the primary system. The MTGLE emphasizes the short time scales which are obviously more relevant to chemical reaction dynamics, while the conventional GLE emphasizes the adiabatic limit.

5.2.2 Instantaneous Normal Modes In Liquids

In this subsection we discuss the concept of instantaneous normal modes in a liquid and its application to the solvent cage effect. The instantaneous normal mode analysis in liquids has been revived recently to describe the short time dynamical properties of liquids [5.39-5.45]. These studies put emphasis on the connections of the instantaneous normal modes, or to be more precise, the configuration averaged stationary density of states spectrum of a liquid at equilibrium to its dynamics. However, the general concept of some kind of normal modes in a liquid as an analogy to phonons in a crystal could be dated back to the 1960s [5.46]. The approach could also be viewed as a change of representation, i.e., instead of using the ordinary three dimensional coordinate space to describe the structure and dynamics of a liquid consisting of N particles, a 3N-dimensional configuration space is used [5.47-5.49]. Since a liquid is usually not at mechanical equilibrium, this 3N-dimensional configuration space is not fixed in time but evolving, i.e., it is instantaneous. The instantaneous normal mode formalism, therefore, allows us to view the liquid from a different perspective. In a liquid at equilibrium, because the system state is stationary, the spectrum is time-independent. In a system not at equilibrium, on the other hand, we will have a configuration averaged density of states spectrum which is evolving in time.

Obviously, this 3N-dimensional representation would be more suitable to describe the collective motions in a liquid. It is particularly appealing to the study of the solvent cage effect on molecules on their repulsive intramolecular potential. The motion involved in this solvent cage effect is a local yet collective motion with all solvent molecules in the vicinity of the solute participating in it. The solvent molecules some distance away may also play a role through interactions with those close to the solute by, for example, blocking their relaxation path. In the instantaneous normal mode representation which supplies a set of eigenvectors as well as eignevalues, it will be possible to factor the cage effect part out without resorting to any mechanical, and often subjective, definition of solvent cages in real space [5.50, 5.51]. Secondly, the impulsively driven system is highly nonequilibrated. The instantaneous normal mode analysis would allow us to follow the evolution of the spectrum of the system.

The calculations of the instantaneous normal mode are actually quite straight forward. For convenience, we will write the potential energy of the solution as V(**R**) where $\mathbf{R} = (\mathbf{r}_1, \mathbf{r}_2, \dots, \mathbf{r}_N)$ represents a particular liquid solution configuration with **r**'s being the coordinates of individual solvent and solute particles in the liquid without explicit separation of the solvent and solute parts. The elements of the dynamical matrix D (also called the Hessian matrix) which are the second derivatives of this potential energy appropriately mass weighted are given by

$$D_{iA,jB}(\mathbf{R}) = (m_i m_j)^{-1/2} \frac{\partial^2 V}{\partial r_{iA} \partial r_{jB}}; i,j = 1,2,\dots,N; A,B = x,y,z \tag{5.31}$$

where m_i and m_j are the masses of the ith and jth atom. Diagonalizing this matrix will generate a set of modes $\{\mathbf{e}_\alpha\}$ which form a complete basis set for the 3N-dimensional configuration space at an instant t. The approximation is that the potential energy can be expanded and truncated at second order:

$$\Delta\mathbf{V}(\mathbf{R}) = -\mathbf{F}(\mathbf{R})\cdot\Delta\mathbf{R} + \frac{1}{2}\Delta\mathbf{R}\cdot D_{iA,jB}(\mathbf{R})\cdot\Delta\mathbf{R}+\ldots \tag{5.32}$$

where $\Delta\mathbf{R}$ is the displacement in the coordinate space and $\mathbf{F}(\mathbf{R})$ is the force whose elements are given by,

$$\mathbf{F}_{iA}(\mathbf{R}) = -\frac{\partial V}{\partial r_{iA}}; i = 1,2,\ldots,N; A = x,y,z \tag{5.33}$$

Although in a liquid, unlike in a crystal, the potential is not at a global minimum where $\mathbf{F}(\mathbf{R}) = 0$, a truncation of the potential to second order will allow a transformation of the representation from the coordinate space to the configuration space since the linear term in $-\mathbf{F}(\mathbf{R})\cdot\Delta\mathbf{R}$ will not affect a linear transformation.

Once in the 3N-dimensional configuration space with basis set $\{\mathbf{e}_\alpha\}$, we can equivalently study any structural and dynamical properties of the system. Since our interest here is to calculate the instantaneous spectrum along the reaction coordinate $\mathbf{r}$, we will project the eigenvectors to the reaction coordinate.

Assume that the Cartesian coordinates of the two solute atoms are $\mathbf{r}_1 = (x_1, y_1, z_1)$ and $\mathbf{r}_2 = (x_2, y_2, z_2)$. The vector along the bond direction is $\mathbf{r} = (x_1 - x_2, y_1 - y_2, z_1 - z_2)$. The displacements in these coordinates can be expanded in $\{\mathbf{e}_\alpha\}$,

$$\Delta x_1 = \sum_\alpha U_{\alpha,1x} \cdot e_\alpha,$$

$$\Delta x_2 = \sum_\alpha U_{\alpha,2x} \cdot e_\alpha, \qquad (5.34)$$

$$\cdots\cdot$$

where $U_{\alpha,iA}$, etc., are the elements of the transformation matrix **U**. Or written in $\Delta\mathbf{r}$,

$$\Delta\mathbf{r} = (\sum_\alpha (U_{\alpha,1x} - U_{\alpha,2x}) \cdot e_\alpha, \sum_\beta (U_{\beta,1y} - U_{\beta,2y}) \cdot e_\beta, \sum_\gamma (U_{\gamma,1z} - U_{\gamma,2z}) \cdot e_\gamma)$$

$$(5.35)$$

and the vector in internal coordinate is,

$$\begin{aligned} \Delta r &= \Delta\mathbf{r} \cdot \frac{\mathbf{r}}{r} \\ &= \frac{1}{r} \sum_\alpha [(U_{\alpha,1x} - U_{\alpha,2x}) \cdot (x_1 - x_2) + (U_{\alpha,2y} - U_{\alpha,2y}) \cdot (y_1 - y_2) \\ &+ (U_{\alpha,2z} - U_{\alpha,2z}) \cdot (z_1 - z_2)] \cdot e_\alpha \end{aligned}$$

$$(5.36)$$

Define projection operator,

$$\begin{aligned} P_\alpha^r = \frac{1}{r^2} [(U_{\alpha,1x} - U_{\alpha,2x})(x_1 - x_2) + (U_{\alpha,1y} - U_{\alpha,2y})(y_1 - y_2) \\ + (U_{\alpha,1z} - U_{\alpha,2z})(z_1 - z_2)]^2 \end{aligned} \qquad (5.37)$$

which will project out the stretching mode along the reaction coordinate from the αth normal mode. The density of states at a particular time t will be calculated after projecting out this stretching mode from all normal modes and averaged over the whole ensemble of configurations,

$$D^r(\omega;t) = \left\langle \frac{1}{3N} \sum_{\alpha=1}^{3N} \delta(\omega - \omega_\alpha) P_\alpha^r \right\rangle \tag{5.38}$$

Rigorously, this quantity will tell us the value and distribution of the potential curvature along the reaction coordinate. If this effective cage potential is harmonic, we should expect a Gaussian distribution around some center value. In other cases, the spectrum may assume more complicated shape. As mentioned earlier, this quantity may offer us a global view of the dynamics of the cage effect with both the solute and the solvent parts in it. Since the cage wall was supplied by the solvent but a mechanical definition of the cages is not achievable without arbitrariness in real space [5.50, 5.51], this global picture in the configuration space is welcomed to offer more insight into the dynamics of the cage effect.

5.3 MOLECULAR DYNAMICS SIMULATION: MODEL AND METHOD

Recent developments in computer technology have make it possible to simulate many important physical and chemical processes. In contrast to the MTGLE theoretical approach discussed above, which use statistical mechanics to reduce the many-body problem into an effective few-body problem and then solve the dynamics of this problem, molecular dynamics simulation solves the detailed many-body dynamical problem directly by following the motion of all particles in each system in the ensemble. The MD approach provides a direct connection between dynamics and material parameters, which is difficult to achieve with the theoretical approach due to the difficulty in getting closed form expressions for functions such as the heat bath response function or the friction kernel in terms of material parameters.

In an effort to have a better understanding of the solvent cage effect at the very early stage of photodissociation, we have performed classical molecular dynamics simulations on model systems of a diatomic molecule (modeled after I_2) in xenon solutions. Molecular dynamics simulation studies of I_2 in solution has been carried out by many groups [5.11, 5.25, 5.52-5.55]. We have chosen this simple system in our study not because we want to address new aspects of this particular molecule or solvent, but only because the relevant parameters are few and well characterized. Our objective is to gain physical insight into what conditions (constructed from realistic material parameters) might permit direct observation of "collisions" between incipient photofragments and amorphous solvent surroundings, as evidenced by oscillations in the trajectories of dissociating reactants while they are on unstable potential energy surfaces. In an effort to simplify the problem, we have also neglected electronic curve crossing on the short time scale of present interest. This is reasonable since in cases in which the solvent cage is sufficiently stiff that excited-state oscillations are induced, it is likely that the incipient photofragments are turned back toward each other before they reach the asymptotic region where electronic potential curves are close enough to facilitate curve crossing.

Similarly, our use of a Lennard-Jones fluid environment is based on convenience. This environment may not be optimal for observation of solvent-induced recurrence in unstable species since the attractions among solvent atoms are weak and hence the rigidity of cage structures is low. However, this study opens the door to examination of trends as the magnitudes of solvent forces are varied.

The model system used in this study consists of one diatomic molecule embedded in a solution of 254 xenon atoms in a cubic box. Periodic boundary conditions are used for solvent-solvent and solvent-solute interactions. For the highest density, the box size is about $25\mathring{A}$ which is sufficient to accommodate the largest separation between the two atoms in the diatoms in our simulations. The xenon-xenon and iodine-xenon interactions are described by Lennard-Jones potentials and calculated out to a cutoff of $2.5\,\sigma_{Xe}$. The iodine ground state potential is a Morse potential fit to the RKR potential of LeRoy [5.56]. Since in the present work the ground-state potential is only used to generate the equilibrium configurations, we tried only to fit the bottom part of the well, no efforts were made to fit the entire potential curve. The excited state potential for I_2 used was that of the repulsive $^1\Pi_u$ state of form $c(r/\alpha)^{-9.5}$ [5.25]. Table 5.1 lists the relevant xenon-xenon, iodine-xenon, and iodine-iodine potential parameters used in this work. They are plotted in Fig. 5.5.

TABLE 5.1. Potential parameters

Xe-Xe	$4\varepsilon[(\sigma/r)^{12}-(\sigma/r)^{6}]$ $\sigma=4.055\mathring{A}$ $\varepsilon=229K$
I-Xe	$4\varepsilon[(\sigma/r)^{12}-(\sigma/r)^{6}]$ $\sigma=3.94\mathring{A}$ $\varepsilon=328.6K$
I-I (ground state)	$D\{\exp[-2\beta(r-r_e)]-2\exp[-\beta(r-r_e)]\}$ $D=18044.61(K)$ $\beta=1.867(\mathring{A}^{-1})$ $r_e=2.668(\mathring{A})$
I-I (excited state)	$c(r/\alpha)^{-9.5}, c=5.755\times10^{7}(K),$ $\alpha=1\mathring{A}$

To evaluate the effect of disordered environment on cage oscillations we need to average a large number of trajectories. Our ensemble for each density and temperature consists of either 1,024 or 4,096 trajectories. No significant ensemble size effects were detected for the two sizes. Newton's equations of motion for each trajectory were

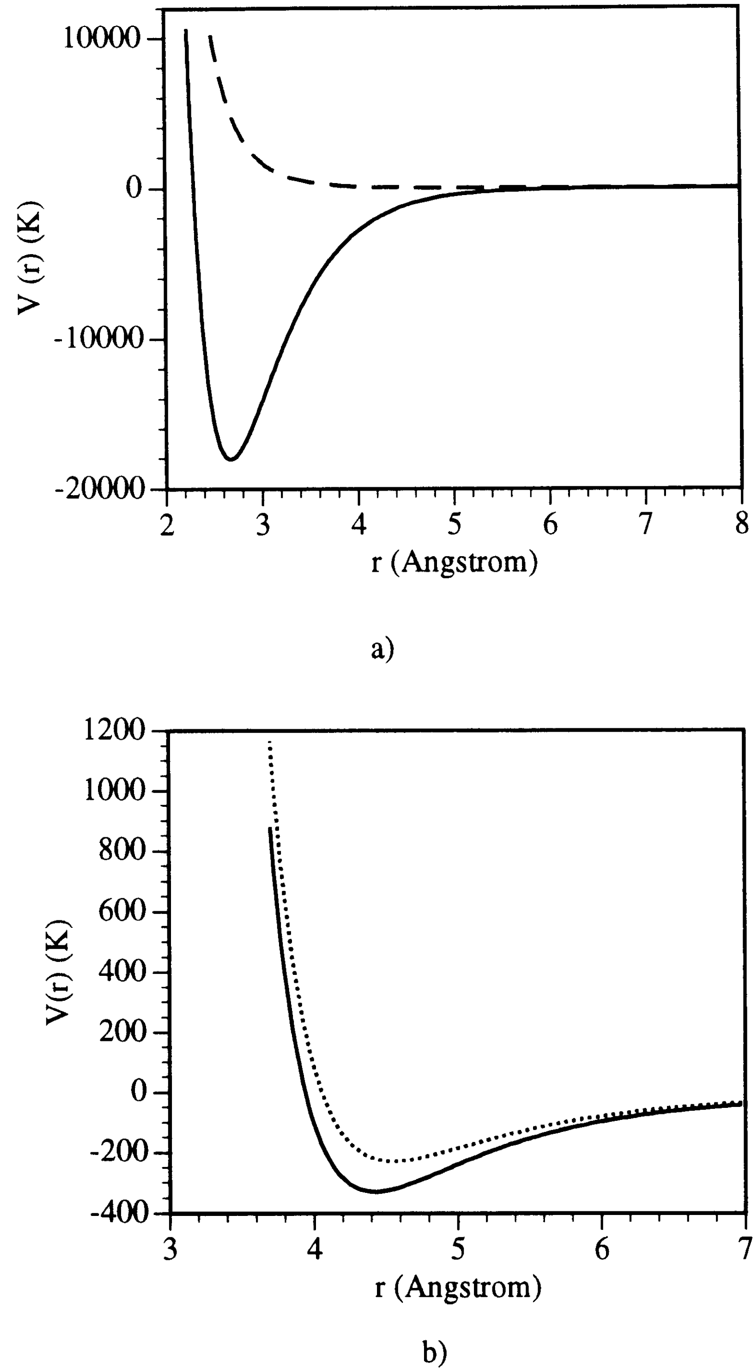

a)

b)

Figure 5.5 a) Iodine intramolecular potential curves; b) I-Xe and Xe-Xe potentials. Solid line: I-Xe, Dotted line: Xe-Xe.

propagated with a 1-fs step size for the solutions and a 5-fs step size for pure solvents using the velocity Verlet algorithm [5.57]. Two methods were used to generate the solvent configurations. In the conventional serial method, we start from a FCC lattice of 256 xenon atoms at a specified density and at 1000K. After 1000 steps with temperature scaling, we integrated the system for 5 to 6 ps before we started to save configurations of the system at 5-ps intervals. A total of 1,024 configurations at each specified density were saved. The radial distribution functions were examined to confirm that the liquid state was reached for each density. We also prepared the solvent configurations in parallel by starting from a set of either 1,024 or 4,096 identical FCC lattices with random initial velocities at 1000K and running the simulation for a total of 6 to 7 picoseconds for the whole ensemble. No differences between the results of the two methods have been detected. The crystal solvent was generated without the melting step; instead the initial FCC lattice was heated to about 100K and equilibrated at 100K for a few picoseconds. Next, we used the set of pure solvent configurations to generate the initial solution configurations. Two adjacent xenon atoms were removed from the center of the simulation box in each solvent configuration, and an I_2 molecule was inserted in their place. The iodine center of mass and orientation matched those of the two removed xenon atoms. The system was then allowed to run at 1000K (or 100K for the crystal) for 5 to 6 ps, with velocity scaling for the first picosecond. The final temperature was reached by quenching the system from 1000K (or 100K for the crystal) down to the chosen temperature and letting the system equilibrate for 8 to 10 ps. At this point, the simulation of photodissociation began. Photoexcitation was simulated by switching the solute diatom potential from the ground to the excited electronic state for all trajectories with the positions and velocities of all particles unchanged. This process corresponds to a δ-pulse (with infinitely broad spectral width) excitation. In a real femtosecond experiment, finite pulse duration (thus finite spectral width) would lead to only a fraction of the ground state trajectories (those within the Frank-Condon region covered by the pulse spectrum) to be excited to the exited state [5.27, 5.28, 5.58]. However, from the point of view of observing oscillations in disordered environments, our approach provides a lower limiting case. The finite pulse bandwidth will excite a narrower distribution and therefore will enhance the chance of observing cage induced oscillations. The evolution of the system was then monitored for 2 to 3 picoseconds and relevant quantities were calculated and saved for analysis.

The serial pure solvent runs were performed on SGI workstations (Indigo), while the parallel solvent runs and all runs with I_2 were carried out on the Thinking Machines Corp. CM5 at Boston University. Parallel MD was implemented in such a way that each trajectory in the ensemble propagated in its own data stream just as on a conventional computer while all the trajectories in the ensemble were propagated in parallel. Since our problem is intrinsically parallel, linear speedup can be achieved. The CM5 we used was a 64-node distributed memory parallel machine configured as one 32-node and two 16-node partitions. Each processing node includes one SPARC microprocessor, with 32 Mbytes of memory divided into 4 banks each of which is attached to a vector unit. Each vector unit was optimally suited for a vector instruction of length 8, and so with the 32-node partition a minimum of 1,024 trajectories were run simultaneously in order to take full advantage of the computer. However, this arrangement allocates only less 1 Mbytes of memory (1 Mbytes minus local instruction needs) for each trajectory, the traditional Verlet neighbor list can not be implemented. This may reduced the speed of the MD run somewhat. The CM5 also offers parallel input and output method which improved the overall speed a lot. With our 4,096 trajectory ensemble the restart file was about 90 Mbytes. By appropriate programming, this and other large files could be written and read in parallel greatly improved the performance. With our system of 256 (254 solvent atoms and 2 solute atoms) particles and 1,024 trajectories, about 15 hours of running time for a complete simulation of one density and temperature were required on the 32-node partition. About 50 hours were needed for ensembles with 4,096 trajectories. On a 16-node partition roughly twice as long processing times were needed.

The instantaneous normal mode densities at a specific time t' were calculated as follows. The ensemble of trajectories was propagated to t' and the instantaneous configuration for each trajectory was saved. The Hessian matrix for each configuration was constructed and diagonalized to obtain eigenvalues and eigenvectors for the configuration. The spectral density of the system at time t' was then calculated through binning the eigenvalues of all trajectories in the ensemble. The spectral density of the stretching mode was calculated through projecting out this mode from the complete set of eigenstates.

The implementation of this calculation on CM5 was more demanding. With 256 particles for each trajectory, the Hessian matrix was 768 by 768. Using double precision in the calculation, each Hessian matrix requires about 5 Mbytes of memory. As we have discussed above, for an ensemble of 4,096 trajectories, only less than 1/4 Mbytes of memory was available for each trajectory. We could not perform the instantaneous normal mode calculation on the fly. We had to propagate the trajectories and dump configurations to disk and then run the instantaneous normal mode calculation in a separate job. Even with this arrangement, it is still impossible to perform the calculation over the whole ensemble simultaneously as we did with the MD runs. We performed the instantaneous normal mode calculation on one configuration at a time but spread the single configuration calculation across the whole partition. The CPU time for each configuration was about 10 seconds for the high density solutions and about 100 seconds for the $\rho^*=0.7$ solution. The speed difference was due to one CM5 black-box routine which performs diagonalization. It is possible that this routine is less efficient in dealing with more sparse matrices. In any case the speed was acceptable such that averaging over at least part of the ensemble was possible. As a comparison, the CPU time for the same task, i.e., diagonalizing the Hessian matrix for a 256 particle system, was about 40 minutes on an SGI Indigo. We averaged

1000 configurations at each time t' for the $\rho^*=1.1$ at low temperatures with the iodine and the light iodine solutions. Other systems were averaged over only 100 configurations at each time t'. The time interval at which we performed the instantaneous normal mode calculation depended on solvent states. In any case, intervals no less than 100 femtoseconds were used. It would be better to average more configurations at each time t' and use shorter time intervals. However, that would have increased the computational load significantly.

5.4. MOLECULAR DYNAMICS SIMULATION: RESULTS

Part of the results presented here have been reported [5.59, 5.60].

5.4.1 Solvent Structures

Several solvent reduced densities were used. Here we report results from a liquid solution with reduced density (defined as $\rho^*=\rho\sigma^3$, where ρ is the number density and σ is the Lennard-Jones radius) of 0.7 at temperature 250K. We also report results at a solvent reduced density of 1.1. Two temperatures, 50K and 250K, were simulated for this density to investigate the temperature effects. At both temperatures, the thermodynamic states for the high density correspond to solid solutions. We will show below that the solids we generated were amorphous solids which were different from crystalline xenon obtained under laboratory conditions. Since our primary interest is to investigate the possibility of observing cage-induced coherent oscillatory motion of unstable molecules in amorphous environments, this result is suitable. We also used a solvent state with reduced density of 0.9 at a temperature of 180K. The crystalline xenon with $\rho^*=1.1$ as solvent was also simulated at 30K to investigate the effects of crystalline order. The dynamics were drastically different from that in amorphous (glassy) solutions.

Table 5.2 lists the solvent density in g/cm^3 for the solutions we used in this study. Figs. 5.6 through 5.9 present the radial distribution functions of these solvent states defined as

$$g(r) = \frac{V}{N^2}\left\langle \sum_i \sum_{j \neq i} \delta(\vec{r} - \vec{r}_{ij}) \right\rangle \tag{5.39}$$

where $\vec{r}_{ij}$ is the vector from atom i to atom j, N is the total number of particles, and V is the volume. These radial distribution functions were calculated through averaging over the ensemble of either 1,024 or 4,096 trajectories rather than through the traditional way of averaging over time by propagating a single trajectory. The two lower density solutions correspond to liquid xenon. The highest density solutions, on the other hand, correspond to glasses.

Table 5.2 The correspondence of xenon reduced density with density in g/cm^3

ρ^*	0.7	0.9	1.1
d (g/cm^3)	2.3	2.9	3.6

The radial distribution function of the latter shows distinctive split second peak for the low temperature (T$\approx$50K) case and a flat top second peak for the high temperature (T$\approx$ 250K) case. These are distinctive features of the g(r)'s of amorphous Lennard-Jones solids (glasses) [5.61-5.64]. It was also suggested [5.64] that if we define

$$R = g_{min}(r)/g_{max}(r) \tag{5.40}$$

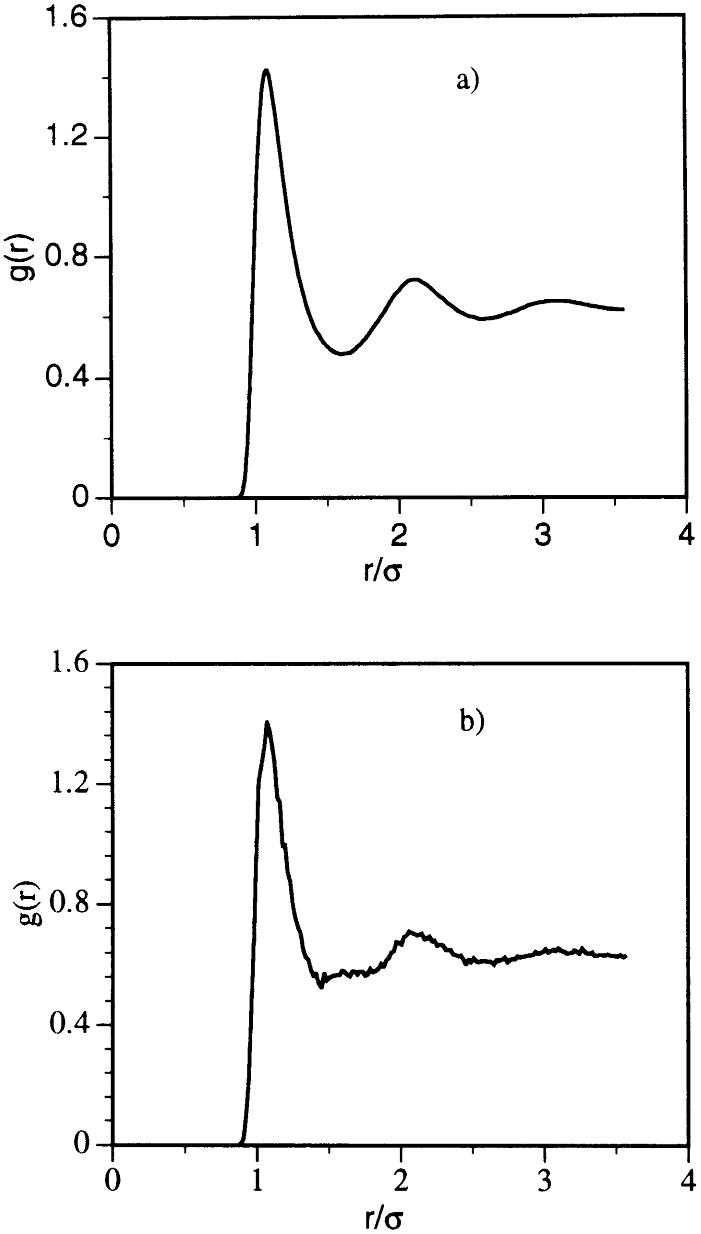

Figure 5.6 g(r) of ρ*=0.7 and T=250K solution.
a) Xe-Xe; b) I-Xe

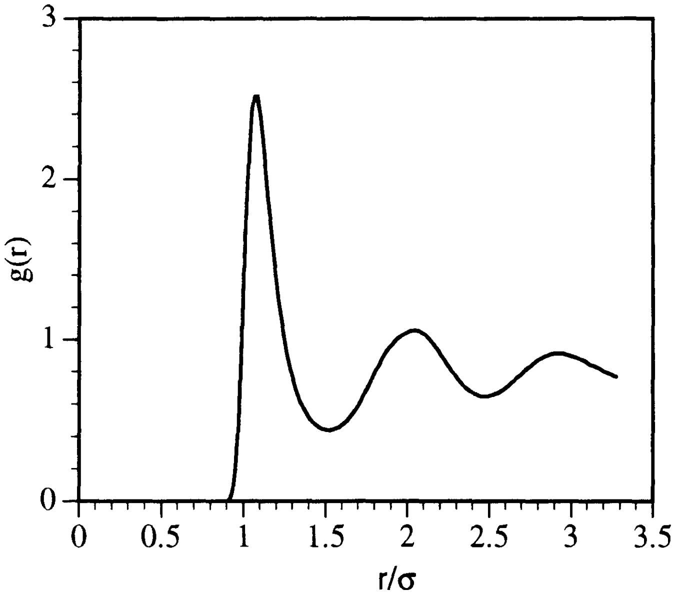

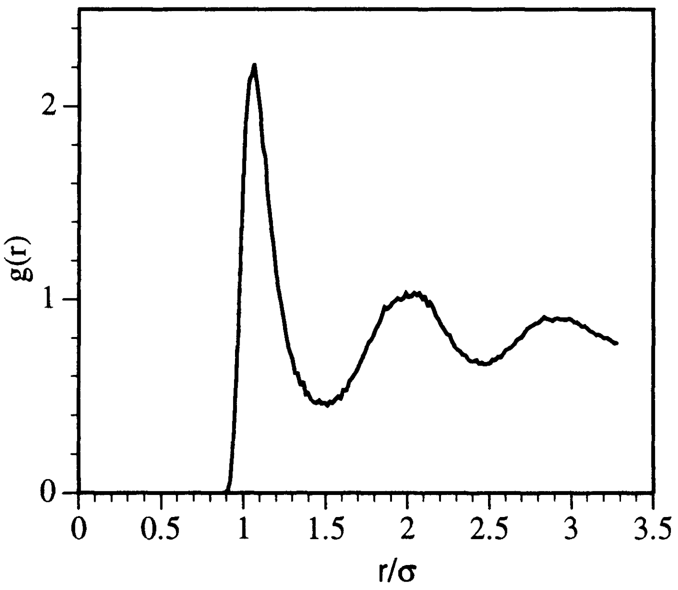

Figure 5.7 g(r) of ρ*=0.9 and T=180K solution.
Top: Xe-Xe; Bottom: I-Xe

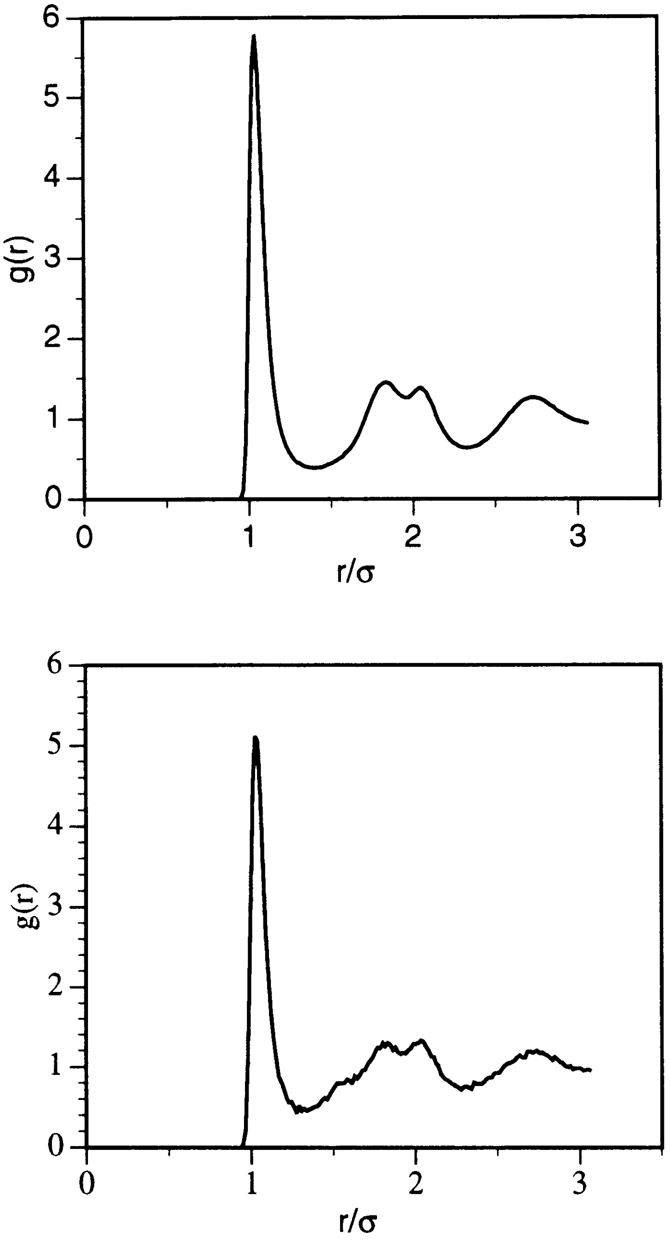

Figure 5.8 g(r) of $\rho^{*}=1.1$ and T=50K solution.
Top: Xe-Xe; Bottom: I-Xe

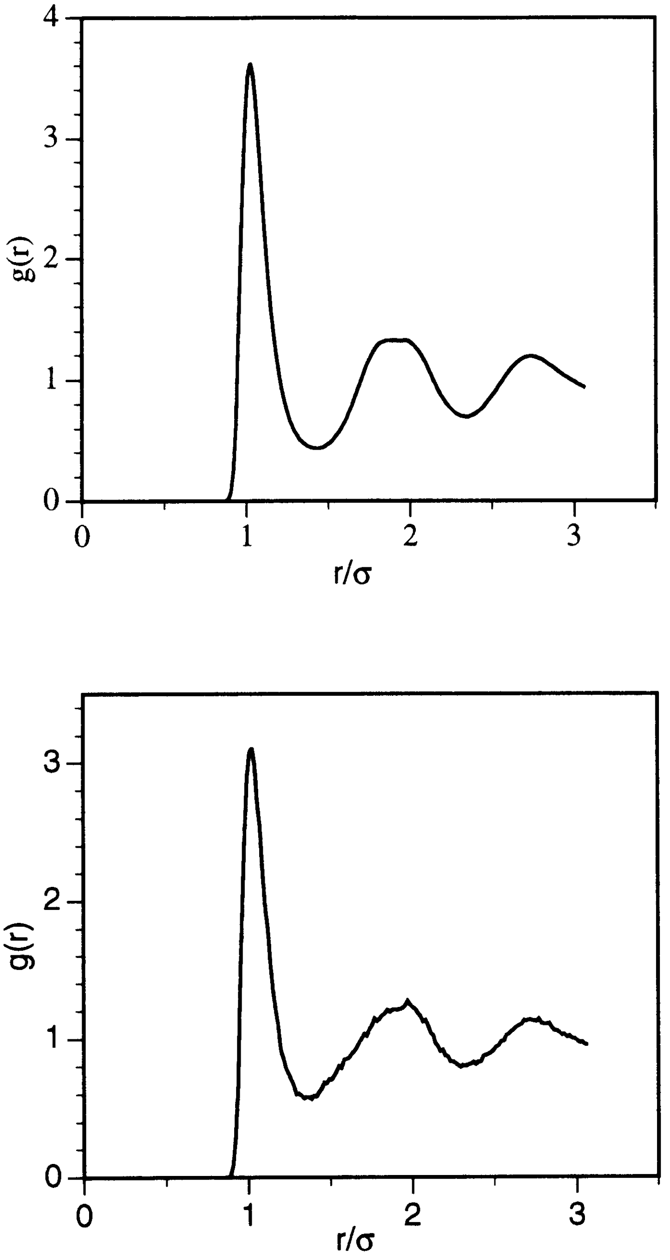

Figure 5.9 g(r) of ρ*=1.1 and T=250K solution.
Top: Xe-Xe; Bottom: I-Xe

where $g_{min}(r)$ is the magnitude of the first minimum and $g_{max}(r)$ is the magnitude of the first maximum in g(r), then the liquid/glass boundary is $R \approx 1.4$ with liquids having larger R's. Table 5.3 lists the R value for the four solvent states. They are consistent with our categorization. These results indicate that the molecular dynamics results reported for these systems should be more relevant to glasses and liquids rather than to ordered crystalline solids which have been studied in the past [5.65-5.68].

Table 5.3 R value for the solvent state used in this study.

	$\rho^*=0.7$, $T \approx 250K$	$\rho^*=0.9$ $T \approx 180K$	$\rho^*=1.1$ $T \approx 250K$	$\rho^*=1.1$ $T \approx 50K$
R	0.33	0.18	0.12	0.07

Fig. 5.10 shows the g(r) of a xenon crystal with $\rho^*=1.1$ and $T \approx 30K$. The ordered crystal lattice structure is obviously seen. The results for this system will serve for comparison to the results for amorphous solutions. It is of interest to notice that under laboratory conditions, Lennard-Jones systems form crystalline solids only. Amorphous Lennard-Jones solids have only been generated through molecular dynamics simulations due to the fast quenching rate in molecular dynamics runs: in our simulations, for example, quenching rate was on the magnitude of 10^{12} K/s which is many orders of magnitude larger than laboratory achievable quenching rate of 10^8 K/s. However, these computer generated glasses possess many of the important features real glasses possess and have been used as vehicles to study glass properties and dynamics through molecular dynamics simulations.

Fig. 5.11 through 5.15 presents the instantaneous normal mode density of the solvents. The two liquids have large density of imaginary frequencies which are plotted in

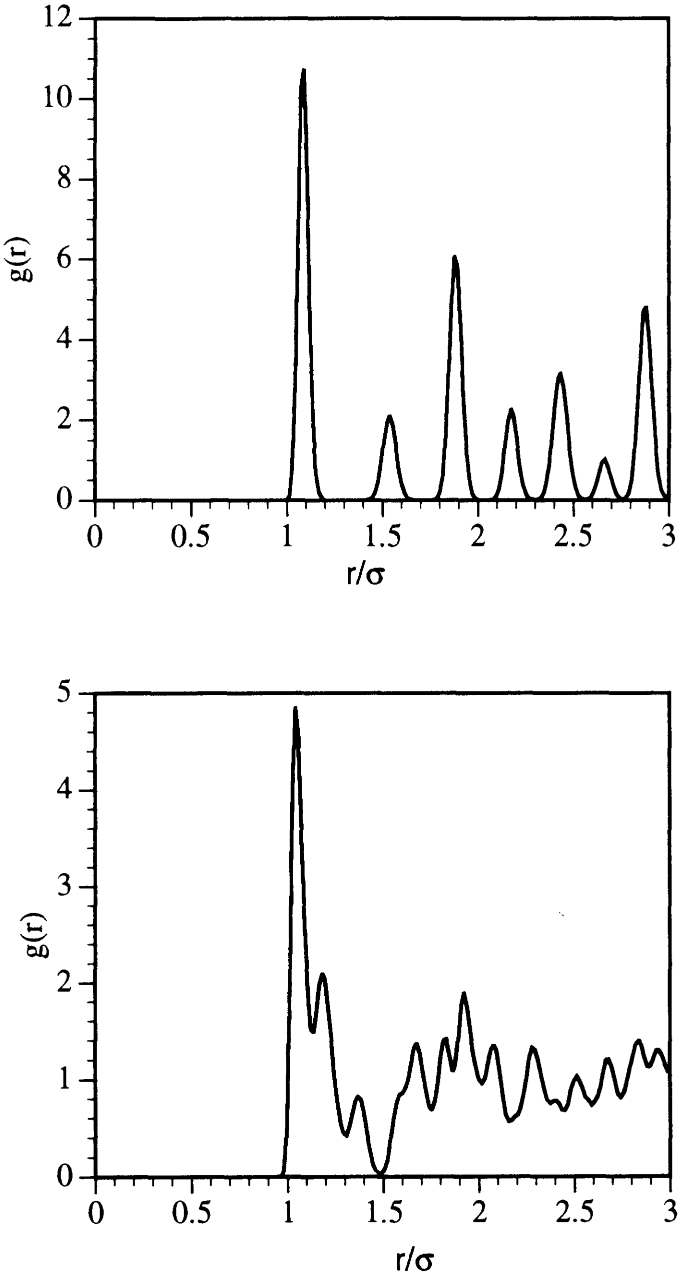

Figure 5.10 g(r) of ρ*=1.1 and T=30K crystal solution. Top: Xe-Xe; Bottom: I-Xe

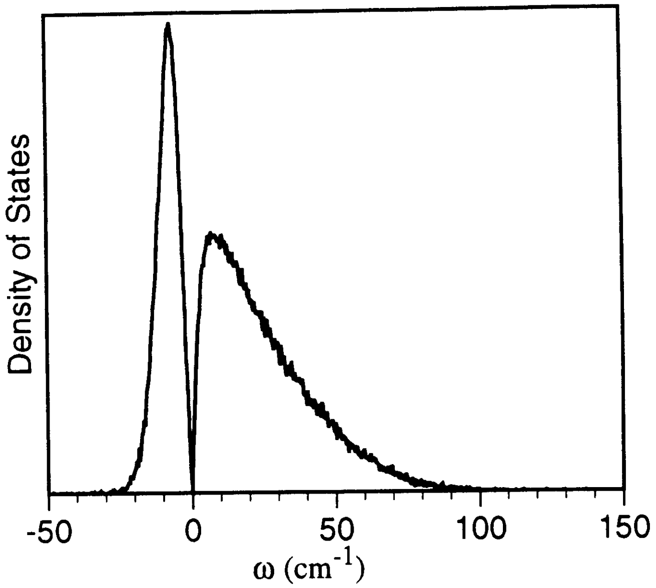

Figure 5.11 Density of States of xenon liquid $\rho^*=0.7$ at 250K.

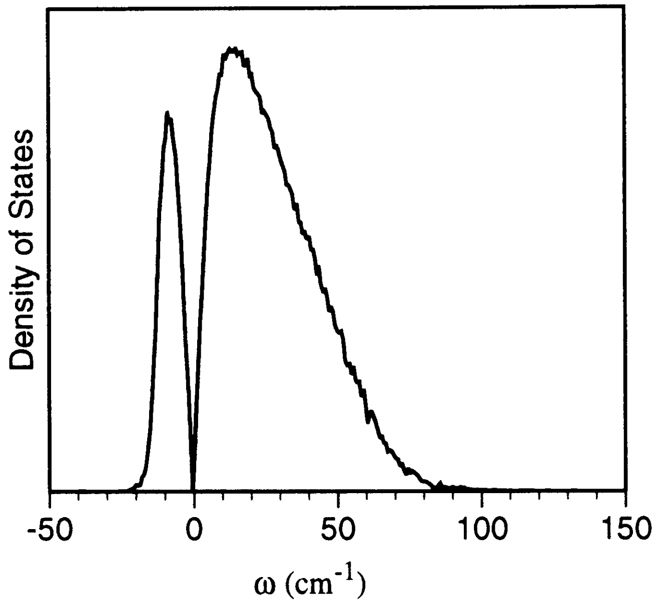

Figure 5.12 Density of States of xenon liquid $\rho^*=0.9$ at 180K.

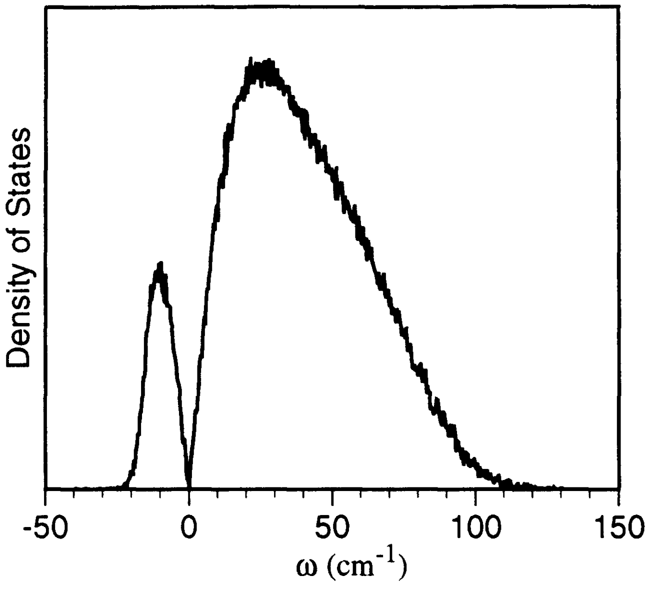

Figure 5.13 Density of States of xenon liquid ρ*=1.1 at 250K.

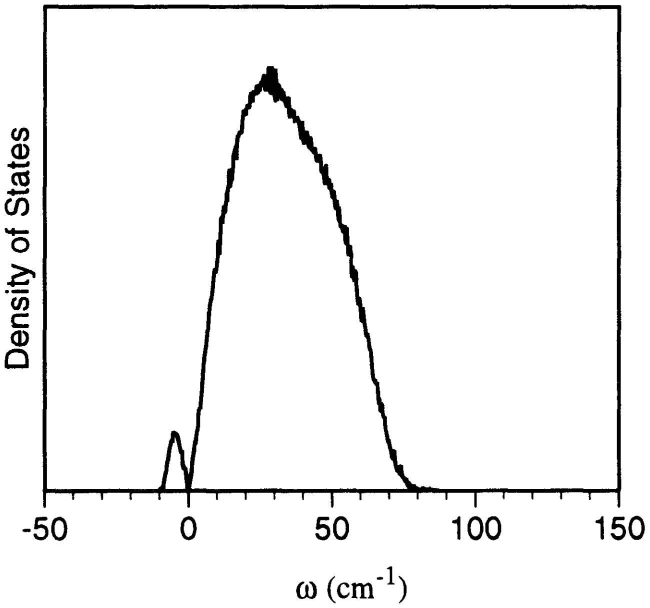

Figure 5.14 Density of States of xenon liquid ρ*=1.1 at 50K.

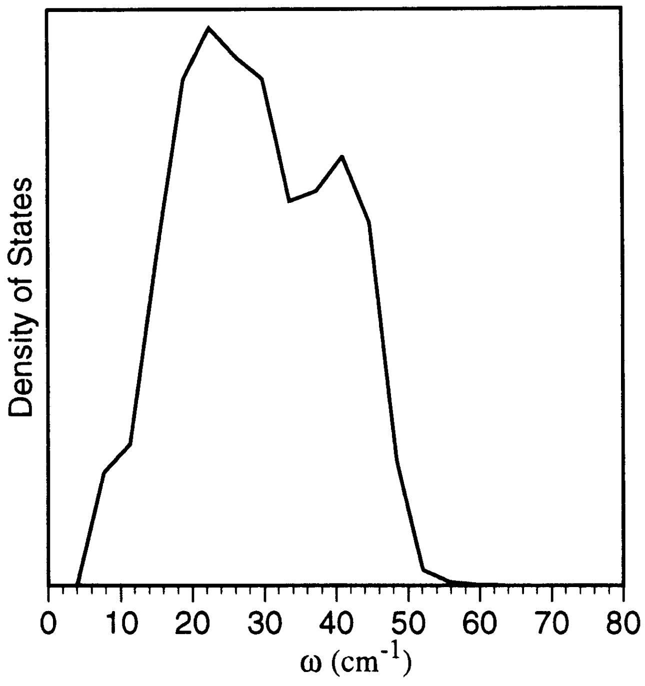

Figure 5.15 Density of States of xenon crystal $\rho^*=1.1$ at 30K.

the negative side following convention. The two glasses have much smaller imaginary part while the crystal has no imaginary part at all.

5.4.2 I_2 and "Light I_2" In Liquid and Amorphous Solid Solutions

The first system we studied was modeled after I_2. As mentioned before, this molecule has been the prototype for studying cage effects both experimentally and theoretically. The potential energy surfaces are well studied and relatively simple. Again this is a simplified I_2 model. The actual photodissociation dynamics of I_2 include both predissociation from its bound B state and curve crossing to other states at the asymptotic region. We have ignored these effects and considered only the $^1\Pi_u$ state with no curve crossing.

Fig. 5.16 shows the simulation results for the low-density ($\rho^*=0.7$), high-temperature ($T \approx 250K$) solution. We use the term 'low' here in comparison to the higher density discussed below. This density actually corresponds to that of a typical liquid at ambient pressure. The first panel shows the average internuclear distance between the two iodine atoms as a function of time. Following photoexcitation ($t = 0$), there is a rapid increase due to the repulsive molecular potential energy surface and then a more gradual increase as I fragments continue to move apart. The second panel shows the force autocorrelation function $\langle \mathbf{F}(0) \cdot \mathbf{F}(t) \rangle$ and reorientational autocorrelation function $\langle P_2[\cos\theta(t)] \rangle$ of the I-I pair. Here $\mathbf{F}$ is the component of the total force between the two iodine atoms projected along the I-I direction:

$$\mathbf{F}(t) = [\mathbf{F}(\mathbf{r}_2) - \mathbf{F}(\mathbf{r}_1)] \cdot (\mathbf{r}_2 - \mathbf{r}_1) / r_{12} \qquad (5.41)$$

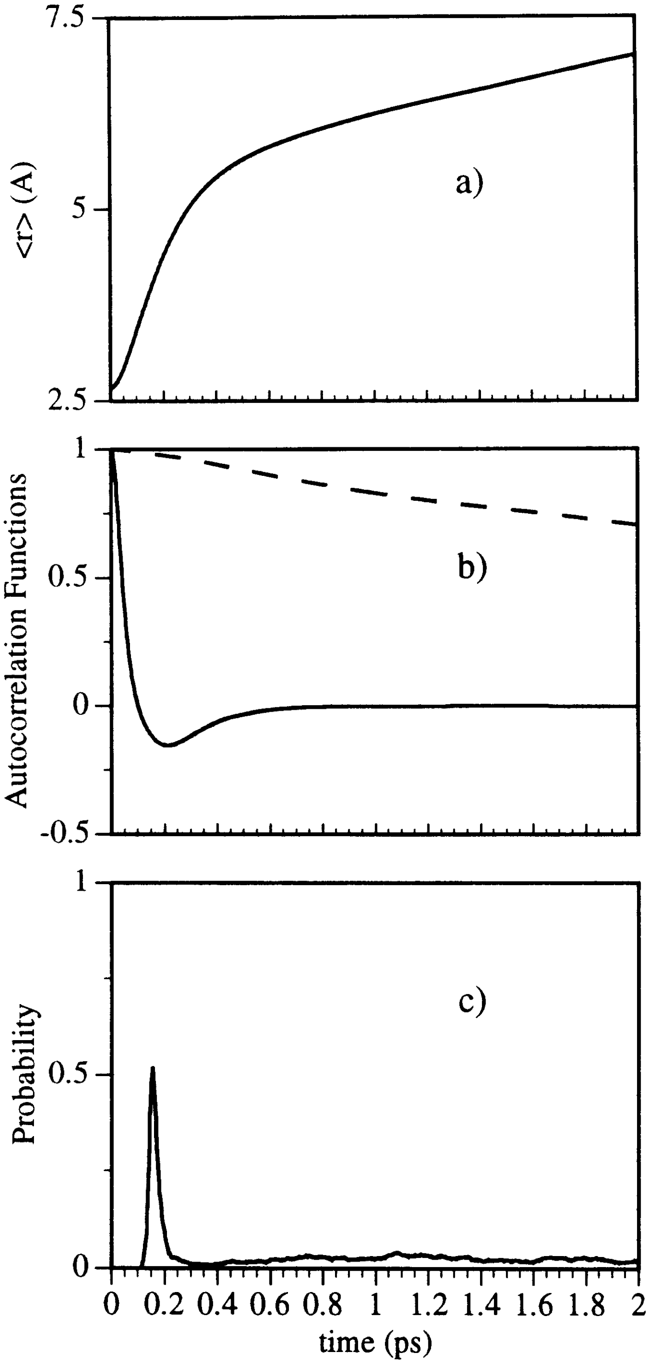

Figure 5.16 Results for the ρ*=0.7 solution at 250K.

where $\mathbf{r}_1$ and $\mathbf{r}_2$ are positions of the two iodine atoms and $\mathbf{F}(\mathbf{r}_1)$ and $\mathbf{F}(\mathbf{r}_2)$ are the total forces on the two iodine atoms. $\theta(t)$ is the angle between the initial I-I direction and the I-I direction at time t, and

$$P_2[\cos\theta(t)] = \frac{1}{2}[3\cos^2\theta(t) - 1] \tag{5.42}$$

Since the initial force $\mathbf{F}(0)$ is predominantly the repulsive force of the I atoms against each other, the force autocorrelation function provides a good illustration of the cage influence on molecular dynamics. The result shows that after about 200 fs, the net force on the fragments favors motion back toward each other. However, the monotonic increase in interatomic distance (top curve) indicates that the solvent restoring force is insufficient to overcome the momentum toward separation. The reorientational autocorrelation function shows that within the time interval of interest, molecular alignment is largely preserved. The bottom panel shows the probability of finding the I-I separation within a predefined window on the excited-state potential surface. This quantity was used to estimate the results of a femtosecond transient absorption experiment. A precise calculation would require detailed potential energy surfaces for both the initial and final states involved in the probing process, the transition dipole moment for the probe wavelengths, and inclusion of the effects of reorientation [5.55]. The goal in the present work is simply to assess whether oscillatory dynamics might be observed with realistic averaging over an ensemble of trajectories. We used a window of width 0.2 Å centered at a position (I-I separation) of 3.5 Å . The qualitative behavior was found to be similar for all positions along the potential energy surface. The result is consistent with the top figure. Shortly after photoexcitation, the average I-I separation increases to the specified range (around 3.5 Å). There is no recurrence observed in this system since most of the molecules dissociate rather than oscillate. A more complete plot of the probability distribution of I-I distances is shown in Fig. 5.17. The I-I distances spread monotonically and quickly over time.

Fig. 5.18 presents the results for the high-density ($\rho^*=1.1$), high-temperature ($T \approx 250K$) solution. New features are apparent which indicate a more significant role played by the solvent at higher density. The top panel shows that the average I-I interatomic distance does not increase monotonically but instead increases until a maximum is reached and then decreases to a "steady-state" value of about 3.7 Å . There appears to be a weak oscillation about this value. The force autocorrelation function (second panel) also shows these features clearly. The third and fourth panels respectively show the probability of finding the I-I separation within a predefined window of width 0.2 Å centered at positions (I-I separations) of 3.25 Å and 3.85 Å. These values represent probing at the inner and outer (cage) potential "wall" respectively. At the inner wall, we see first a sharp peak corresponding to the initial passage of the ensembles of trajectories through the probing region. Then there is a slower rise due to the return of some molecules to this geometry following rebound off the solvent cage potential wall. Superimposed on this rise appears to be a weak oscillation whose period seems to match that of the force autocorrelation function. A corresponding result is observed at the outer probing window. The initial rise occurs later than at the inner window since the dissociating molecules take longer to reach this geometry. The subsequent decrease reflects the rebound of molecules toward smaller internuclear separations. There is a weak minimum in the probability of the outer I-I separation which matches well with the weak maximum in the inner separation. After this no oscillatory character is apparent.

Fig. 5.19 shows the major results for the high-density ($\rho^*=1.1$), low-temperature ($T \approx 50K$) solution. Oscillatory motion in the molecular repulsive electronic excited state is clearly seen in the average internuclear distance (top panel) as well as the force autocorrelation function (second panel). The last two panels show the probability of finding

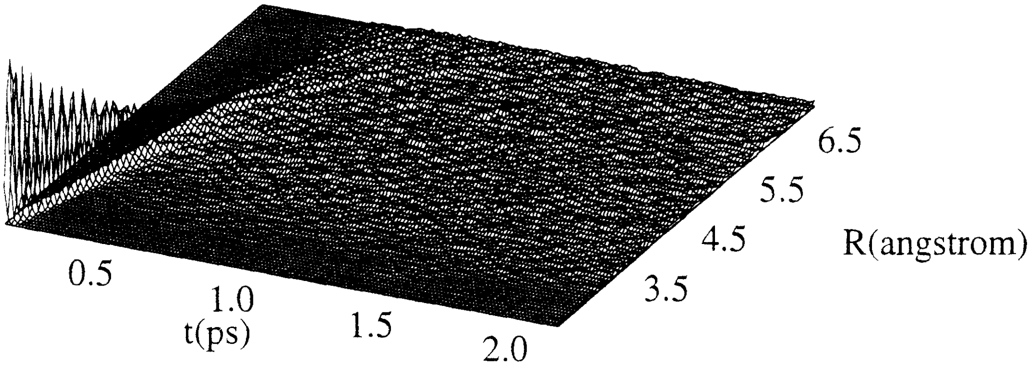

Figure 5.17 Probability distribution function of I-I distances in ρ*=0.7 solution at 250K.

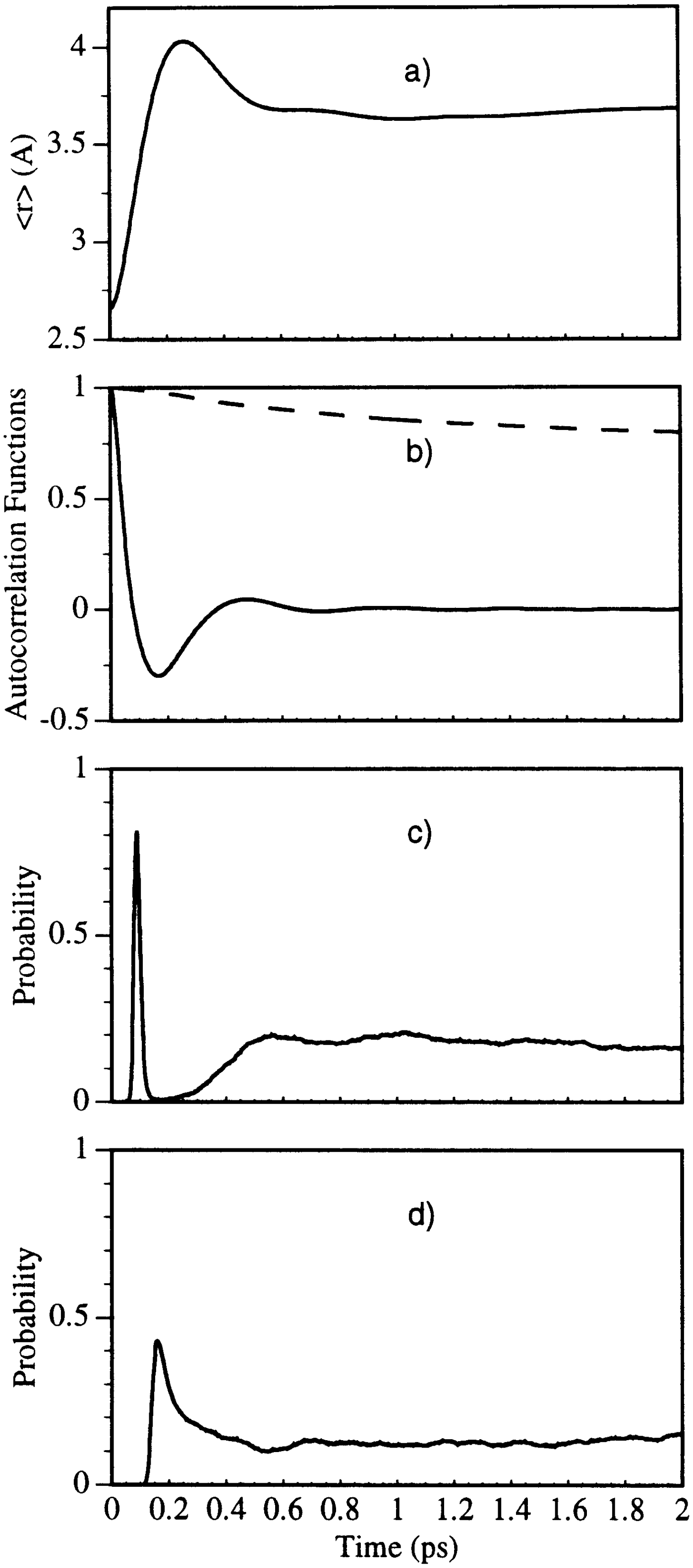

Figure 5.18 Results for the ρ*=1.1 solution at 250K.

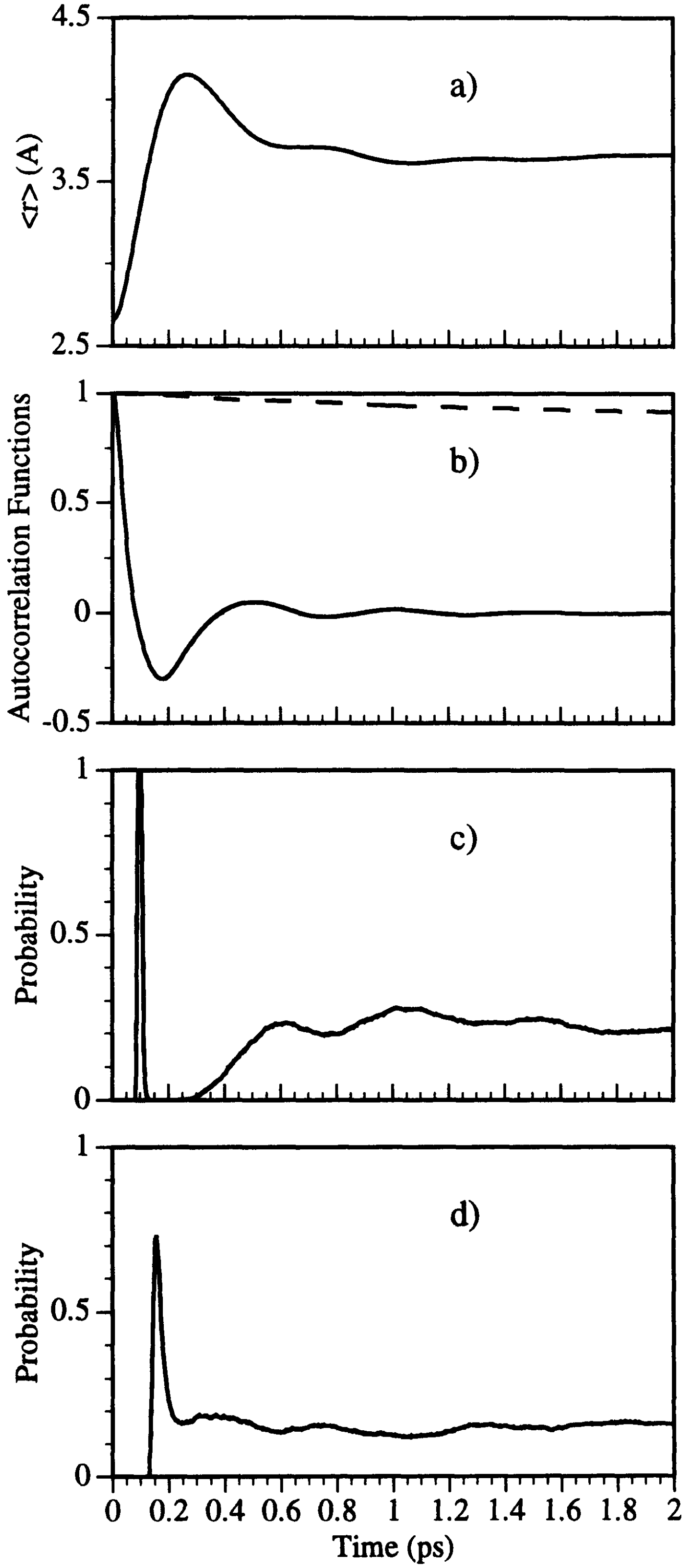

Figure 5.19 Results for the ρ*=1.1 solution at 50K.

the I-I separation within windows of the same width as in Fig. 5.18 while centered at 3.35 Å and 3.85 Å on the potential surface. These also show very clearly oscillatory character, with the oscillation period matching very closely that of the force autocorrelation function. An additional feature associated with the outer probing region is the splitting of the first peak. This corresponds to the swarm of trajectories moving through the probing region, reaching larger separations, and moving back through the probing window on the rebound toward shorter separations. Similar results were observed experimentally when probing wave packets away from the classical turning points of bound potential energy surfaces in gas phase NaI [5.69] and Na_2 [5.70], of I_2 in solution [5.27, 5.28], and of a protein [5.71]. The high-density, high-temperature solution did not show this feature, presumably because of a greater width of the probability distribution function at higher temperature which washed it out. This width was also apparent in results like those shown in the bottom two panels of Fig. 5.19 but with the window at around the center of the two values chosen in the figure. In this case the oscillations, which would be at twice the vibrational frequency, are not resolved.

I-I pair distribution functions on the excited-state potential energy surface in these two high density solutions are shown in Fig. 5.20. The bottom panel shows the high-density, low-temperature solution in which the oscillatory response and the spreading of the probability distribution function can clearly be seen. Probability distribution function spreading occurs more rapidly at higher temperatures (top panel).

In order to study how energy flows from I_2 to the solvent, we calculated the kinetic energies of the iodine "molecule" and of the first and second shells of solvent atoms. We define the first solvent shell as containing those xenon atoms which are within 1.5 σ_{Xe-I} of either of the two iodine atoms. The second shell was defined as containing xenon atoms between 1.5 σ_{Xe-I} and 2.5 σ_{Xe-I}. away from either I atom. These two locations correspond to the first two minima in the g(r) (see Figs. 5.6 through 5.10). This is a rather crude

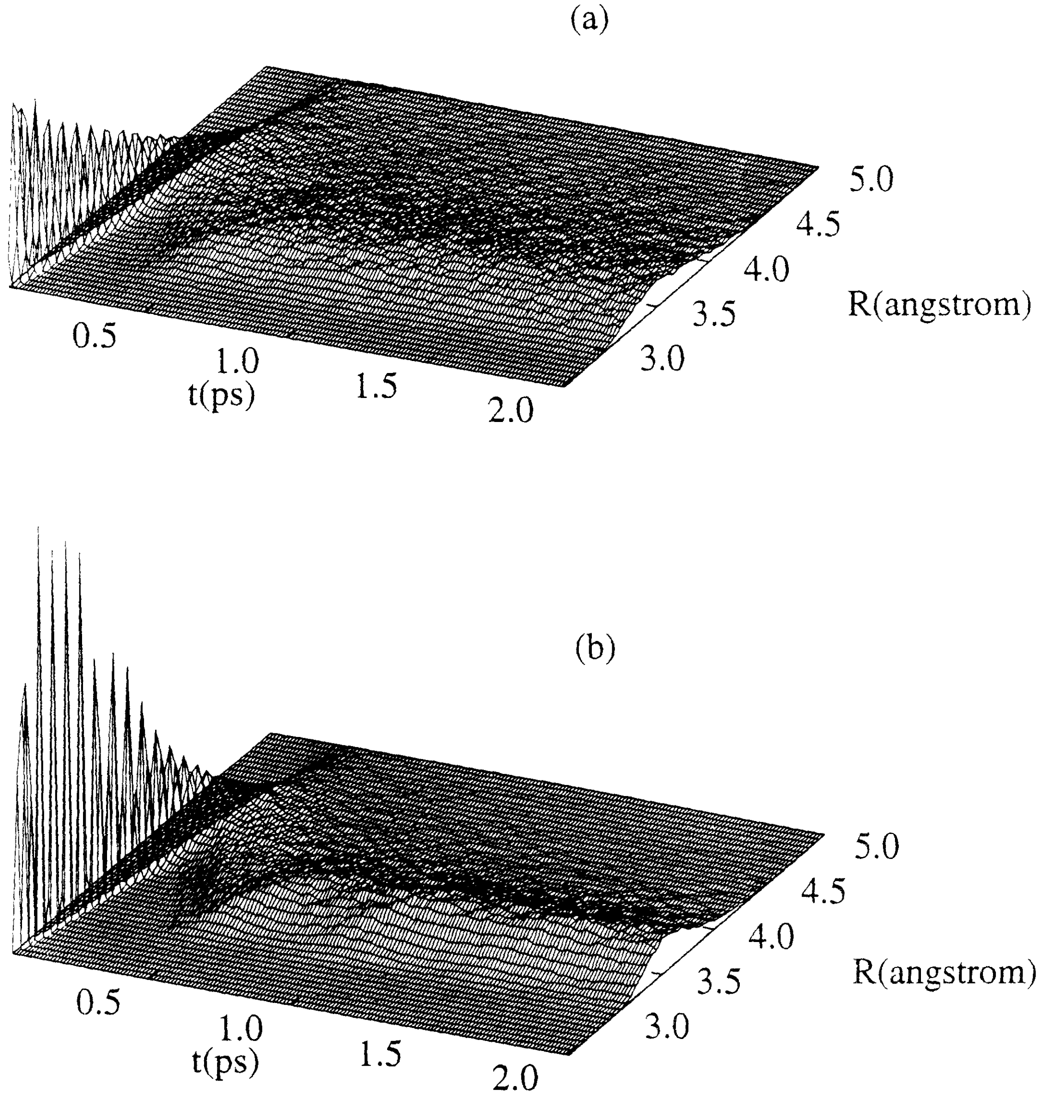

Figure 5.20 Probability distribution functions of I-I distances in $\rho^*=1.1$ solutions. a) T≈250K; b) T≈50K.

definition, especially when the I-I separation is large. However, our primary interest is in the behavior before very large separations are reached. Figs. 5.21 and 5.22 show respectively the ensemble averaged kinetic energy per atom as a function of time for I_2 and for the solvent shells. Fig. 5.21 shows that in all cases molecules lose most of their excess energy during the first collision with the solvent cages. There are no significant oscillations in kinetic energy curves although there is a shoulder in the $\rho^*=1.1$ and $T \approx 50K$ case. This is in accordance with the fact that in cases of oscillatory motion, kinetic energy oscillates at twice the fundamental frequency of the oscillation and therefore cannot be resolved. Fig. 5.22 indicates that in all cases there is substantial energy transfer to the first solvent shell during the first collision, with a lag before energy is transferred to the second shell. Very efficient heat dissipation from the first and second shells into the bulk of the solution is also clearly shown. By 2 ps after photoexcitation, roughly uniform local solvent temperature has been reached and the temperatures are within 15K of their initial values. The detailed time dependence of the energy flow also reflects the different dynamical behavior in different cases. In the high density solutions, energy transfer to the first shell shows a clear second maximum (see panel c) in Fig. 5.22, which indicates that energy transfer from the first shell into the second shell was not completed after the first set of solvent-solvent collisions. In the low density solution, however, no such second maximum was observed. Picosecond Raman experiments [5.72] on I_2 in CCl_4 have shown that this transient heating of the solvent cage can be observed when using a molecular solvent. Heating occurred within the experimental time resolution of 15 picoseconds. Our results suggest that heating due to photodissociation should occur on a much faster time scale.

The fast energy dissipation suggested that although we can see cage-induced oscillations in the high density solutions we are still far away from the rigid cage limit. To illustrate this point, we scaled the iodine mass to one-fourth of its real value while keeping the other parameters unchanged. Due to the larger solvent/solute mass ratio, energy transfer

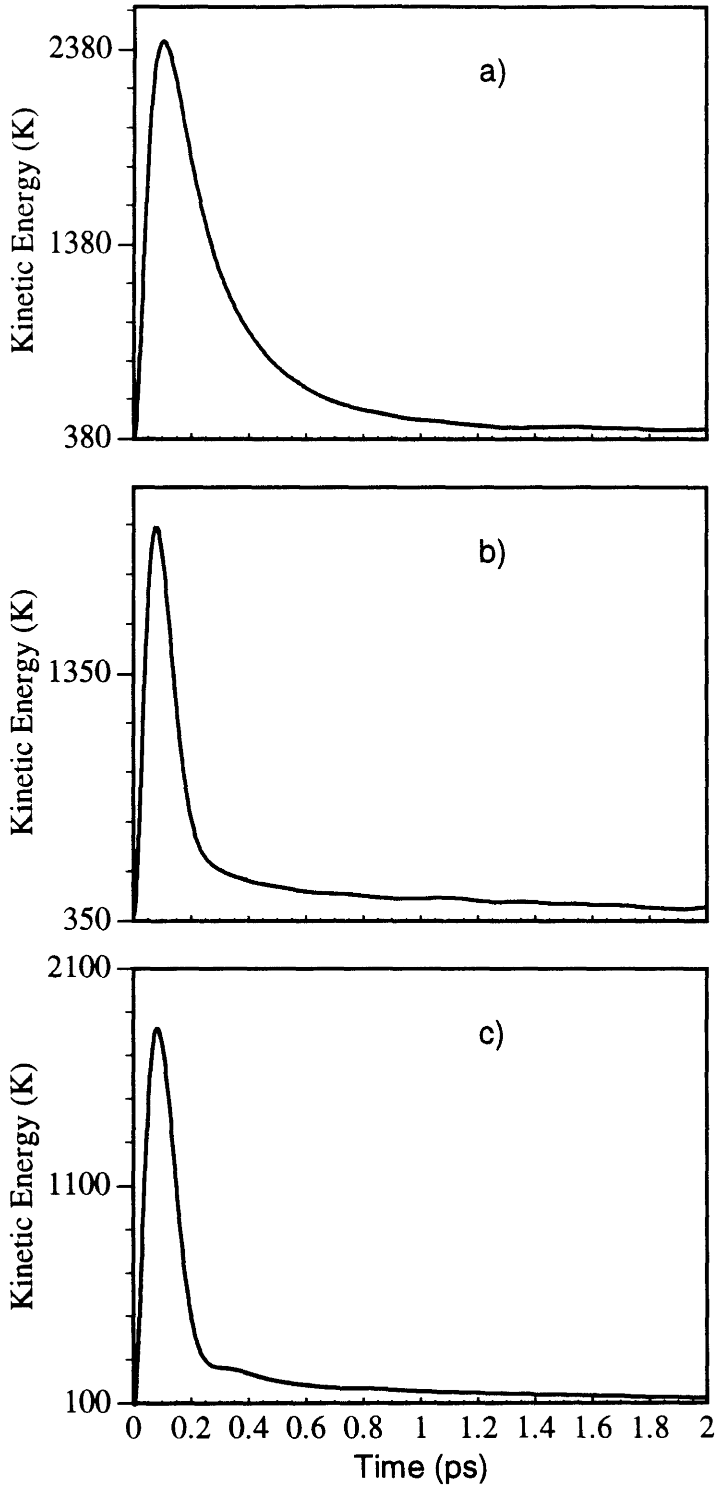

Figure 5.21 Iodine kinetic energy for the a) $\rho^*=0.7$ solution at 250K; b) $\rho^*=1.1$ solution at 250K; c) $\rho^*=1.1$ solution at 50K

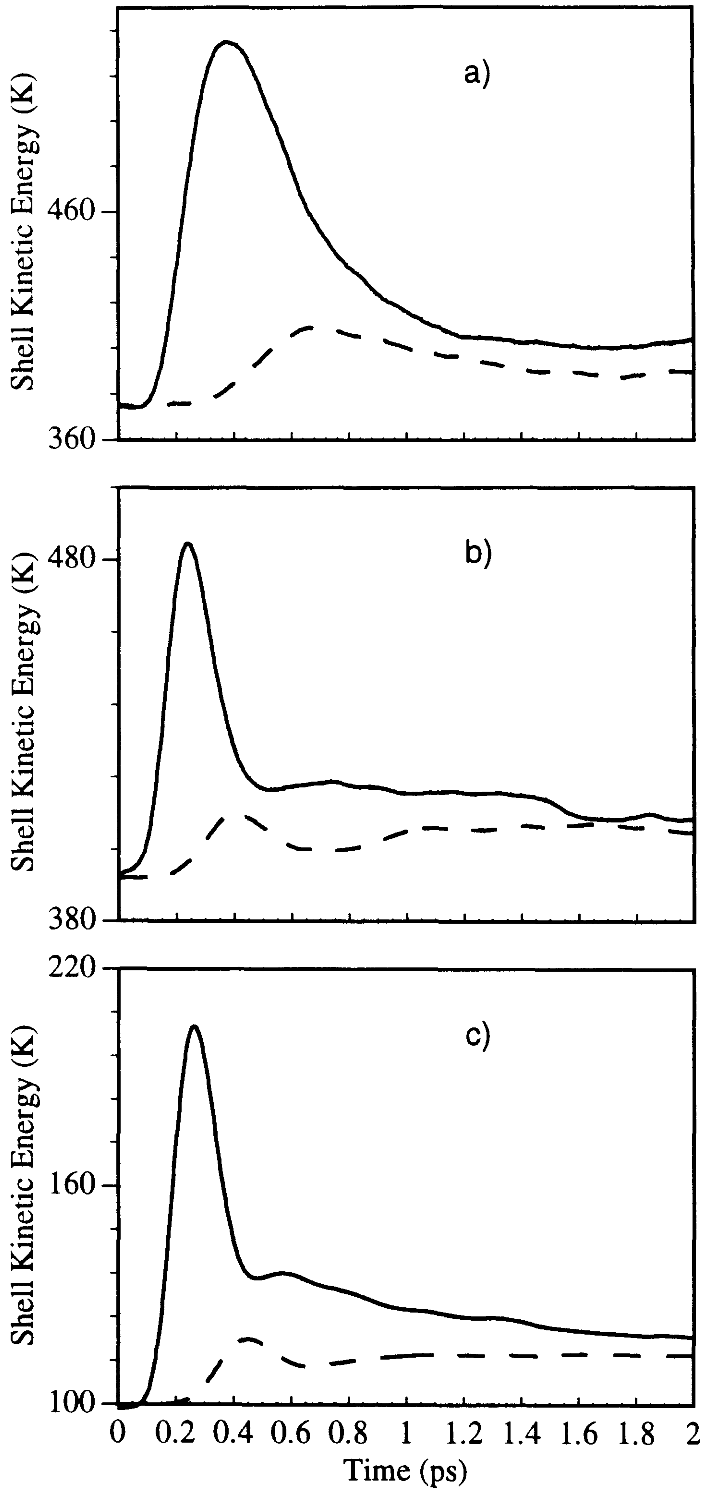

Figure 5.22 Shell kinetic energies for the a) ρ*=0.7 solution at 250K; b) ρ*=1.1 solution at 250K; c) ρ*=1.1 solution at 50K

from photoexcited "light iodine" to the solvent should be less efficient and therefore the system should be closer to the rigid cage limit [5.31-5.33]. Fig. 5.23 shows the results for this fictitious diatomic molecule in a $\rho^*=1.1$ and $T \approx 30K$ solution. As expected, energy transfer from the solute to the solvent is far slower than in the iodine solution under the same conditions. At 2 ps the solute kinetic energy is still about 300K above its initial value. The kinetic energy shows oscillations at twice the fundamental frequency in the first 500 fs. The kinetic energy rise in the first solvent shell is far less than in the iodine case. This stronger cage effect also manifests itself through larger oscillation amplitudes in <r> and the force autocorrelation function. The frequency of the motion is roughly twice the frequency of iodine solution under the same conditions, consistent with the reduction in "iodine" mass.

Fig. 5.24 a plots the probability distribution function for this system. Since there are more oscillations in this system, we can examine the dynamical behavior more closely. In Fig. 5.25 , we present the probability of finding the bond length at five values along the potential energy surface with the window width the same as previously used. At the inner potential wall (panel a), we can see recurrence up to 1ps with much larger modulation depth compared to the iodine system. Panel b shows that "incoming" and "outgoing" "wavepackets" can be resolved even in the inner wall region. Panel c corresponds to probing at around the bottom of the effective well formed by the intramolecular repulsive potential and the cage potential, where the "wavepacket" moves through twice every period. Note the increase of the baseline at long times for this probing region in comparison to decreases of baselines in the other four probing regions: molecules relax to the bottom of the well just like they do in a intramolecular potential well. At the outer potential wall, more recurrence with larger modulation depth can be resolved as compared to the I_2 system, similar to the results of inner potential wall probing.

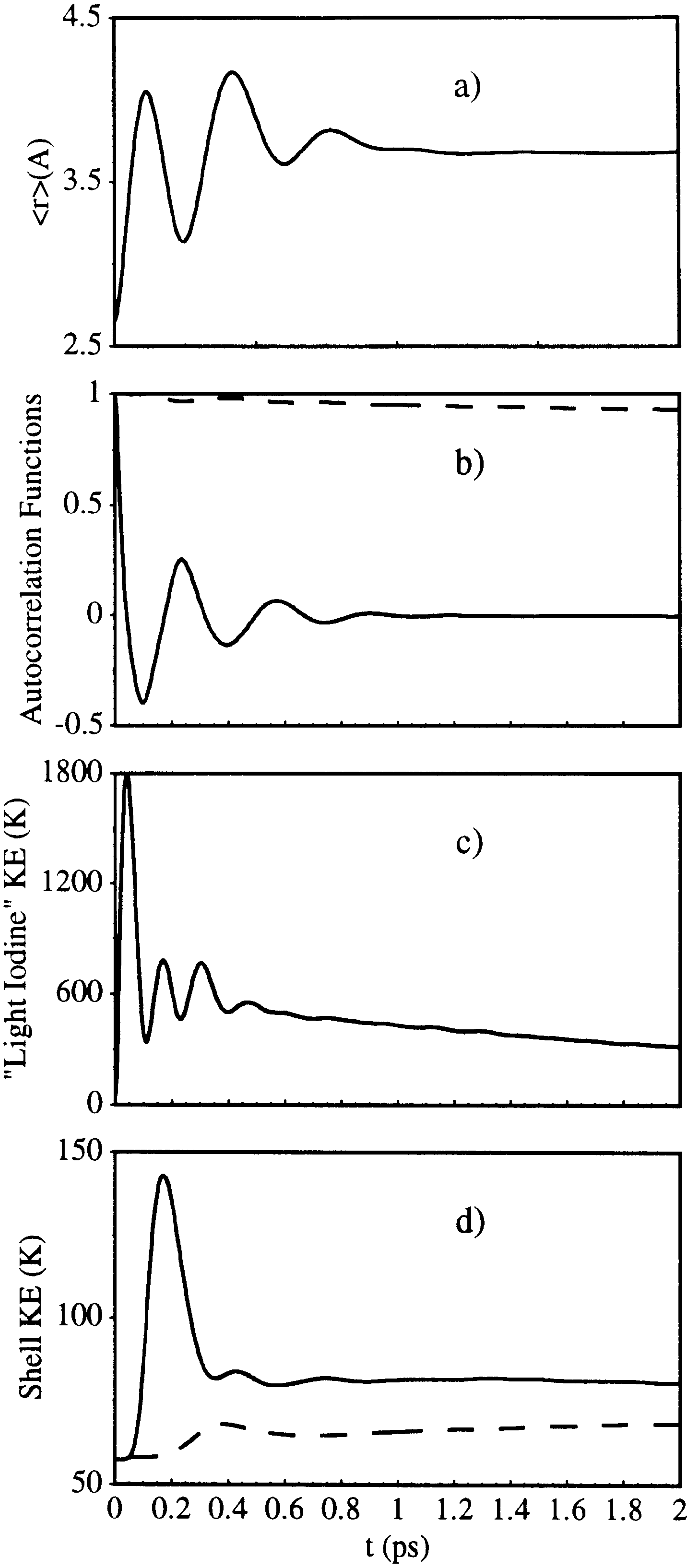

Figure 5.23 Results for the "light iodine" in the $\rho^*=1.1$ solution at 30K.

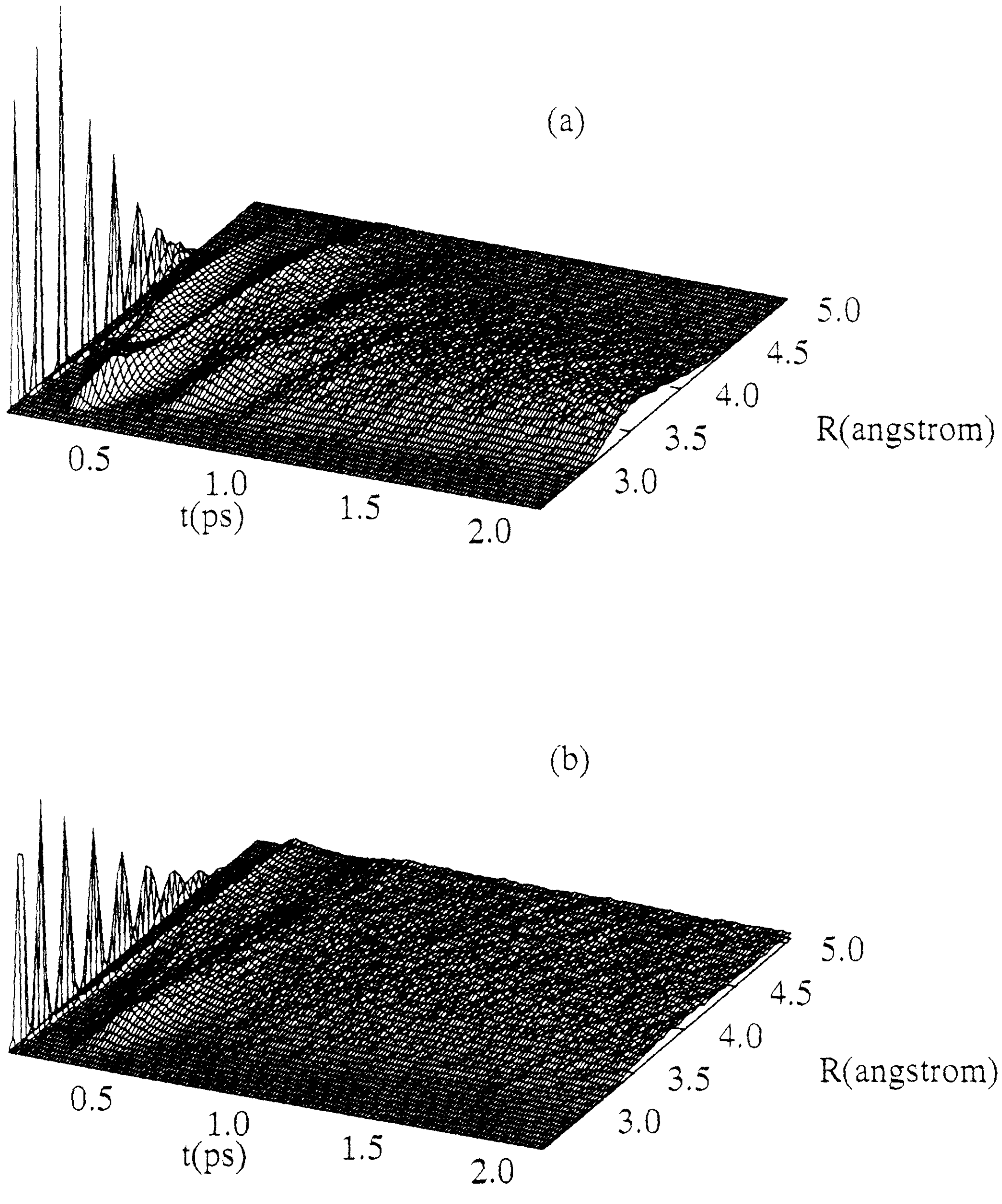

Figure 5.24 Probability distribution functions of I-I distances in $\rho^*=1.1$ solutions. a) $T\approx250K$; b) $T\approx50K$.

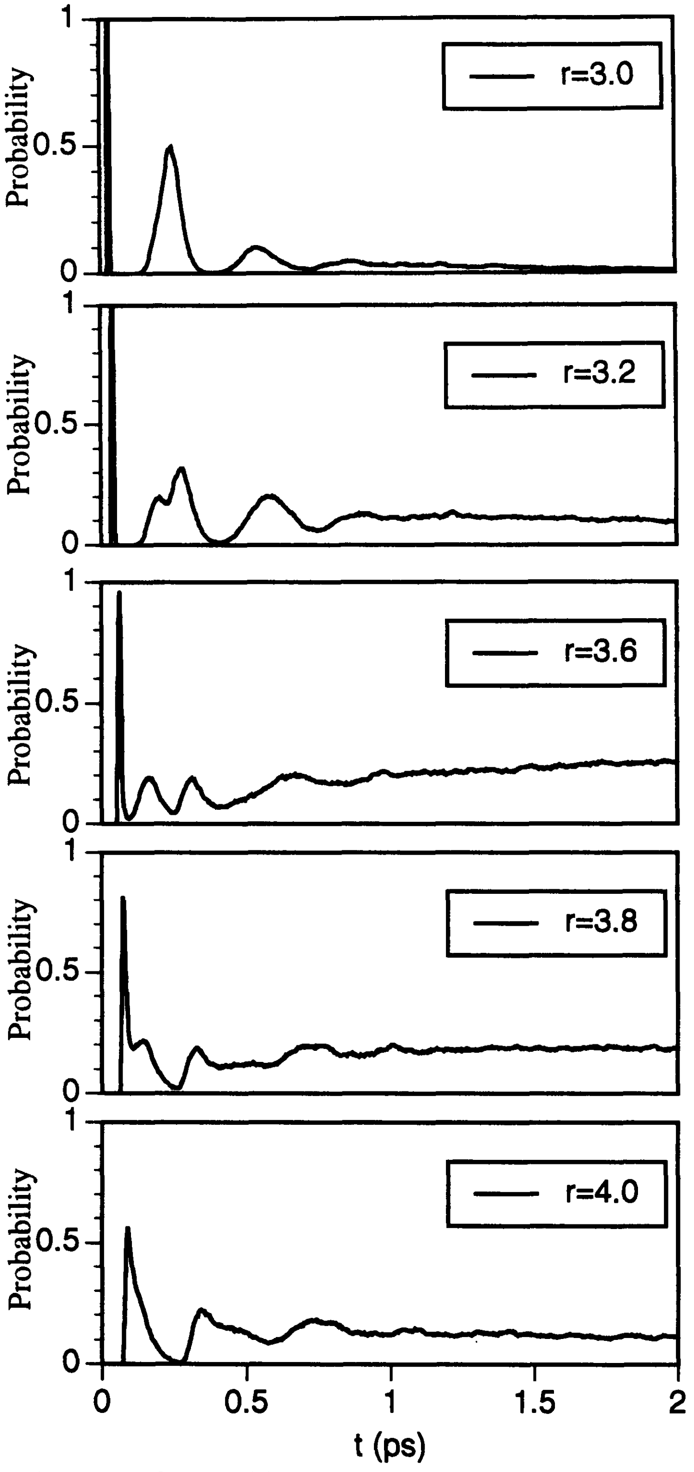

Figure 5.25 Probability distribution functions for the "light iodine" in ρ*=1.1 solution at 30K. The legend in each plot indicates the probing location (unit in Angstrom).

In order to show the general relevance of the results presented in this work to cage effects in liquid as well as glass solutions, simulations of "light iodine" in liquid xenon solution with reduced density $\rho^*=0.9$ and $T \approx 180K$ were performed. The results are shown in Fig. 5.26. A clearly oscillatory response is seen even though the long time behavior is dissociative rather than bound. The oscillation period is longer than in the higher density solution, reflecting weaker solvent forces. This type of case should be particularly interesting because it illustrates that cage-induced oscillations might be observed even when the solvent cage potential is not strong enough to trap the dissociation products for long. The probability distribution function of the "light iodine" bond length is plotted in Fig. 5.24. Fig. 5.27 presents "slices" of the probability distribution function at several locations along the potential curve. At the inner wall (top panel), clear recurrence exist just like in solid solutions. At the outer wall (bottom panel), again just like in solid solutions, the ensemble of trajectories moving in and out of the probing region can be resolved. The qualitative features in this liquid solution show no significant differences as compared to the solid solutions: from the "light iodine" point of view there is little difference between a solid or a liquid solution, at least as far as short-time dynamics including cage induced oscillation is concerned.

These results have shown that when solvent cage relaxation is slower than the solute motion, oscillatory behavior should be observed, even though the environment is inhomogeneous. From a frequency domain picture, this indicates that the mean oscillation frequency should be larger than the width of its distribution. Figs. 5.28 through 5.32 present the power spectra of the force autocorrelation functions. The power spectra were calculated by padding zeros to the data from 2 ps to 8 ps to improve spectral resolution. Since all features in the force autocorrelation functions are within about 1ps and the force autocorrelation functions decay to essentially zero after 2 ps, this procedure would not introduce significant errors. However it must be emphasized that this is only a way to

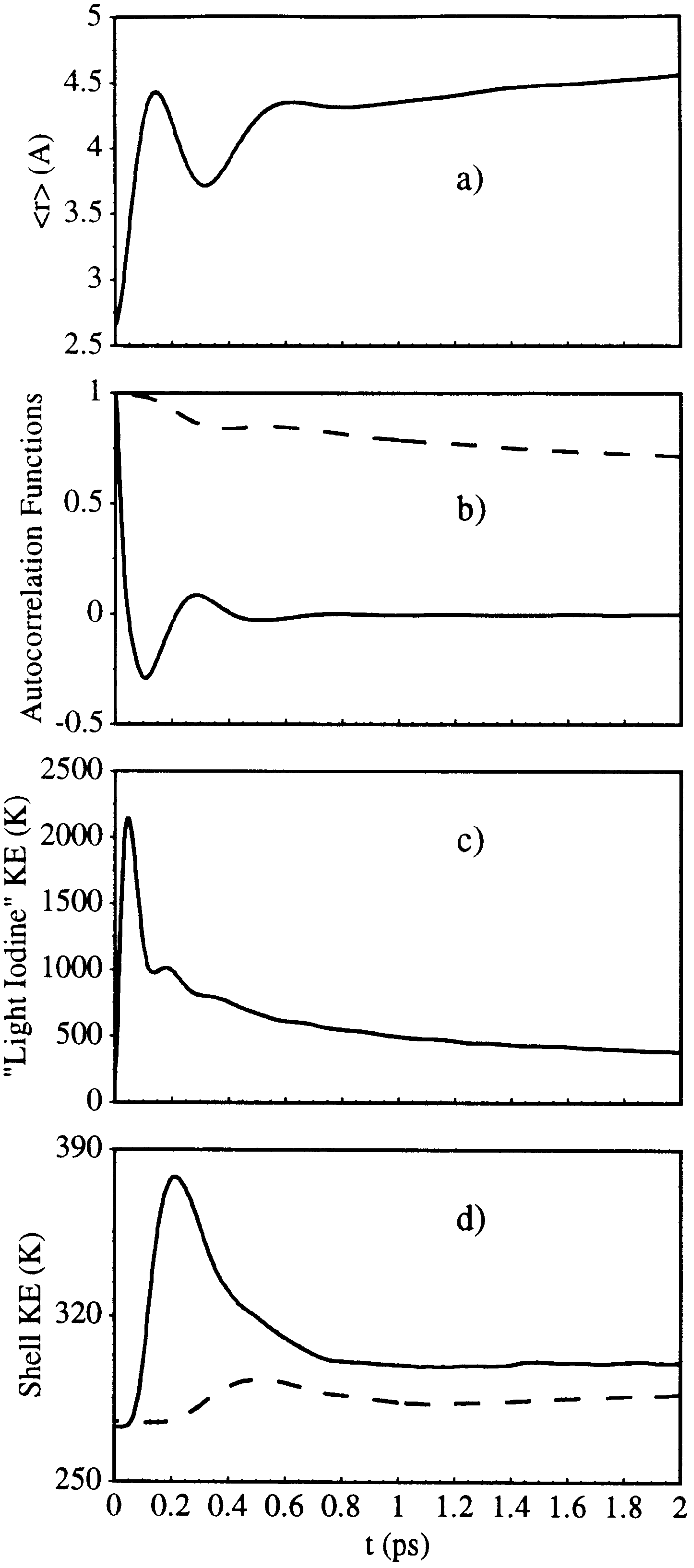

Figure 5.26 Results for the "light iodine" in $\rho^*=0.9$ solution at 180K.

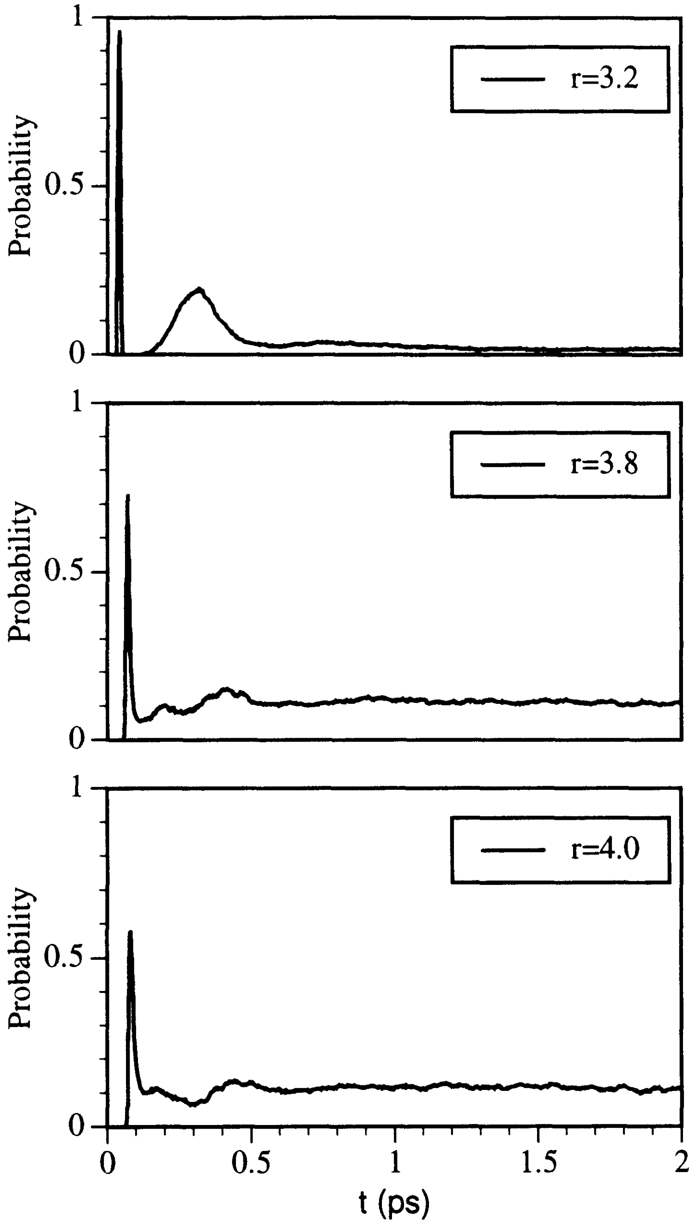

Figure 5.27 Probability distribution functions for the "light iodine" in ρ*=0.9 solution at 180K. The legend in each plot indicates the probing location (unit in Angstrom).

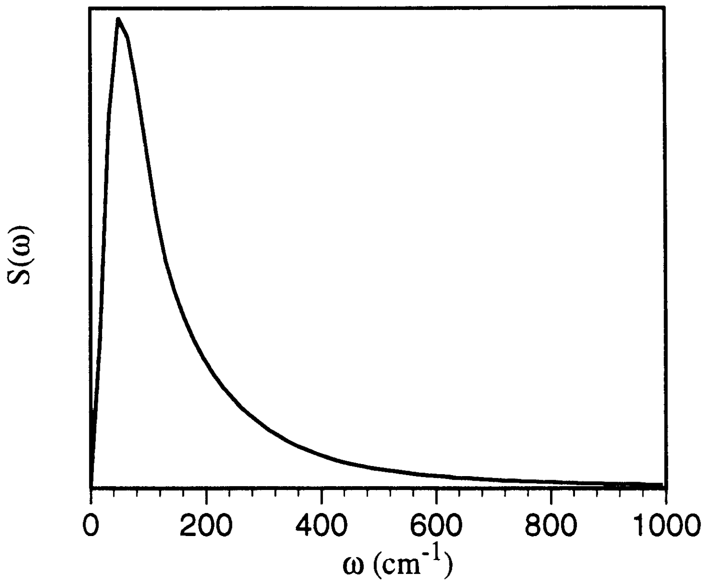

Figure 5.28 Power spectrum of the force autocorrelation function for iodine in $\rho^*=0.7$ solution at 250K.

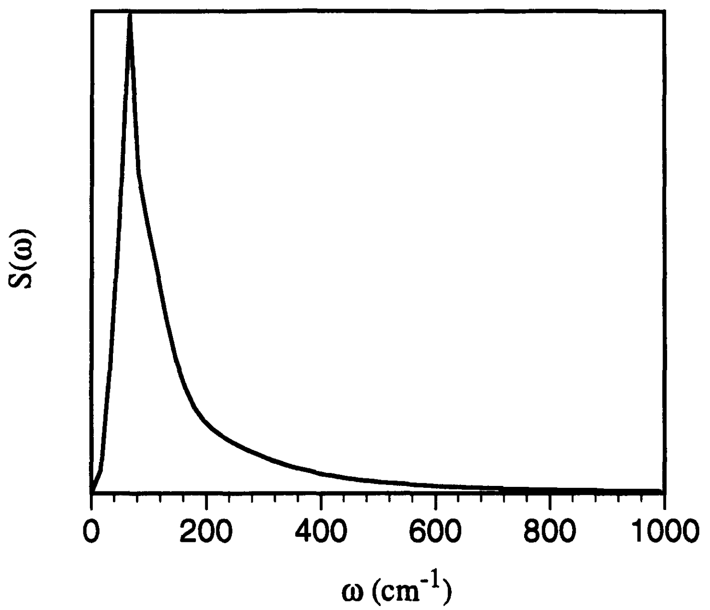

Figure 5.29 Power spectrum of the force autocorrelation function for iodine in ρ*=1.1 solution at 50K.

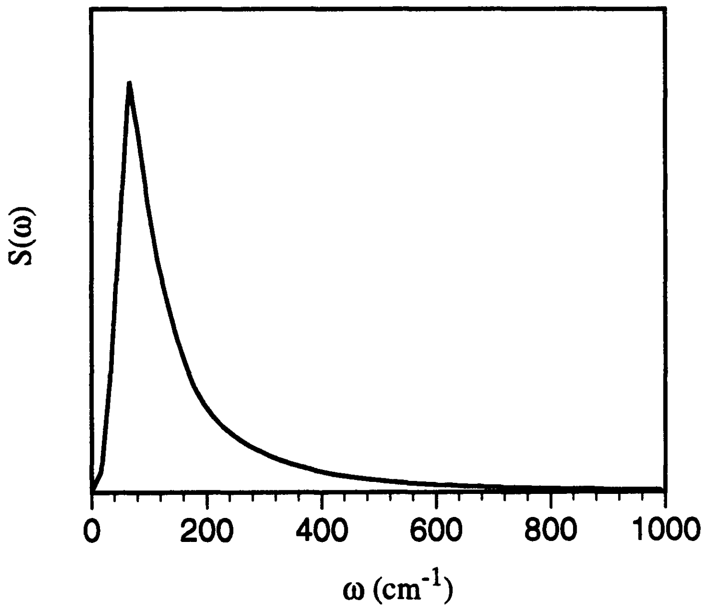

Figure 5.30 Power spectrum of the force autocorrelation function for iodine in ρ*=1.1 solution at 250K.

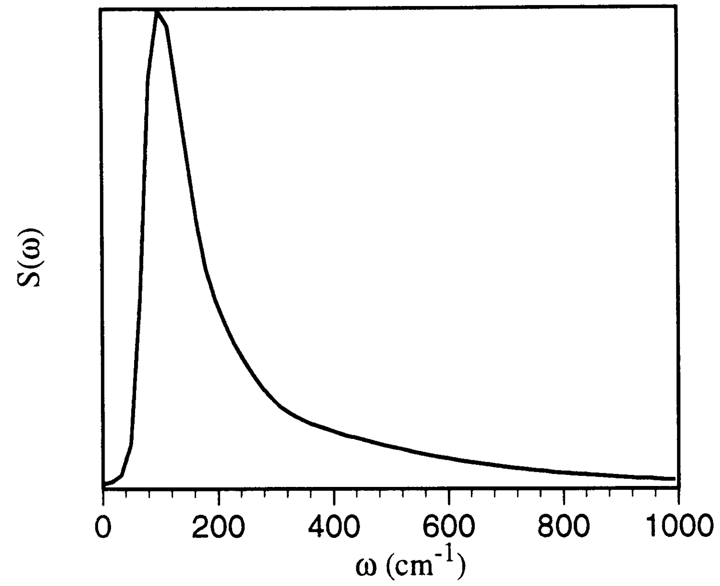

Figure 5.31 Power spectrum of the force autocorrelation function for "light iodine" in ρ*=0.9 solution at 180K.

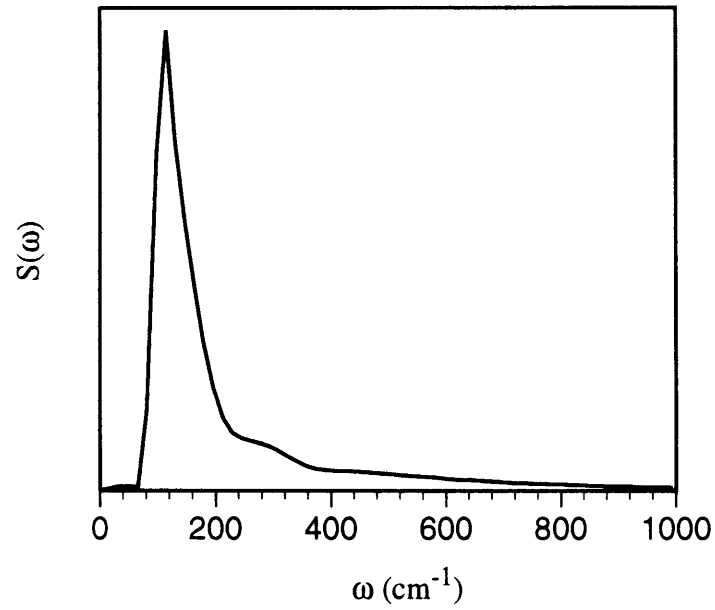

Figure 5.32 Power spectrum of the force autocorrelation function for "light iodine" in ρ*=1.1 solution at 30K.

facilitate finding ω_{max} and $\Delta\omega$ without extrapolating frequency domain data. To get a real improvement of resolution autocorrelation functions calculated to longer time are required. Table 5.4 lists the frequency value ω_{max} at maximum and the full width at half maximum (FWHM) $\Delta\omega$ of each power spectrum.

Table 5.4 ω_{max} and $\Delta\omega$ measured from the power spectrum of the force autocorrelation function

	I_2 $\rho^*=0.7$ $T\approx250K$	I_2 $\rho^*=1.1$ $T\approx250K$	I_2 $\rho^*=1.1$ $T\approx50K$	"Light I_2 " $\rho^*=0.9$ $T\approx180K$	"Light I_2 " $\rho^*=1.1$ $T\approx30K$
ω_{max} (cm^{-1})	47	69	67	102	120
$\Delta\omega$ (cm^{-1})	104	79	63	102	63

For the $\rho^*=0.7$ I_2 system, the peak frequency is below 50 cm^{-1} while the bandwidth is over 100 cm^{-1}, more than two times larger than its peak frequency. This corresponds very well to the diffusion like behavior in this system. At the other extreme, for the $\rho^*=1.1$ system with "light iodine", we have a peak frequency of 120 cm^{-1} which is almost twice as high as the bandwidth. This reflects very well the strong oscillations observed in this system. For the other three systems, the peak frequencies are all comparable to the corresponding bandwidths. On the one hand, this would be consistent with the weaker modulations observed in these systems. On the other hand, we must realize that the peak frequency and bandwidth calculated this way are only rigorous in discussing real oscillations where oscillator has a single frequency and a bandwidth caused by various broadening mechanisms. In our case the oscillation frequency itself decreases as the cage potential relaxes. The bandwidth includes both broadening effects and relaxation effects which cause the peak frequency to move towards smaller values.

It would be of interest to calculate the instantaneous frequency at any time as well as the bandwidth. This will give us a picture of how both the center frequency and the bandwidth evolve in time as the solvent cage potential relaxes. However, these instantaneous quantities can not be calculated in the same way as the time integrated quantities. They can be calculated by taking the curvature of the effective potential of the reaction coordinate for each trajectory and averaging over the ensemble. We will take another more complicated yet more general route here. As discussed in the theory section, we can have a global view of the dynamics of the solvent cage effect by diagonalizing the Hessian matrix of the whole solvent-solute system and projecting out the spectrum of the solute stretching degree of freedom. The results from the less involved approach mentioned above could be obtained through retaining only the averaged frequency for each trajectory.

We start from the two extreme cases. Fig. 5.33 presents the results for the "light iodine" in $\rho^*=1.1$ solution at $T\approx30K$. The instantaneous normal mode spectra correlate to the Fourier transform of the force autocorrelation function fairly well. Initially, the spectrum located at high frequency which is dictated mostly by the intramolecular potential. As the system moves down the potential surface its spectrum moves toward lower values and finally approaches a quasistatic value of about 100 cm^{-1} and a quasistatic bandwidth of about 60 cm^{-1}. This suggests that the "light iodine" fragments should behave very much like an oscillator after the static frequency has been reached. Fig. 5.34 presents the results for another extreme, the $\rho^*=0.7$ and $T\approx250K$ system. The spectra are dramatically different from those at the other extreme in accordance with the entirely different dynamical behavior of this system. The instantaneous spectrum quickly approaches zero. After 200 fs, the negative side (imaginary frequencies) has grown significantly indicating that a large

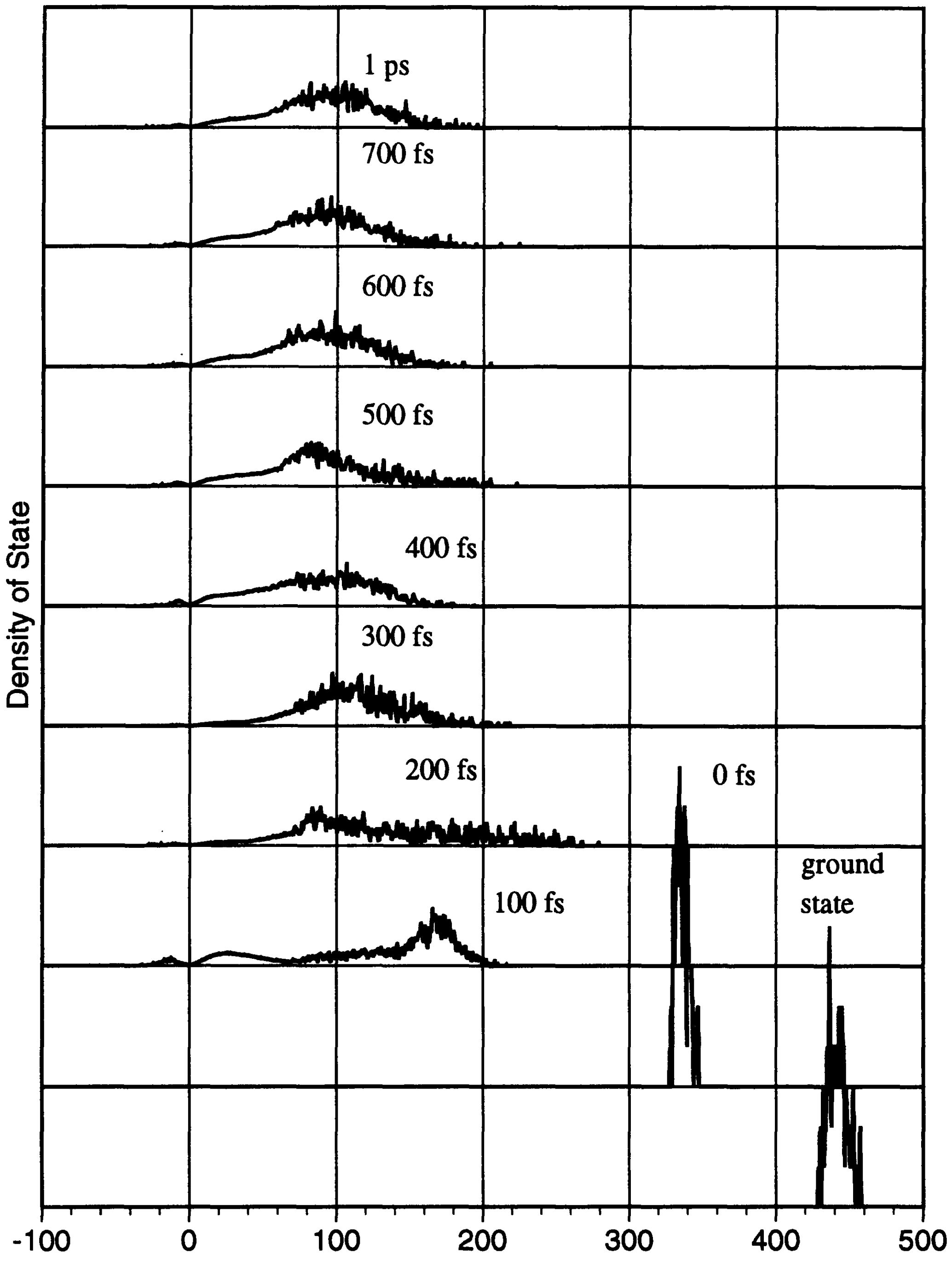

Figure 5.33 Instantaneous normal mode spectrua of the "light iodine" in $\rho^*=1.1$ solution at 30K.

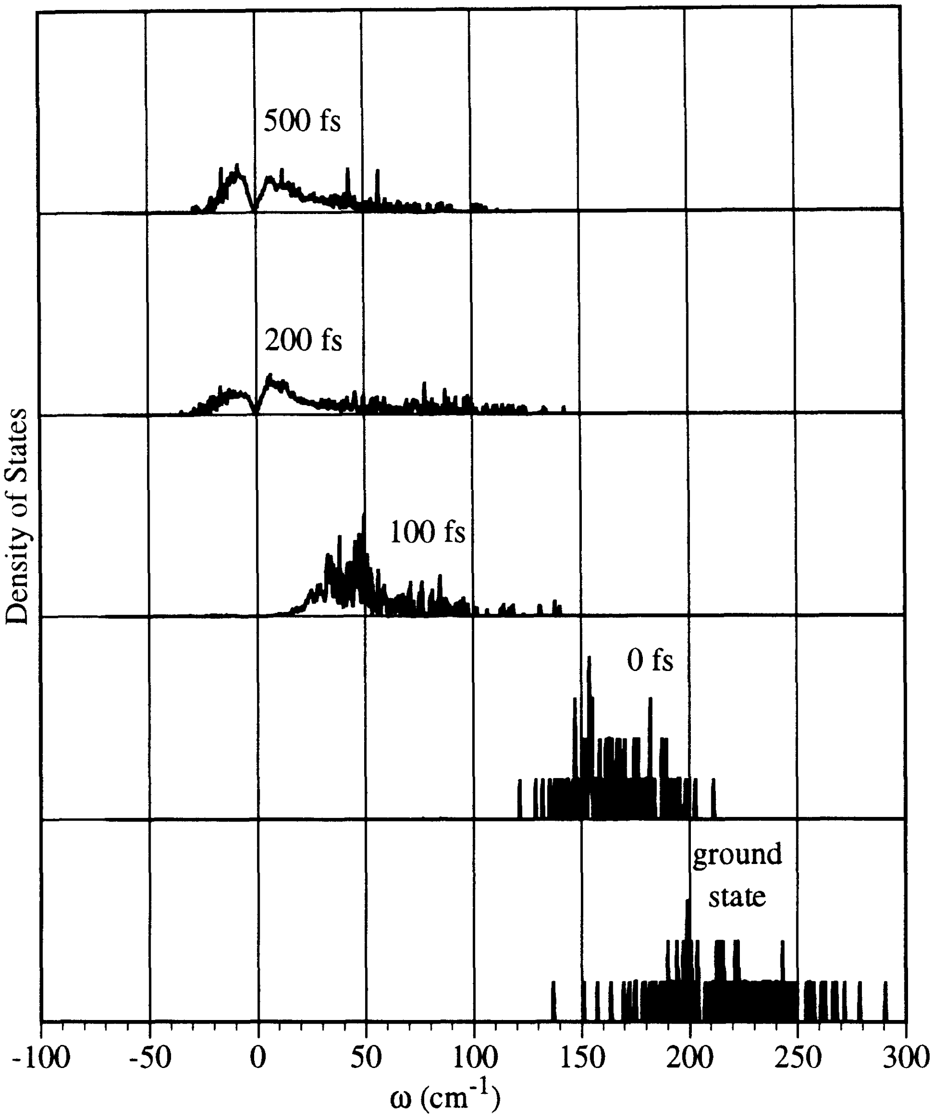

Figure 5.34 Instantaneous normal mode spectra of iodine in ρ*=0.7 solution at 250K.

fraction of the molecules are on top of a potential barrier rather than in a potential well and therefore the molecules are mostly dissociating. Comparing this to the pure liquid spectrum indicates that the two atoms from the dissociating molecule are more like two liquid atoms diffusing around rather than forming a bound pair oscillating against each other. However, it is interesting to notice that the spectral bandwidth is not as large as the bandwidth calculated from the force autocorrelation function (compare to Table 5.4). This demonstrates the previous suggestion that the bandwidth from the Fourier transform of the force autocorrelation contains both broadening effects and relaxation contributions.

Figs. 5.35 and 5.36 present the spectra of iodine in $\rho^*=1.1$ solution at 50K and 250K respectively. The spectra were similar to each other except that the bandwidth in the low temperature case is smaller. In both cases, the spectra approach quasistatic behavior at about 300 femtoseconds with a peak frequency at about 50 cm^{-1} for the high temperature solution and about 40 cm^{-1} for the low temperature solution. The widths are about 40 cm^{-1} for the low temperature solution and about 60 cm^{-1} for the high temperature solution. In both cases, there is a small negative frequency part in the spectrum indicating that a small fraction of the molecules dissociate.

Fig. 5.37 shows the results for the "light iodine" in the $\rho^*=0.9$ and $T\approx180K$ solution. The final quasistatic frequency peak around 80 cm^{-1} with a bandwidth of about 60 cm^{-1}. As expected, this is a lower peak frequency and a larger width as compared to the high density low temperature solution. The general behavior of the spectra are somewhere between the behavior found in glass solutions which could be seen in the positive part of the spectra and the behavior found in liquid with a larger negative part.

There are several general features that are worth special attention. First, if we compare the liquid spectra with those of the pure liquids, we can see that for the systems in which oscillations were observed the peak frequencies are at least comparable to those in the corresponding pure solvents. This again demonstrates that the oscillatory

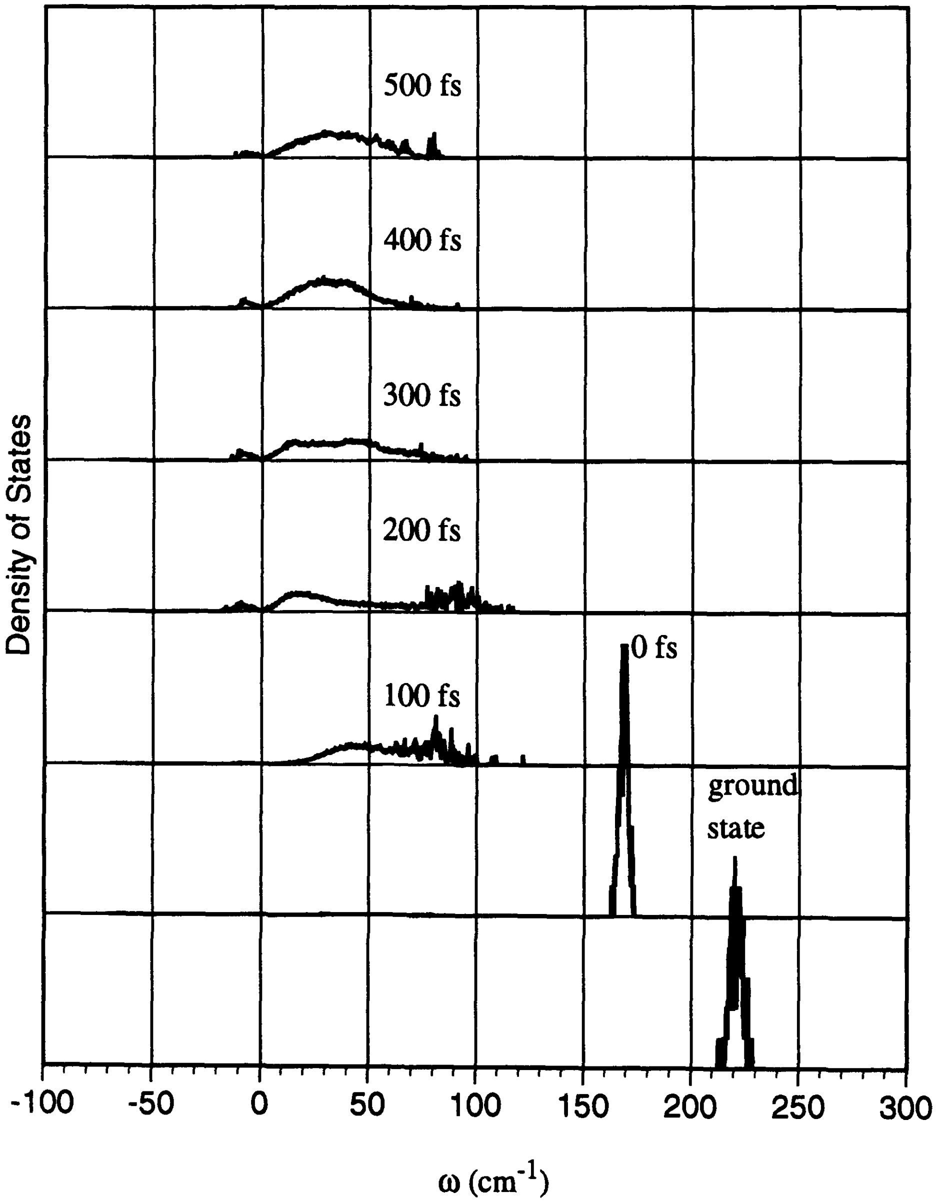

Figure 5.35 Instantaneous normal mode spectra of iodine in ρ*=1.1 solution at 50K.

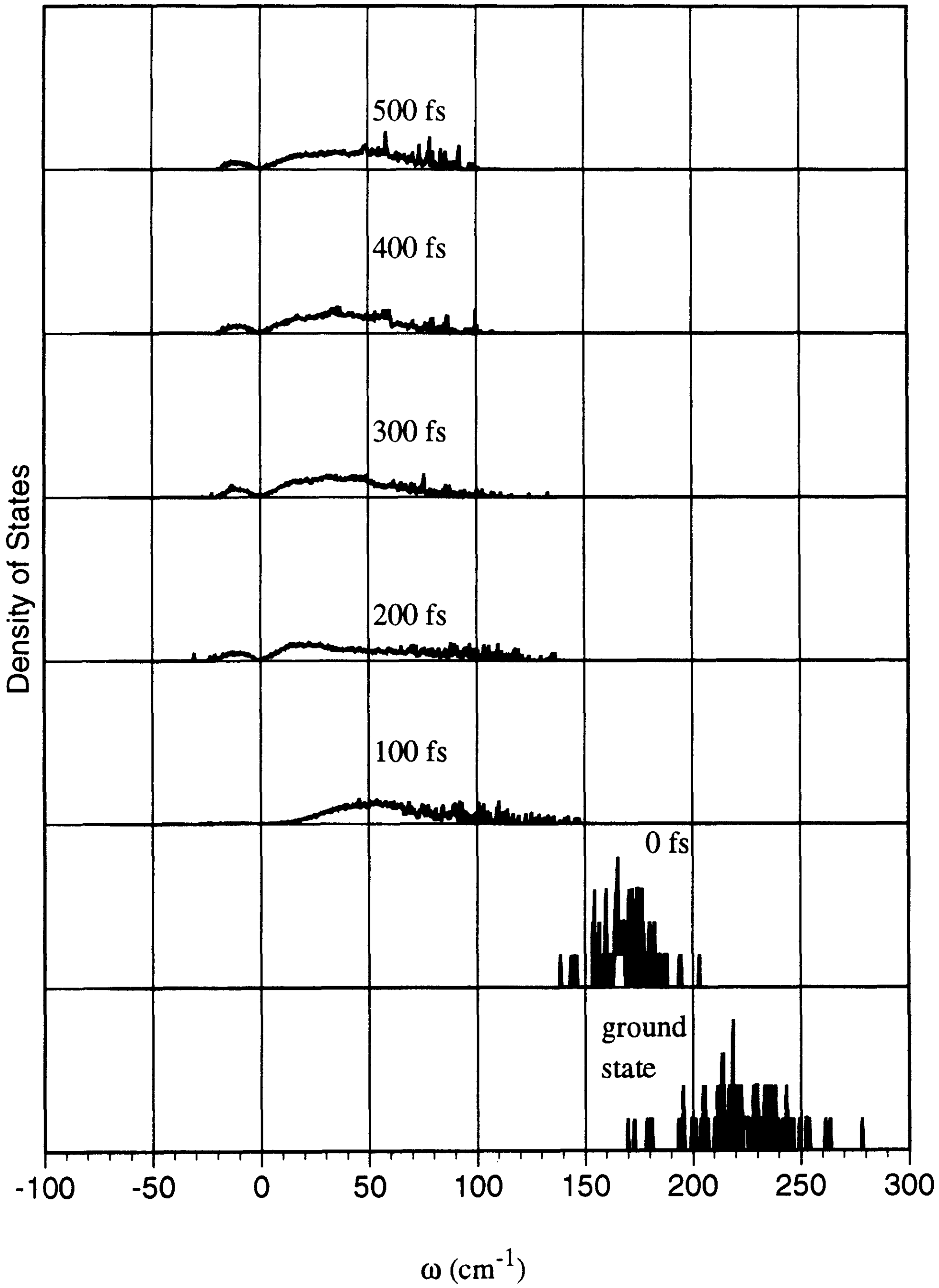

Figure 5.36 Instantaneous normal mode spectra of iodine in $\rho^*=1.1$ solution at 250K.

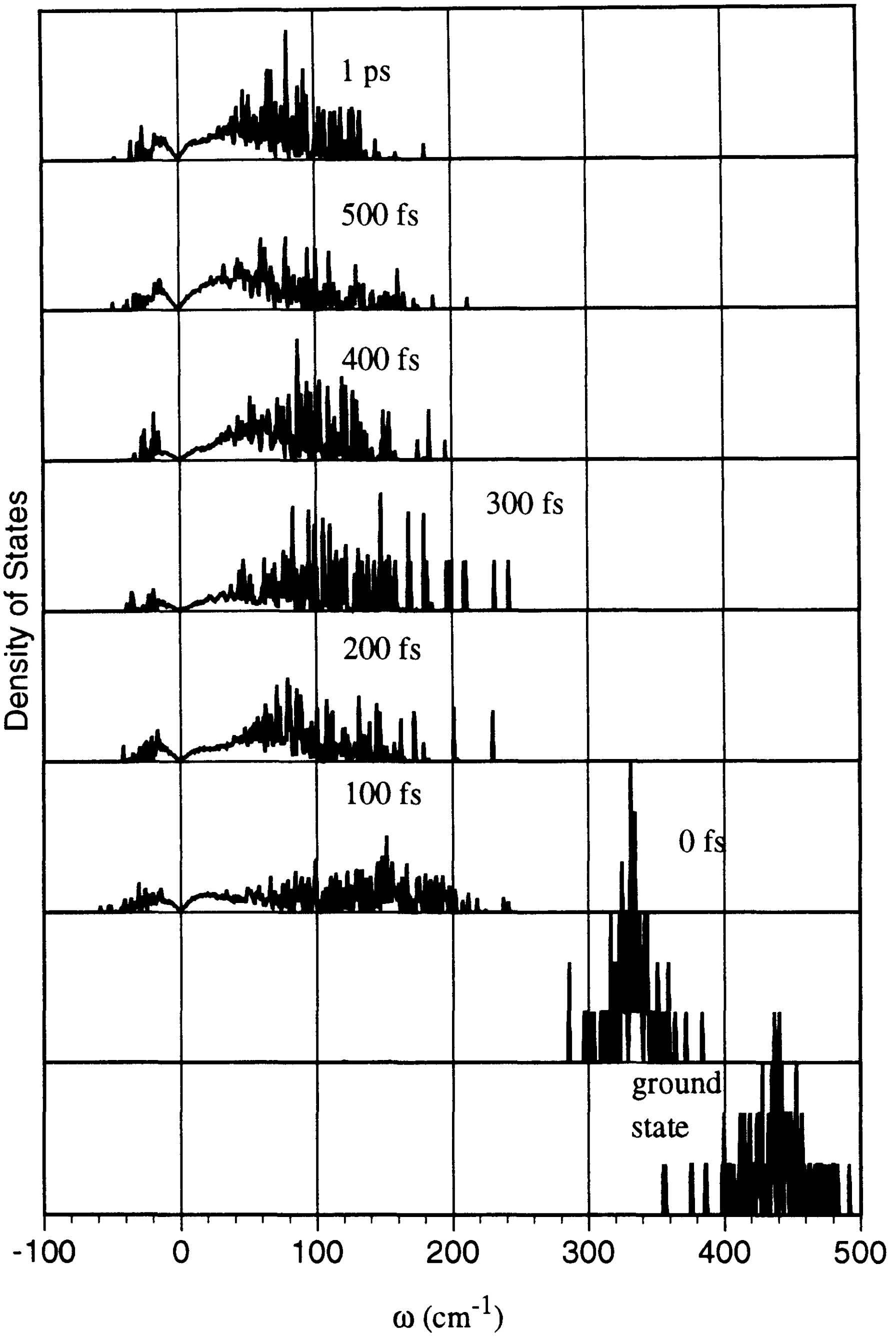

Figure 5.37 Instantaneous normal mode spectra of iodine in ρ*=0.9 solution at 180K.

behavior is a result of the faster solute motion (as evidenced by its higher frequency) than the solvent motion (as evidenced by its lower frequency). In the three iodine solutions, the reaction coordinate spectra approach the solvent spectra within about 500 femtoseconds with the low density solution the fastest. For the two high density solutions the solvent relaxation is on the same time scale as the solute motion. In the two "light iodine" solutions, on the other hand, the reaction coordinate spectra stay higher than the solvent spectra even at 1 picosecond. In these two solutions the frequencies of the reaction coordinate motion are much higher than the frequencies of the solvent bath modes. The energy transfer between them is not as efficient as in the iodine solution.

Observing these instantaneous spectra, we can see that at some intermediate times the spectra assume very complicated shapes. This is more prominent in high density situations. In the spectra of the "light iodine" in the $\rho^*=1.1$ and $T\approx30K$ solution, for example, at 100 femtoseconds we see two distinct maxima located at low and high frequencies (see Fig. 5.33). The two maxima converge into the single maximum in the static spectra at later times. Since the initial excited state spectra (i.e. at t=0) do not show splitting, this is not a result of different sites. Fig. 5.38 presents the spectra of a single configuration for the same system. It can been seen that the feature is very well represented. This suggests that the complicated shape of the spectra have a homogeneous rather than inhomogeous origin. It may indicate that the cage relaxation process involves some low frequency solvent modes. In any case, the effective potential at these intermediate times is very far from being harmonic. On the other hand, the single configuration spectra show much narrower frequency peaks as compared to the ensemble averaged spectra, suggesting that the broad frequency distributions in the ensemble averaged spectra have inhomogeneous origin. This is consistent with the speculation that different chromophores may undergo oscillations with different numbers and frequencies.

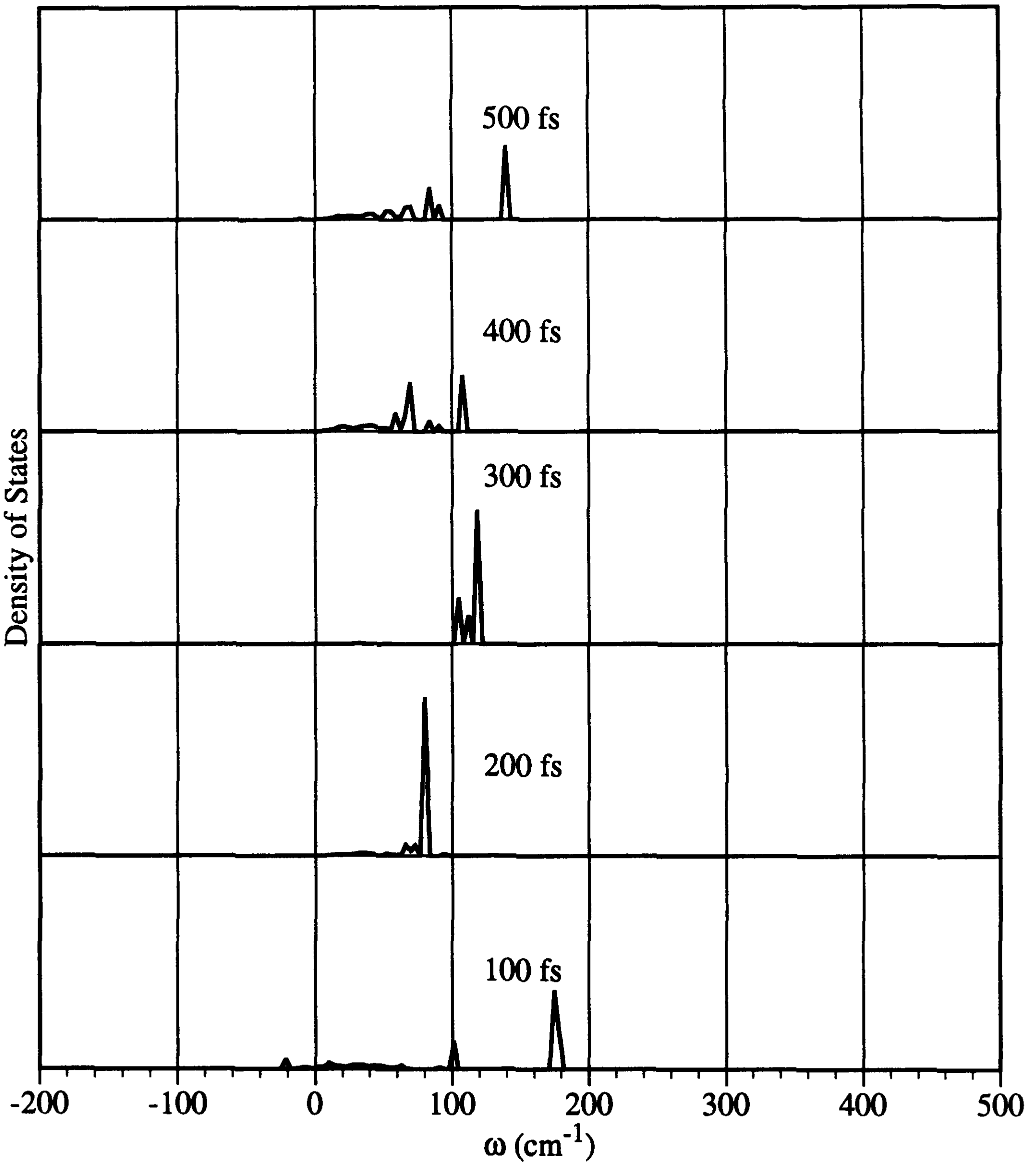

Figure 5.38 The single configuration density of states along the reaction coordinate of the "light iodine" in $\rho^*=1.1$ solution at 30K.

5.4.3 I_2 in Crystalline Solid Solution

Our results reported above included both liquid and amorphous solid solutions. It is of interest to compare with the crystalline solid solvent to see what difference an ordered environment makes. Experimental work by Apakarian and co-workers on I_2 in crystalline xenon which has shown that the caging was quite different from our results in the glass and liquid with I-I stretched to much longer distance and efficient geminate recombination into the ground state [5.73].

Figs. 5.39 and 5.40 show the results in xenon crystal. The I-I distance indeed reaches 6.0 Å, much longer than in the glass solution of the same density. The final equilibrium position for the I-I pair is around 4.2 Å, also much longer than in the glass solution. Comparing to the potential surfaces in Fig. 5.5, it is obvious that geminate recombination is facilitated. Although the experiment of Apakarian and co-workers was done on the A-state of I_2 rather than the higher repulsive state simulated here so that a direct comparison to the experiment is not appropriate, the results do indicate that the crystalline environment is very different from the glassy environment. The fast geminate recombination in this system will prevent any observation of oscillations. Nonetheless we ignore it here to permit evaluation of the dynamical behavior in the absence of curve crossing. The oscillation in this system (if it exists) has both much larger modulation and lower dephasing as compared to the glass system. These indicate a relatively weaker cage potential but greater order. Fig. 5.41 shows a picture of the atomic configuration of one representative trajectory as compared to a glass configuration at the same density (Fig. 5.42). It can be seen that the iodine molecule is actually embedded in a one-dimensional chain of xenon atoms. The longer stretching distance (which is a result of weaker cage potential) is a result of this arrangement where only the atoms in the chain have a significant contribution to the cage effect. On the other hand, this ordered cage structure guarantees the

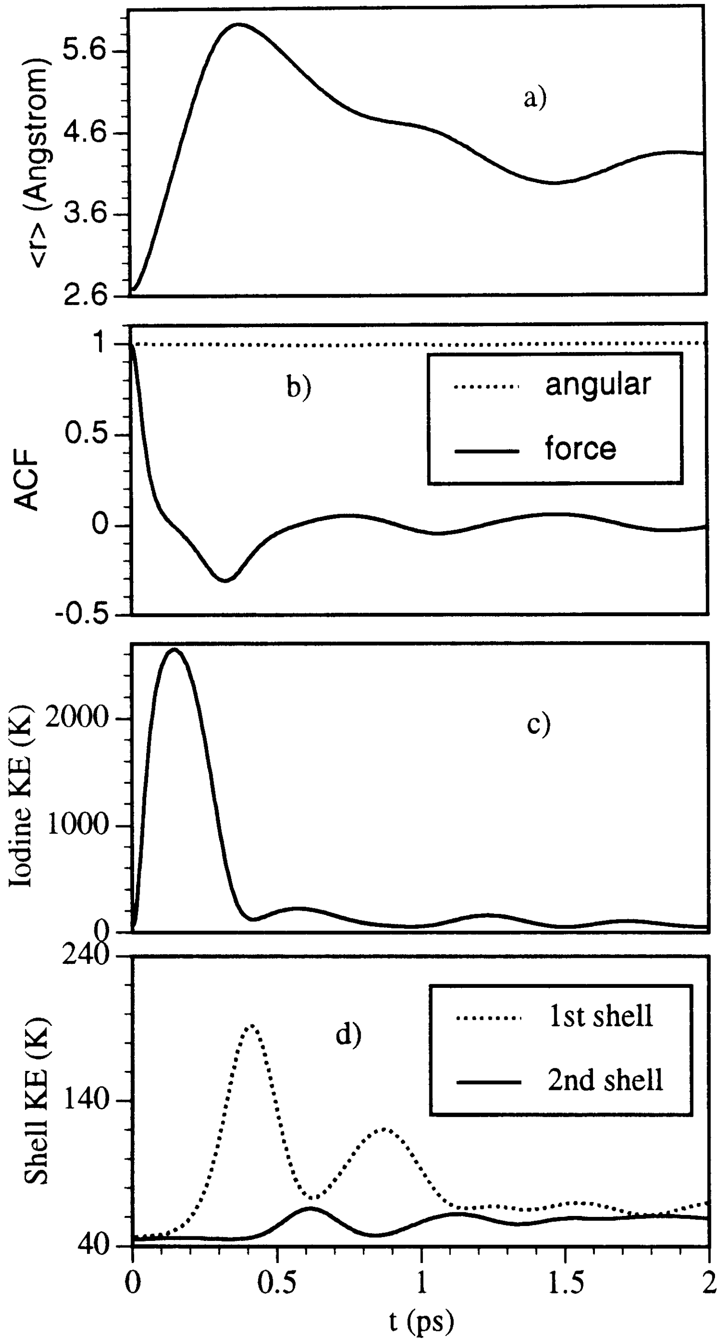

Figure 5.39 Results for I_2 in crystalline xenon solution. a) Average bond length; b) Autocorrelation Functions; c) Iodine kinetic energy; d) Solvent shell kinetic energies.

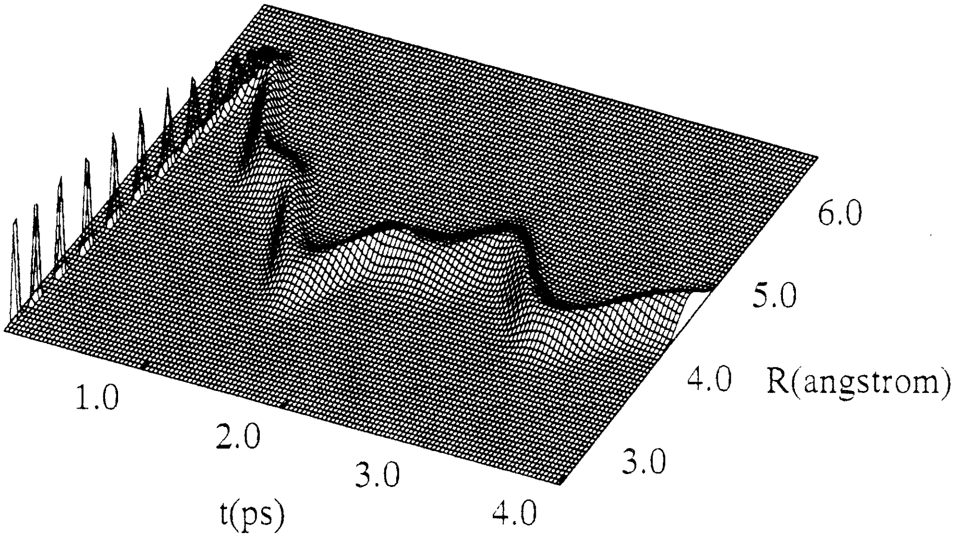

Figure 5.40 Probability distribution function of I-I distances in $\rho^*=1.1$ xenon crystalline solution at 30K.

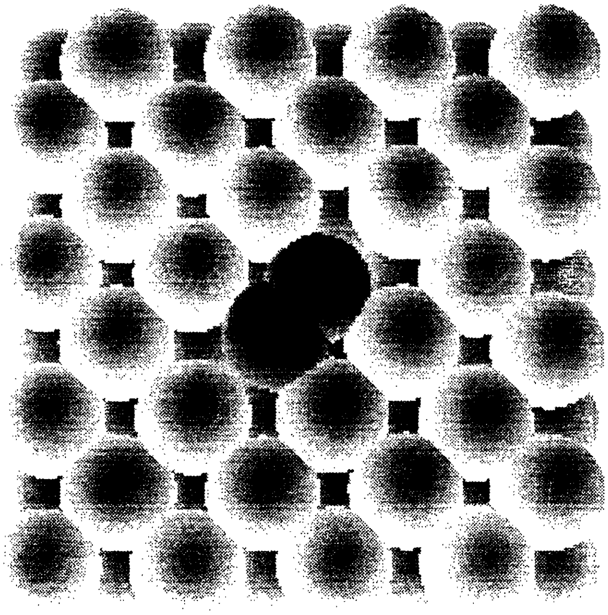

Figure 5.41 A representative picture of the packing arrangement of I_2 in $\rho^*=1.1$ crystalline xenon solution at 30K.

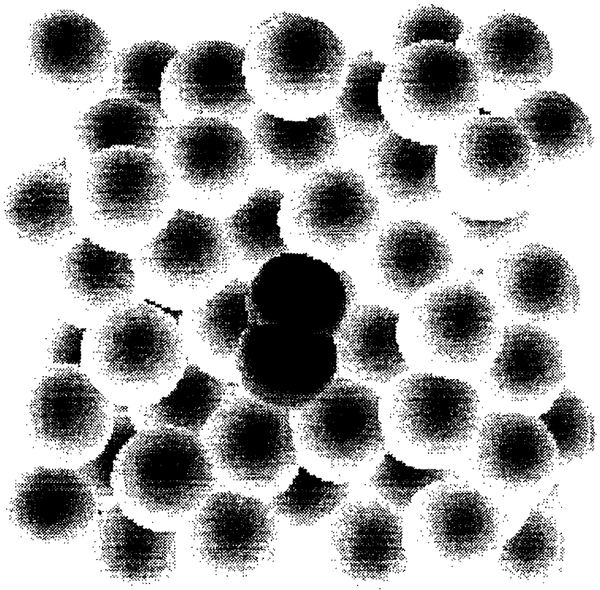

Figure 5.42 A representative picture of the packing arrangement of I_2 in $\rho^*=1.1$ amorphous xenon solution at 50K.

long lasting oscillation. Observation of the iodine and shell kinetic energy shows that energy transfer from the molecule to the solvent and among the solvent shells occurs in a coordinated fashion. Fig. 5.43 shows the Fourier transform of the force autocorrelation function and Fig. 5.44 shows the instantaneous normal mode density. As expected, the spectra are much narrower, consistent with the ordered solvent cage.

The results in the crystal solution shows that the cage effect may actually be stronger in amorphous solid solutions than in crystalline solutions. The ordered structure in the crystalline solid may not enhance the opportunity of observing cage oscillations. Even though the amorphous systems do not have structural order, if the cage is rigid enough and the efficiency of energy exchange between the solute and the solvent cage is low, cage oscillation may be expected.

5.5 FURTHER DEVELOPMENTS

We have demonstrated that coherent cage oscillations on repulsive intramolecular potential surfaces may exist if there is a separation of time scales between the molecular motion and the solvent relaxation. This type of dynamics should offer us some insight into the solvent cage effect on chemical reactions in condensed phases. Since the dissociating fragments exert a sudden force to the solvent and drive the solvent structure from an old equilibrium (with the molecule before dissociation) to a new equilibrium, it is of interest to further understand how this relaxation proceeds. We have observed interesting structure in the instantaneous normal mode densities. Further investigation of this structure should be both important and useful.

It is also interesting to extract the friction kernel $\gamma[\omega]$ from our simulations. The friction kernel will also show how the solvent cage relaxes. Kubo [5.74] has shown that

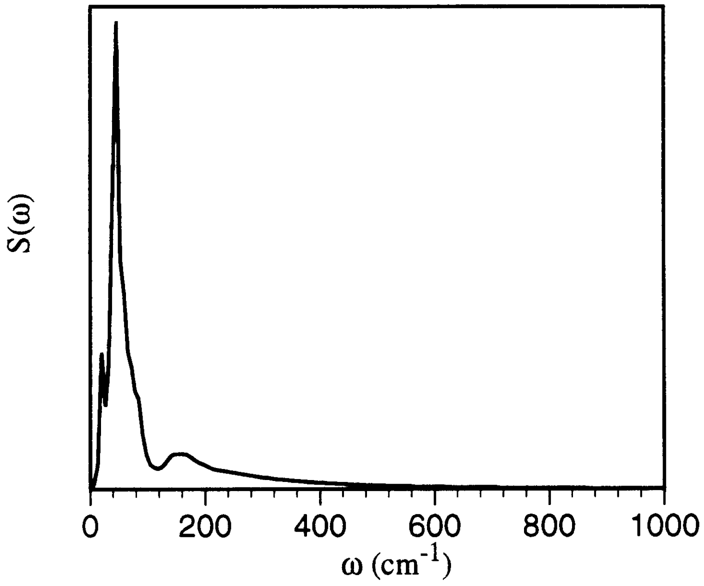

Figure 5.43 Power spectrum of the force autocorrelation function for iodine in ρ*=1.1 crystalline xenon at 30K.

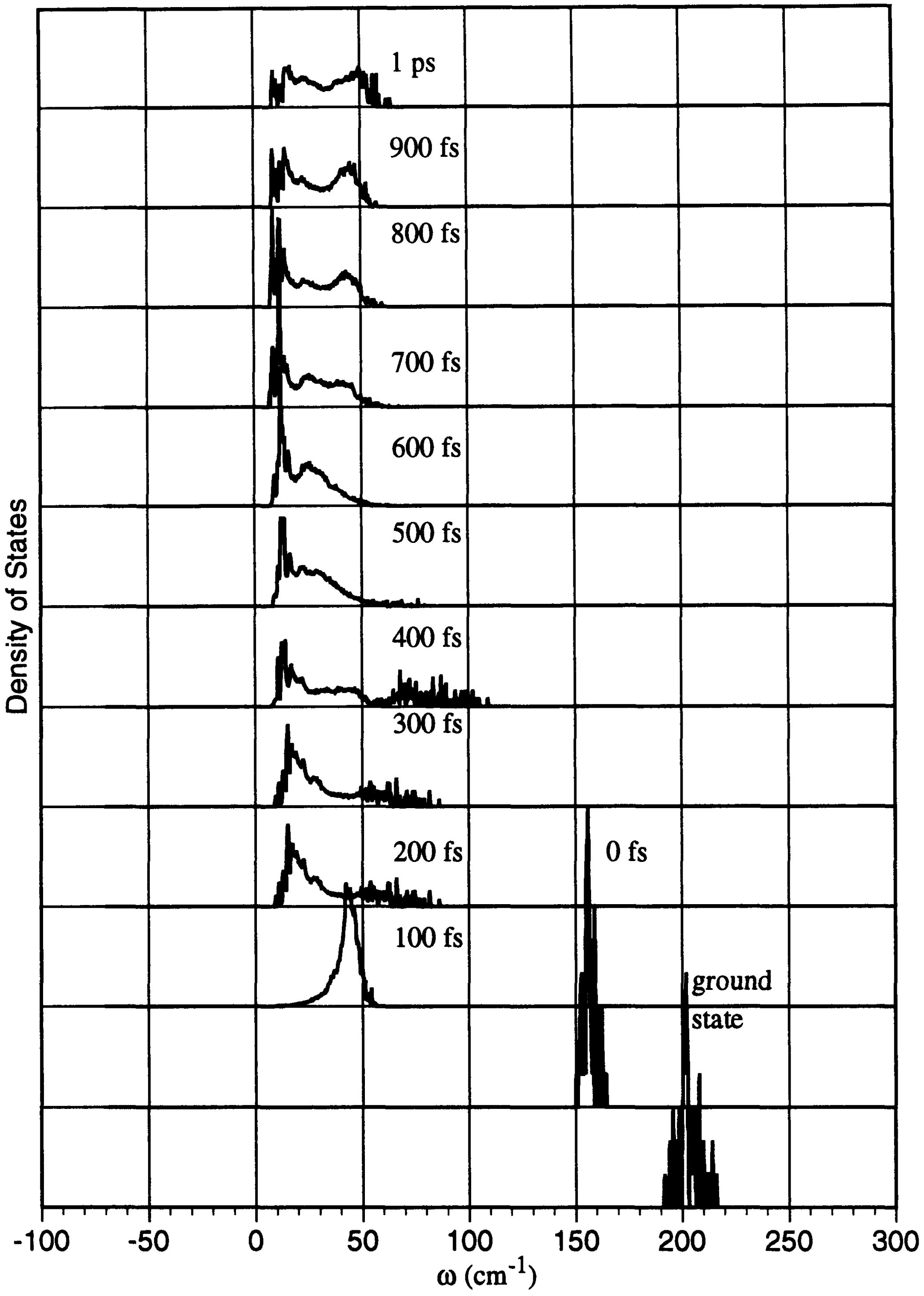

Figure 5.44 Instantaneous normal mode spectra of iodine in ρ*=1.1 crystalline xenon solution at 30K.

the friction kernel can be related to the total force autocorrelation function (after subtracting the systematic part) through a simple relation in the Fourier-Laplace space:

$$\frac{1}{\gamma[\omega]} = \frac{1}{\gamma_t[\omega]} - \frac{1}{i\omega} \tag{5.42}$$

where

$$\gamma_t[\omega] = \frac{1}{mk_BT}\int_0^\infty \langle \mathbf{F}(0)\cdot\mathbf{F}(t)\rangle e^{-i\omega t}dt \tag{5.43}$$

is the Fourier-Laplace transform of the total force autocorrelation function, and

$$\gamma[\omega] = \int_0^\infty \gamma(t)e^{-i\omega t}dt \tag{5.44}$$

is the Fourier-Laplace transform of the friction kernel.

In order to obtain **F**(t), we need to calculate the systematic part of the total force and subtract it out. This would involve calculating the total force by fixing the I-I bond length at r and averaging over time. The force so obtained is the systematic part of the total force at r. After saving this systematic force for all r, **F**(t) can be constructed by subtracting the systematic force out from the total real force, and then the friction kernel can be calculated. Since the friction kernel tells us the solvent fluctuation spectrum, it would be very interesting to compare the friction kernel calculated here to that in an equilibrium solution. This may further help us to gain insight into the dynamics of the relaxation process.

Other solute/solvent systems may also be studied with the MD methods used here. As we have mentioned I_2/xenon may not be a ideal candidate for the purpose of observing cage induced oscillations. Other molecules which have less complicated potential energy surfaces and lighter masses may be better choices. As for solvents, there are many liquids which have much stronger intermolecular interactions and therefore will form much stronger cages.

Finally, the experimental observation of cage oscillations should be another important future work. (It was the motivation of doing the MD work presented here in the first place!) It is clear now that cage oscillations are possible under favorable conditions. This should be an invitation to further experimental efforts. Of course, the choice of samples is totally open here, too.

6. SUMMARY

The reaction dynamics of solid state chemical reactions have been of both scientific and practical interests. However, due to the problem of the accumulation of reaction products in nonflowable solid samples, the conventional femtosecond spectroscopic methods employing a repetitive scheme are no longer applicable. In order to extend the femtosecond spectroscopy into this and other new areas where irreversible changes in a sample can not be conveniently removed, we have initiated the development of new femtosecond spectroscopic methods which can record a time-dependent signal in a single shot. In the first method, the multiple probe method, the probe beam is divided into 16 equal intensity parts. These 16 pulses are used to monitor the sample response to an excitation pulse. Since the relative delays among these 16 pulses are known, 16 points along the time axis can be sampled after a single excitation pulse. The method has been demonstrated in malachite green with a pump-probe configuration and in CS_2 with an optical Kerr effect configuration. In the second method, the spatial encoding method, the pump and probe beams are focused into to lines and crossed with each other in the sample at a substantial angle. Different parts of the probe beam along the line reach the sample at different delay times. The time-dependent response of the sample is carried by the probe spatial intensity profile. By spatially resolving the intensity of the probe beam, the time-dependent signal can be recovered with a single pair of pump and probe pulses.

The spatial encoding single-shot method has been applied to study the reaction dynamics of a molecular crystal : the crystal of 2,5-distyrylpyrazine (DSP). This is the first femtosecond spectroscopic study of a solid state chemical reaction. The reaction is an excited state four-center addition type of reaction in which a DSP molecule is excited by a 400 nm photon to its first excited state where it opens a double bond in one or both of the styryl moiety and forms a four center ring with another DSP molecule. The reactivity of DSP is enhanced significantly in one of its crystalline phase: the α-phase. It was suggested that both the lattice structure and an n-π* electronic transition of the DSP molecule helped to enhance the reaction rate. However, our preliminary results showed a short time signal similar to that in liquid solutions. This may suggest that the photoexcitation prepares the DSP molecule at a location on its reactive excited state potential energy surface below the transition state energy barrier. Further experiments including a pump intensity dependence study are called for to fully understand the roles the crystal lattice and other electronic states play in this reaction.

Molecular dynamics simulations have been performed to study the solvent cage effect on photodissociation in liquid and solid solutions. The purpose of this study is to evaluate the possibility of observing coherent oscillatory motions of photodissociated fragments on an intramolecular repulsive potential energy surface due to the confining forces of solvent cages. We have used simple diatomic molecules in liquid or solid xenon solutions as our model systems. The results demonstrate that this type of oscillations can be observed in both amorphous solid and liquid solutions. The oscillations are due to a separation of time scales between the motion of the reactants along the reaction coordinate and the relaxation of the solvent environment as well as the inefficient exchange of energy between the reactants and their solvent surroundings. The slower the solvent relaxation as compared to the motion of the reactants and the lower the energy exchange efficiency, the more prominent the oscillations. An instantaneous normal mode analysis has been performed on these systems. The results of this analysis have provided more detailed information about the nature of these oscillations.

7. APPENDIX

7.1. TANGENTIAL PHASE-MATCHING

Effective nonlinear wave generation requires phase matching between the input fundamental waves and the generated wave. The phase-matching condition for mixing two waves is:

$$\mathbf{k}_1 + \mathbf{k}_2 = \mathbf{k}_3 \qquad (7.1)$$

Geometrically, this means that the **k**-vector surface of $\mathbf{k}_1 + \mathbf{k}_2$ intersects $\mathbf{k}_3$ surface. When $\mathbf{k}_1 + \mathbf{k}_2$ surface and $\mathbf{k}_3$ surface are tangential, we have tangential phase-matching(TPM). Tangential phase-matching was developed twenty years ago for up-converting IR images, because under TPM

$$|\Delta k| \propto \Delta\theta^2 \qquad (7.2)$$

which allows a large field of view being up-converted by a single pump beam (see Fig. 7.1.).

It is possible to use this technique to mix two waves in the visible or near IR. This

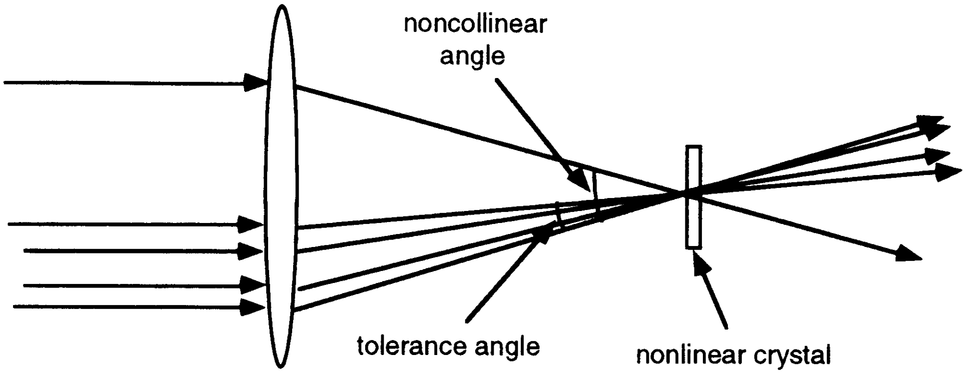

Figure 7.1. Schematic illustration of upconverting many beams by a single beam.

will allow us to directly mix our 16 beams with a single 'pump' beam and generate 16 second harmonics or sum-frequencies. Since we can take the cross section of 16 beams as a single large beam, the question becomes to find how big the diameter of this 'large beam' could be for phase-matching. More precisely, we need to know how big an acceptance angle we can achieve.

For our application, we will need type I phase-matching in both 2nd harmonic generation and sum-frequency generation to avoid dispersion between the pump and probe pulses. However, both type I and type II phase-matching are possible for TPM. We will consider the more general case here without limiting to type I phase-matching.

Assume $\mathbf{k}_1$ is the wave vector of the single 'pump' beam. $\mathbf{k}_2$ is the wave vector of the other input wave to which we want to give a large acceptance angle. $\mathbf{k}_3$ is the wave vector of the generated wave.

$$\text{o}-\text{ray:}\quad k=\frac{2\pi}{\lambda}n_o(\lambda) \tag{7.3}$$

$$\text{e}-\text{ray:}\quad k(\theta)=\frac{2\pi}{\lambda}n_e(\lambda,\theta) \tag{7.4}$$

and

$$\frac{1}{n_e^2(\lambda,\theta)} = \frac{\cos^2(\theta)}{n_o^2(\lambda)} + \frac{\sin^2(\theta)}{n_e^2(\lambda)} \tag{7.5}$$

where n_e and n_o are refractive indices for e-ray and o-ray, respectively. Fig. 7.2 and Fig. 7.3 show the relations among the three **k** vectors for both tangential phase matching and the usual phase matching.

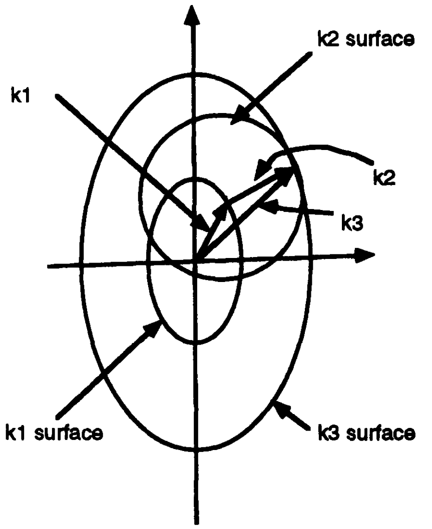

k-vector diagram illustate type II tangential phase-matching with k1 as e-ray, k2 as o-ray

Figure 7.2. **k** vector diagram for tangential phase matching.

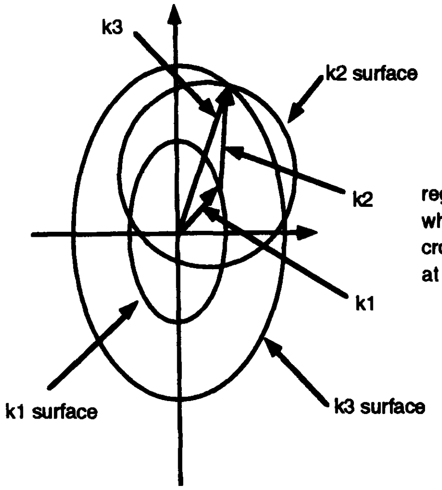

regular phase-matching where k1+k2 surface cross with k3 surface at one point

Figure 7.3. **k** vector diagram for non tangential phase matching.

We will choose $\mathbf{k}_1$ as o-ray for type I phase-matching or e-ray for type II phase-matching. $\mathbf{k}_2$ will always be o-ray, and $\mathbf{k}_3$ will be e-ray. The wavelengths of the three waves are related by,

$$\frac{1}{\lambda_3} = \frac{1}{\lambda_1} + \frac{1}{\lambda_2} \tag{7.6}$$

Since there is not a closed form solution for shorter wavelength input waves (closed form solutions for up-converting IR exploited approximations which are no longer valid if λ_2 is not big), we will solve the problem numerically.

Define

$$f^2(\theta_1, \theta_3) = k_1^2(\theta_1) + k_3^2(\theta_3) - 2 \cdot k_1(\theta_1) \cdot k_3(\theta_3) \cdot \cos(\theta_3 - \theta_1) \tag{7.7}$$

tangential phase-matching requires f to be a minimum concerning θ_3. Then the criterion for tpm for a pair of input wavelengths is whether there is a θ_1^{tp} which will satisfy

$$f(\theta_1^{tp}, \theta_3^{tp}) = k_2 \tag{7.8}$$

where θ_1^{tp} is the tangential phase-matching angle. The tangentially phase-matched noncollinear angle α^{tp} is given by

$$\cos(\pi - \alpha^{tp}) = \frac{k_1^2(\theta_1^{tp}) + k_2^2 - k_3^2(\theta_3^{tp})}{2k_1(\theta_1^{tp}) \cdot k_2} \tag{7.9}$$

The phase mismatch is given by

$$|\Delta k| = k_3(\alpha) - k_1 \cdot \cos(\theta_3 - \theta_1^{tp}) - k_2 \cdot \cos[\alpha - (\theta_3 - \theta_1^{tp})] \tag{7.10}$$

and the relative conversion efficiency is

$$\eta = \frac{1}{L^2} \left\{ \frac{\sin\left(\frac{1}{2}|\Delta k| \cdot L\right)}{\frac{1}{2}|\Delta k|} \right\}^2 \tag{7.11}$$

where L is the length of the nonlinear crystal.

The following are the calculated results for a 0.3 mm thick BBO. For type I doubling of 620 nm, we have phase-matching angle θ_1^{tp}=36.31°, and the phase-matched noncollinear angle α^{tp}=9.21°. For type I doubling of 800nm, we have θ_1^{tp}=27.05° and α^{tp}=7.99°. Fig. 7.4 presents the relative doubling efficiency verse noncollinear angle α^{tp}. Also presented in Fig. 7.4 is the relative doubling efficiency for a 1mm tick BBO. The angular tolarence is significantly lower.

Figure 7.5 shows the possible wavelength range of type I sum frequency generation with 620 nm light using a 0.3 mm thick BBO crystal.

The advantages of using nonlinear up-conversion are as following:

(1) Allowing using different probe wavelengths in the experiment: We can use 16 beams of one wavelength to analyze a longer probe pulse of a different wavelength. It is no longer necessary to use a different set of beamsplitters for each probe wavelength.

(2) Angular deviation of the 16 beams can be corrected theoretically. It is also possible to collimate the cross section small enough that angular deviation is no longer important (Fig. 7.6).

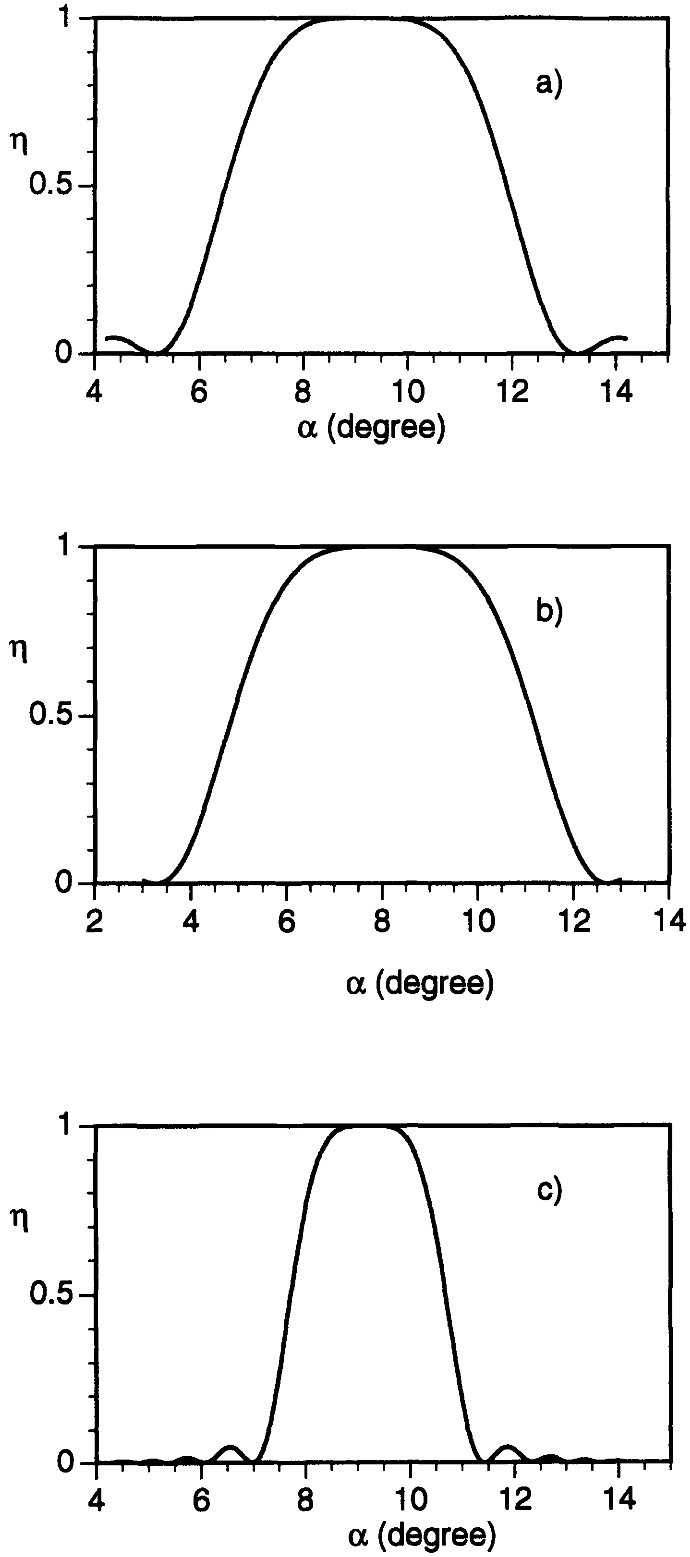

Figure A1.4. Relative doubling efficiency in BBO vs. noncollinear angle. a) λ=620nm, L=0.3mm; b) λ=800nm, L=0.3mm; c) λ=620, L=1mm.

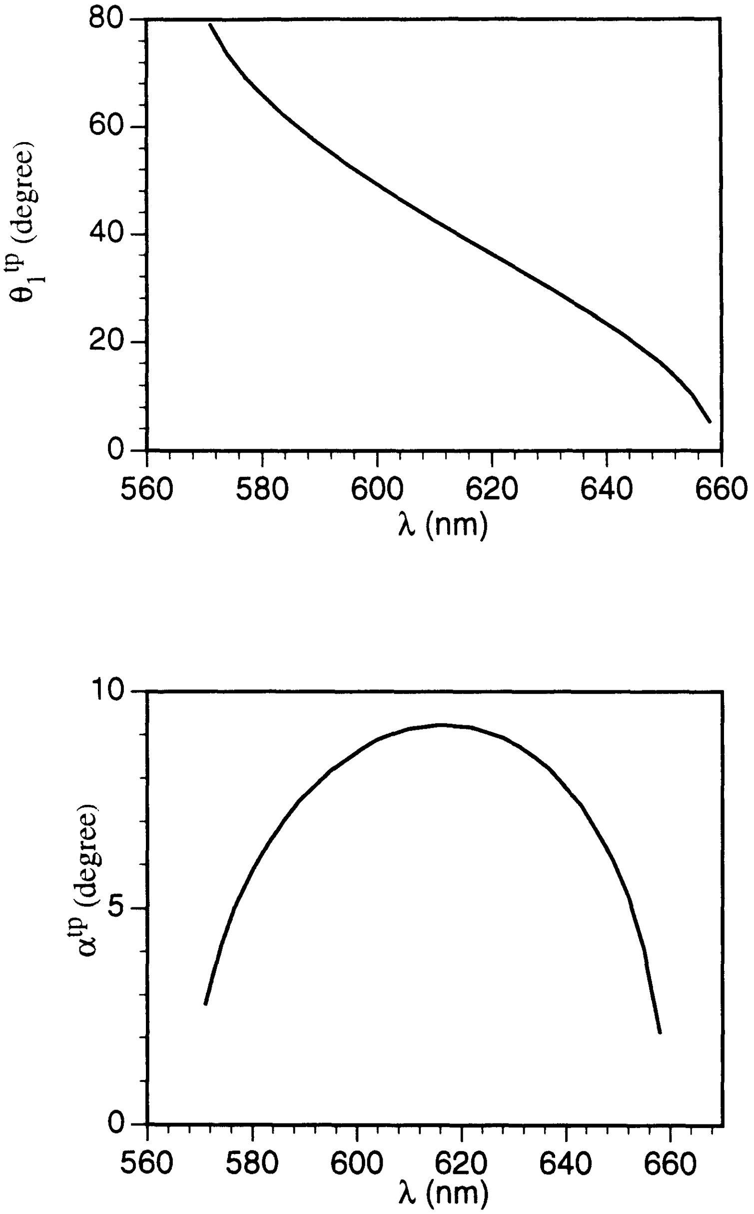

Figure A1.5. Phase-matching angle and phase-matched noncollinear angle for type I sum frequency generation of different wavelength λ with λ=620nm in 0.3mm BBO

(3) Taking advantage of nonlinear process: the power of the generated wave scales up with the power of the 16 beams. The long probe pulse could be kept weak.

(4) Allowing background free detection.

(5) Allowing more precise timing determination.

(6) In practice, we no longer need to align 16 beams every time we switch samples. Both the crystal and the 16 beams will be fixed after aligned. Only the long probe beam needs to be realigned.

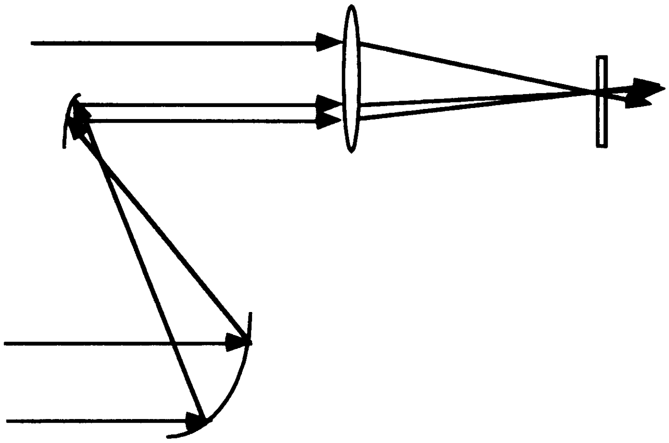

Figure 7.6. The cross section of the 16 beam grid can be collimated down.

REFERENCES

CHAPTER 1

1.1. See articles in the Journal of Physical Chemistry, Vol. 97 no. 48, 1993.

1.2. See for example L. Dhar, J. A. Rogers, and K. A. Nelson, *Chem. Rev.* **94**, 157(1994).

1.3. A. Rahman, *J. Chem. Phys.* **45**, 2585(1966).

1.4. R. M. Lynden-Bell, D. J. C. Hutchinson, and M. J. Doyle, *Mol. Phys.* **58**, 307(1986).

1.5. S. Ruhamn, A. G. Joly, B. Kohler, L. R. Williams, and K. A. Nelson, *Revue Phys. Appl.* **22**, 1717(1987).

1.6. B. Kohler and K. A. Nelson, *J. Phys. Chem.* **96**, 6532(1992).

CHAPTER 2

2.1. P. F. Moulton, *J. Opt. Soc. Am.* **B3**, 125(1986).

2.2. D. E. Spence, *Opt. Lett.* **16**, 42(1991).

2.3. H. A. Haus, *IEEE J. Quant. Electr.* **28**, 2086(1992).

2.4. C.-P. Huang, H. C. Kapteyn, J. W. McIntosh, and M. M. Murnane, *Opt. Lett.* **17**, 139(1992).

2.5. C.-P. Huang, M. T. Asaki, S. Backus, M. M. Murnane, and H. C. Kapteyn, *Opt. Lett.* **17**, 1289(1992).

2.6. M. T. Asaki, C.-P. Huang, D. Garvey, J. Zhou, H. C. Kapteyn, and M. M. Murnane, *Opt. Lett.* **18**, 977(1993).

2.7. D. Strickland and G. Mourou, *Opt. Comm.* **56**, 219(1985).

2.8. F. Salin, J. Squier, G. Mourou, and G. Vaillancourt, *Opt. Lett.* **16**, 1964(1993).

2.9. J. V. Rudd, G. Korn, S. Kane, J. Squier, G. Mourou, and P. Bado, *Opt. Lett.* **18**, 2044(1993).

2.10. O. E. Martinez, *IEEE J. Quant. Electr.* **23**, 59(1992).

2.11. F. Salin, J. Squier, and G. Mourou, *Appl. Opt.* **31**, 1225(1992).

2.12. D. J. Kane and R. Trebino, IEEE J. Quant. Electron.,

2.13. M. V. Oritz, J. H. Fair, and D. J. Kulzenga, in OSA Proceedings on the Advanced Solid-State Lasers, Vol. 13, eds. L. L. Chase and A. A. Pinto, 1992. p.361.

2.14. J. E. Geusic, H. J. Levinstein, S. Singh, R. G. Smith, and L. G. Van Ultert, *IEEE J. Quant. Electr.* **4**, 352(1968)

2.15. Y. S. Liu, D. Dentz, and R. Belt, *Opt. Lett.* **9**, 76(1984).

2.16. P. E. Perkins and T. S. Fahlen, *J. Opt. Soc. Am.* **B4**, 1066(1987).

2.17. T. P. Dougherty, G. P. Wiedderecht, and K. A. Nelson, *Science* **258**, 770(1992).

2.18. R. Szipocs, K. Ferencz, C. Spielmann, and F. Krausz, *Opt. Lett.* **19**, 201(1994).

2.19. A. Stingl, C. Spielmann, F. Krausz, and R. Szipocs, *Opt. Lett.* **19**, 204(1994).

2.20. M. Ramaswamy, M. Ulman, J. Paye, and J. G. Fujimoto, *Opt. Lett.* **18**, 1822(1993).

2.21. M. S. Pshenichnikov, W. P. de Boeij, and D. A. Wiersma, *Opt. Lett.* **19**, 572(1994).

2.22. J. Zhou, C.-P. Huang, C. Shi, M. M. Murnane, and K. C. Kapteyn, *Opt. Lett.* **19**, 126(1994).

2.23. C. P. Barty, C. L. Gordon III, and B. E. Lemoff, *Opt. Lett.* **19**, 1442(1994).

CHAPTER 3

3.1. E. P. Ippen and C. V. Shank, in Ultrafast Light Pulses, ed. S. L. Shapiro (Springer, New York, 1977) p. 83.

3.2. W. Wang, L. Dhar, J. Fourkas, K. A. Nelson, L. Xiao, and D. F. Coker, in *Femtosecond Reaction Dynamics*, D. A. Wiersma(ed.), North-Holland, Amsterdam, 1994. pp.111-123.

3.3. W. Wang, M. M. Wefers, and K. A. Nelson, in *Structure and Properties of Energetic Materials*, D. H. Liebenberg, *et al.*(eds.), Materials Research Society, Pittsburgh, Pennsylvania, 1993. pp.129-40.

3.4. G. P. Wiederrecht, W. Wang, K. A. Nelson, A. M. Weiner, D. E. Leaird, in *Ultrafast Phenomena VIII*, edited by J. L. Martin, A. Migus, G. A. Mourou, and A. H. Zewail, Springer-Verlag, Berlin, 1992. pp.110-12.

3.5. Z. Vardeny and J. Tauc, *Opt. Comm.* **39**, 396(1981).

3.6. L. Dhar, J. T. Fourkas, and K. A. Nelson, *Opt. Lett.* **19**, 643(1994).

3.7. Ph. Emplit, J.-P. Hamaide, and F. Reynaud, *Opt. Lett.* **17**, 1358(1992).

3.8. J. Janszky, G. Corrdi, and R. N. Gyuzalian, *Opt. Comm.* **23**, 293(1977).

3.9. F. Salin, P. Georges, G. Roger, and A. Brun, *Appl. Opt.* **26**, 4528(1987).

3.10. A. Brun, P.Georges, G. Le Saux, and F. Salin, *J. Phys. D: Appl. Phys.* **24**, 1225(1991)

CHAPTER 4

4.1. P. N. Prasad, in Organic Solid State Chemistry, ed. by G. R. Desiraju (Elsevier, Amsterdam, 1987). p.117.

4.2. G. Wegner, *Pure and Appl. Chem.* **49**, 443(1977).

4.3. M. Hasegawa and Y. Hashimoto, *Mol. Cryst. Liq. Cryst.* **219**, 1(1992).

4.4. N. F. Scherer, L. R. Khundkar, R. B. Bernstein, and A. H. Zewail, *J. Chem. Phys.* **87**, 1451(1987).

4.5. N. F. Scherer, C. Sipes, R. B. Bernstein, and A. H. Zewail, *J. Chem. Phys.* **92**, 5239(1990).

4.6. M. Gruebele, I. R. Sims, E. D. Potter, and A. H. Zewail, *J. Chem. Phys.* **95**, 7763(1991).

4.7. I. R. Sims, M. Gruebele, E. D. Potter, and A. H. Zewail, *J. Chem. Phys.* **97**, 4127(1992).

4.8. R. Franke, *Chem. Ber.*, 38, 3727(1905).

4.9. C. F. Keolsch and W. H. Gumprecht, *J. Org. Chem.* **23**, 1603(1958).

4.10. M. Hasegawa, Y. Suzuki, F. Suzuki, and H. Nakanishi, *J. Polym. Sci. pt. A-1* **7**, 743(1969);

4.11. H. Nakanishi, Y. Suzuki, F. Suzuki, and M. Hasegawa, *ibid* **7**, 753(1969).

4.12. M. Hasegawa, Y. Suzuki, and T. Tamaki, *Bull. Chem. Soc. Jpn.* 43, 3020(1970).

4.13. E.-Z. M. Ebeid, M. H. Abdel-Kader, and S. E. Morsi, *J. Chem. Soc. Faraday Trans. 1* **78**, 3213(1981).

4.14. E.-Z. M. Ebeid and S. E. Morsi, *J. Chem. Soc. Faraday Trans. 1* **79**, 1183(1982)

4.15. E.-Z. M. Ebeid and N. J. Bridge, *J. Chem. Soc. Faraday Trans. 1* **80**, 1113(1983).

4.16. N. M. Peachey and C. J. Eckhardt, *Chem. Phys. Lett.* **188**, 462(1992).

4.17. N. M. Peachey and C. J. Eckhardt, *J. Amer. Chem. Soc.* **115**, 3519(1993).

4.18. N. M. Peachey and C. J. Eckhardt, *J. Phys. Chem.* **97**, 10849(1993).

4.19. J. O. Williams and K. Janecka-Styrcz, *Chem. Phys. Lett.* **69**, 83(1980)

4.20.J. Swlatkiewicz, G. Eisenhardt, P. N. Prasad, J. M. Thomas, W. Jones, and C. R. Theocharis, *J. Phys. Chem.* **86**, 1764(1982).

4.21. M. D. Cohen and G. M. Schmidt, *J. Chem. Soc.* **1964**, 1996.

4.22. G. M. Schmidt, *J. Chem. Soc.* **1964**, 2014.

4.23. J. Bregman, K. Osaki, G. M. Schmidt, and F. I. Sonntag, *J. Chem. Soc.* **1964**, 2021.

4.24. Y. Sasada, H. Shimanouchi, H. Nakanishi, and M. Hasegawa, *Bull. Chem. Soc. Jpn.* **44**, 1262(1971).

4.25. H. Nakanishi and K. Ueno, *Acta Cryst.* **B32**, 3352(1976).

4.26. H. Nakanishi, G. M. Parkinson, W. Jones, J. M. Thomas, and M. Hasegawa, *Isr. J. Chem.* **18**, 261(1979).

4.27. M. Hasegawa, in Advances in Polymer Science, Volume 42, Springer-Verlag Berlin, Heidelberg, 1982. p.1.

4.28. M. A. El-Sayed and W. R. Moomaw, in *Excitons, Magnons and Phonons in Molecular Crystals*, ed. A. B. Zahlan, Cambridge Press, 1968. p.103.

4.29. D. P. Craig, R. Mason, P. Pauling, and D. P. Santry, *Proc. Roy. Soc. A* **286**, 98(1965).

4.30. R. M. Hochstrasser and P. N. Prasad, *J. Chem. Phys.* **56**, 2814(1972).

CHAPTER 5

5.1. J. Frank and E. Rabinowitsch, *Trans. Faraday Soc.* **30**, 120(1934).

5.2. E. Rabinowitch and W. C. Wood, *Trans. Faraday Soc.* **32**, 1381(1936).

5.3. V. E. Bondybey and L. E. Brus, *J. Chem. Phys.* **62**, 620(1975).

5.4. V. E. Bondybey and C. Fletcher, *J. Chem. Phys.* **64**, 3615(1976).

5.5. L. E. Brus and V. E. Bondybey, *J. Chem. Phys.* **65**, 71(1976).

5.6. T. J. Chuang, G. W. Hoffman, and K. B. Eisenthal, *Chem. Phys. Lett.* **25**, 201(1974).

5.7. D. E. Smith and C. B. Harris, *J. Chem. Phys.* **87**, 2709(1987).

5.8. A. L. Harris, J. K. Brown, and C. B. Harris, *Ann. Rev. Phys. Chem.*, **39**, 341(1988).

5.9. M. E. Paige and C. B. Harris, *Chem. Phys.* **149**, 37(1990).

5.10. D. J. Nesbitt and J. T. Hynes, *J. Chem. Phys.* **77**, 2130(1982).

5.11. P. Bado, P. H. Berens, and K. R. Wilson, *Proc. Soc. Photo-Opt. Instrum. Eng.* **322**, 230(1982).

5.12. N. P. Ernsting, in *Ultrafast Phenomena VIII*, edited by J. L. Martin, A. Migus, G. A. Mourou, and A. H. Zewail (Springer-Verlag, Berlin, 1992). p.638.

5.13. A. G. Joly and K. A. Nelson, *Chem. Phys.* **152**, 69(1991).

5.14. R. Zadoyan, Z. Li, P. Ashjian, C. C. Martens, and V. A. Apkarian, *Chem. Phys. Lett.*, **218**, 504(1994).

5.15. R. Zadoyan, Z. Li, C. C. Martens, and V. A. Apkarian, *J. Chem. Phys.* **101**, 6648(1994).

5.16. G. J. Hoffman, E. Sekreta, and V. A. Apkarian, *Chem. Phys. Lett.*, **191**, 401(1992).

5.17. H. Kunz, J. G. McCaffrey, R. Schriever, and N. Schwentner, *J. Chem. Phys.* **94**, 1039(1991).

5.18. J. G. McCaffrey, H. Kunz, R. Schriever, and N. Schwentner, *J. Chem. Phys.* **96**, 155(1992).

5.19. J. M. Papanikolas, V. Vorsa, M. E. Nadal, P. J. Campagnola,J. R. Gord, and W. C. Lineberger, *J. Chem. Phys.* **97**, 7002 (1992); *ibid*, **99**, 8733(1993).

5.20. Q. Liu, J.-K. Wang, and A. H. Zewail, *Nature*, **364**, 427(1993).

5.21. M. Dantus, M. J. Rosker, and A. H. Zewail, *J. Chem. Phys.* **87**, 2395(1987); *ibid*, **89**, 6128(1988).

5.22. R. M. Bowman, M. Dantus, and A. H. Zewail, *Chem. Phys. Lett.* **156,** 131(1989).

5.23. J. L. Herek, S. Pedersen, L. Banares, and A. H. Zewail, *J. Chem. Phys.* **97**, 9046(1992).

5.24. T. Baumert, J. L. Herek, and A. H. Zewail, *J. Chem. Phys.* **99**, 4430(1993).

5.25. J. K. Brown, C. B. Harris, and J. C. Tully, *J. Chem. Phys.* **89**, 6687(1988).

5.26. B. J. Schwarz, J. C. King, J. Z. Zhang, and C. B. Harris, *Chem. Phys. Lett.* **203**, 503(1993).

5.27.N. F. Scherer, L. D. Ziegler, and G. R. Fleming, *J. Chem. Phys.* **96**,5544(1992).

5.28. N. F. Scherer, D. M. Jonas, and G. R. Fleming, *J. Chem. Phys.* **99**, 153(1993).

5.29. A. H. Zewail, M. Dantus, R. M. Bowman, and A. Mokhtari, *J. Photochem. Photobiol. A: Chem.* **62**, 301(1992).

5.30. Ch. Lienau, J. C. Williamson, and A. H. Zewail, *Chem. Phys. Lett.*, **213**, 289(1993).

5.31. S. Adelman, *J. Stat. Phys.* **42**, 37(1986).

5.32. S. Adelman, *Rev. Chem. Intermed.* **8**, 321(1987).

5.33. S. A. Adelman, *Adv. Chem. Phys.* **53**, 61(1983).

5.34. B. Dellinger and M. Karsha, *Chem. Phys. Lett.* **36**, 410(1975).

5.35. B. Dellinger and M. Karsha, *Chem. Phys. Lett.* **38**, 9(1976).

5.36. T. Tokizaki, T Makinura, H. Akiyama, A. Nakumara, K. Tanimura, and N. Itoh, *Phys. Rev. Lett.* **67**, 2701(1991).

5.37. M. H. Vos, J.-C. Lambry, S. J. Robles, D. C. Youvan, J. Breton, J.-L. Martin, *Proc. Natl. Acan Sci USA.*, **88**, 8885 (1992).

5.38. M. W. Balk, C. L. Brooks, III, and S. Adelman, *J. Chem. Phys.* **79**, 804(1983).

5.39. M. Buchner, B. M. Ladanyi, and R. M. Stratt, *J. Chem. Phys.* **97**, 8522(1992).

5.40. Z. Chen and R. M. Stratt, *J. Chem. Phys.* **95**, 153(1991).

5.41. T.-M. Wu and R. F. Loring, *J. Chem. Phys.* **99**, 8936(1993).

5.42. M. Cho, G. R. Fleming, S. Saito, I. Ohmine, R. M. Stratt, *J. Chem. Phys.* **100**, 6672(1994).

5.43. R. M. Stratt and M. Cho, *J. Chem. Phys.* **100**, 6700(1994).

5.44. G. Seeley and T. Keyes, *J. Chem. Phys.* **91**, 5581(1989).

5.45. P. Moore and T. Keyes, *J. Chem. Phys.* **100**, 6709(1994).

5.46. R. Zwanzig, *Phys. Rev.* **156**, 190(1967).

5.47. F. H. Stillinger and T. A. Weber, *Science* **225**, 983(1984).

5.48. R. A. LaViolette and F. H. Stillinger, *J. Chem. Phys.* **83**, 4079(1985).

5.49. R. M. J. Cotterill and J. U. Madsen, *Phys. Rev.* **B33**, 262(1986).

5.50. R. M. Lynden-Bell and W. A. Steele, *J. Phys. Chem.* **88**, 6514(1984).

5.51. G. J. Moro, P. L. Nordio, M. Noro, and A. Polimeno, *J. Chem. Phys.* **101**, 693(1994).

5.52. D. L. Bunker and B. S. Jacobson, *J. Am. Chem. Soc.* **94**, 1843(1972).

5.53. A. H. Lipkus, F. P. Buff, and M. G. Sceats, *J. Chem. Phys.* **79**, 4830(1983).

5.54. D. P. Ali and W. H. Miller, *J. Chem. Phys.* **78**, 6640(1983).

5.55. Y. Yan, R. M. Whitnell, K. R. Wilson, and A. H. Zewail, *Chem. Phys. Lett.* **193**, 402(1992); R. M. Whitnell, K. R. Wilson, Y. Yan, and A. H. Zewail, submitted to *J. Mol. Liq.*

5.56. R. J. LeRoy, *J. Chem. Phys.* **52**, 2683 (1970).

5.57. W. C. Swope, H. C. Anderson, P. H. Berens, and K. R. Wilson, *J. Chem. Phys.* **76**,637(1982).

5.58. D. M. Jonas, S. E. Bradforth, S. A. Passino, and G. R. Fleming, in the Proceedings of the Royal Netherlands Academy Colloquium on *Femtosecond Reaction Dynamics*, edited by D. A. Wiersma, North Holland, Amsterdam, 1994. p.133.

5.59. W. Wang, L. Dhar, J. Fourkas, K. A. Nelson, L. Xiao, and D. F. Coker, in the Proceedings of the Royal Netherlands Academy Colloquium on *Femtosecond Reaction Dynamics*, edited by D. A. Wiersma, North Holland, Amsterdam, 1994. p.111.

5.60. W. Wang, K. A. Nelson, L. Xiao, and D. F. Coker, *J. Chem. Phys.* (in press).

5.61. A. Rahman, M. J. Mandell, and J. P. McTague, *J. Chem. Phys.* **64**, 1564 (1976).

5.62. F. F. Abraham, *J. Chem. Phys.* **72**, 359, (1980).

5.63. J. R. Fox and H. C. Andersen, *J. Phys. Chem.* **88**, 4019(1984).

5.64. H. R. Wendt and F. F. Abraham, *Phys. Rev. Lett.* **41**, 1244(1978).

5.65. R. Alimi, A. Brokman, and R. B. Gerber, *J. Chem. Phys.* **91**, 1611(1989).

5.66. R. Alimi, R. B. Gerber, and V. A. Apkarian, *J. Chem. Phys.* **92**, 3551(1990).

5.67. R. Alimi, V. A. Apkarian, and R. B. Gerber, *J. Chem. Phys.* **98**, 331(1993).

5.68. R. Alimi, R. B. Gerber, J. G. McCaffrey, H. Kunz, and N. Schwentner, *Phys. Rev. Lett.* **69**, 856(1992).

5.69. A. Mokhtari, P. Cong, L. Herek, and A. H. Zewail, *Nature*, **348**, 225 (1990).

5.70. T. J. Dunn, J. N. Sweetser, I. A. Walmsley, C. Radzewicz, Phys. Rev. Lett. **70**, 3388(1993).

5.71.M. H. Vos, F. Rappaport, J.-C. Lambry, J. Breton, and J.-L Martin, *Nature*, **363**, 320(1993).

5.72. R. Lingle, Jr., X. Xu, S.-C. Yu, Y. J. Chang, and J. B. Hopkins, *J. Chem. Phys.* **92**, 4628(1990).

5.73. V. A. Apkarian, private communication.

5.74. R. Kubo, *Report Prog. Phys.* **29**, 255(1966).